POLITECNICO DI TORINO

Master degree course in Nanotechnologies for ICTs

Master Thesis

Giant Magnetocaloric Materials

Investigations of defects induced by ion collisions

Supervisor
Prof. Pietro Mandracci

Candidate
Erika FONTANA
matricola: s243966

Internship Tutor
INSP: Institut des NanoSciences de Paris
Prof. Martino Trassinelli

ANNO ACCADEMICO 2017 − 2018

Summary

The magnetic refrigeration is among the most promising environment-friendly refrigeration technologies, alternative to common techniques. This new technology exploits the magnetocaloric effect, i.e. the temperature variation occurring in materials when they are subjected to a magnetic field, to produce refrigeration without requiring the compression and expansion of a gas.

Even if the magnetocaloric effect is a property common to any magnetic medium, the choice of good material for magnetic refrigeration requires several properties such as a maximum of the magnetocaloric effect (normally associated to a magnetic phase transition) near the working temperature, wide operative range, no toxicity, etc. Some materials with a first order phase transition, called giant magnetocaloric materials and are the best candidates for the fabrication of next-generation magnetic refrigerators. Even if they are characterized by large entropy change that guarantees a larger refrigeration power, the use of giant magnetocaloric material is still limited because first order phase transitions are often associated with thermal hysteresis, which introduces losses of efficiency of the refrigeration cycle.

The aim of this project is to study the defects induced by ion collisions in giant magnetocaloric materials, since the recent research activity of the ASUR team (French acronym for "Clusters and Surfaces under Intense Excitation") at Paris Institute of Nanosciences (INSP) demonstrated that is possible to reduce, or even suppress, the thermal hysteresis, inducing defects by means of ion collisions.

The document is organized in 5 chapters.

Chapter 1 is an overview on theoretical aspects and the scientific context in which the research activity is set. First of all the definition of magnetocaloric effect will be introduced. A rigorous explanation of the effect will consider both thermodynamic approach and the order of the phase transition. Briefly, it will be explained how easy refrigeration cycles can be achieved through alternation of magnetization and demagnetization. The clarification these concepts will allow the reader to understand the physical mechanisms involved in magnetic refrigeration and which are nowadays the limits of this new technique. A summary on the ion-matter interaction concludes this chapter.

Chapter 2 is a summary of instrumentations used to irradiate and measurement of the modification induced in the sample. It collects the procedures used to simulate the working conditions and methods developed to correct imprecise measurements. Particularly relevant is the section 2.5, in which is described my personal contribute in the development of

a method for the correction of a biased read temperature in SQUID-magnetometer. The corrections, applied to analyse the samples, allow an accurate characterization of irradiated materials and deeper understanding of the processes involved in the thermal hysteresis suppression.

Since my experience can be divided into two parts, referring to two different types of samples used MnAs-thin films and MnFePSi-powders, the central core of the thesis is divided between chapter 3 and chapter 4.

Chapter 3 is dedicated to a well-known magnetocaloric material, MnAs. The magnetic properties of this medium were already characterized in a previous PhD thesis (Ref. [1]). As new contributes, I accurately studied the temperature dependency of the magnetization MnAs samples irradiated by ions with different ion masses and velocities and the evolution of the thermal hysteresis area of magnetization curves as a function of the ion fluence and the induced nuclear collisions in the sample.
As study on the nature of the induced defects, to test the robustness of the irradiation-induced effects, I analysed the modifications of irradiated MnAs film properties subjected to thermal annealing.

Chapter 4 is reserved to MnFePSi powders. The compound is a new magnetocaloric medium extensively studied for industrial magnetic refrigeration applications. The procedure for the irradiation-induced modifications and study of the magnetic properties of the material is presented in this chapter.

Chapter 5 resumes the conclusions and the expectations for future research.

Acknowledgements

First of all, I would like to offer my special thanks to the Politecnico di Torino for making my abroad experience possible and to ASUR team of the Paris Institute of Nanosciences (INSP) for welcoming me. My deepest appreciation goes to Martino Trassinelli, internship tutor at INSP, for his motivation and enthusiasm. His guidance helped me in all the time of research and writing of this thesis. I would like to express my gratitude to my supervisor of the Politecnico, professor Pietro Mandracci. I thank for his generous support and the helpful feedback offered.

I am grateful to have found a perfect colleague in Noemi Bosio, as results of our collaboration these years of study have gone so fast and in the best way. I would like to express the deepest appreciation to my friends that supported me during this journey. I would particularly like to thank Cristina Scarano, Francesca Di Pede e Paula Kroni because even if many years have passed, they are always present. A special thank is reserved to my boyfriend, dispenser of warm encouragements.

Finally, I want to express my gratitude to my parents extraordinary supportive and my sister that give me always the best moral and emotional support. Without their guidance and persistent help, this thesis would not have been possible, I am forever grateful.

Contents

Chapter 1

General introduction

After a brief historical introduction on the magnetic refrigeration, the reader will be informed about the main theoretical aspects of the research activity: the magnetocaloric effect and the ion-matter interaction. The magnetocaloric effect (MCE) will be first discussed in general form and then in a more rigorous way through a thermodynamic approach. The brief description of the phase transition will be useful to define the giant magnetocaloric materials, which are the main interest in the presented project. Concludes this chapter an introduction on ion matter interaction.

1.1 Historical introduction

The magnetocaloric effect, i.e the temperature change in magnetic materials caused by the exposition to a varying magnetic field, was discovered in 1917 by P. Weiss and A. Piccard [2]. They performed caloric measurement of Nickel at the phase transition (354°C) by applying and removing a magnetic field (1.5T).
From thermodynamical considerations on the magnetocaloric effect, Debye [3](1926) et Giaque [4] (1927) theorized the use of this effect to build a refrigeration cycle. In 1933 the first refrigeration system was realised by W. F. Giauque and his colleague D. P. Mac-Dougall [5]. It allowed, by means of adiabatic demagnetization of $Gd_2(SO_4)_3 \cdot 8H_20$, to obtain the record temperature of 0.25 K starting from about 1.5K. It was the first time that a sub-kelvin temperature was measured and the discovery was awarded the Nobel prize in 1949. Starting from this important event scientists and engineers begun to focus their attention on magnetic refrigeration (MR). To appreciate applications of the MR at room temperature we have to wait more than forty years. In 1976, Brown proposed the magnetic heat pumping near room temperature constituted of the ferromagnetic metal gadolinium, material characterized by magnetic phase transition at room temperature [6]. Two years after, the first prototype was developed [7]. In 1997, magnetic refrigeration at room temperature was boosted by Pecharsky's and K. A. Gschneidner's [8] discovery of materials that, thanks to a first order phase transition, were characterized by an extremely large magnetic entropy change at room temperature, the giant magnetocaloric materials. The interest for the MR is growing more and more, because it is a more efficient and ecological solution than standard technology, based on expansion and compression of gases.

1.2   Magnetocaloric Effect (MCE)

The magnetocaloric thermal effect is the response of magnetic material to a slowly varying magnetic field (not associated to induced current). It can be quantified as temperature change, ΔT, in adiabatic process or entropy variation, ΔS, in isothermal condition. The relation is illustrated in the Figure 1.1.
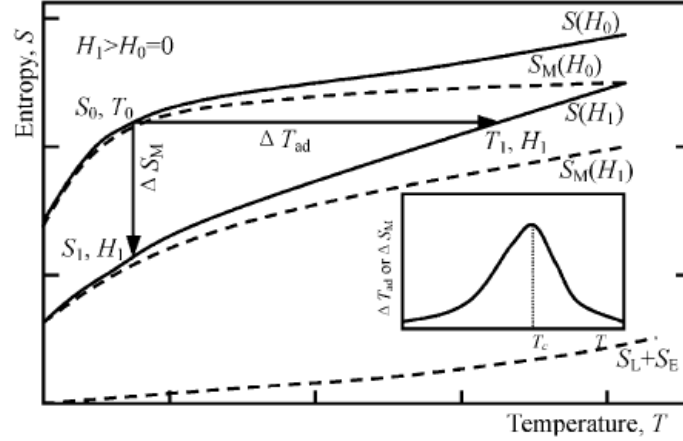

Figure 1.1: Schematic on the thermal dependency of the entropy in ferromagnetic material at different magnetic field. When the magnetic field varies from $H_0 = 0$ to $H_1 > H_0$, the horizontal line measures the temperature change ΔT_{ad} at adiabatic condition and the vertical line measures the entropy change, ΔS_m, at isothermal condition. The solid lines represent the total entropy of the system, while dotted lines show development of the other contributions of the entropy (magnetic, lattice and electronic entropy). The inner scheme displays the variation of the magnetic entropy or adiabatic temperature as function of the temperature. The curve is peaked at the critical temperature, characteristic of the material considered. Figure from Ref [9].

The entropy of a magnet at constant pressure, S, is a function of the temperature, T and the magnetic field, H.

$$S_T = S_m(T,H) + S_l(T) + S_e(T) \tag{1.1}$$

As shown by the equation 1.1, the total entropy is given by three factors: S_m is the magnetic entropy connected to the magnetization of the material, S_l is the lattice entropy, caused by the crystal-lattice vibrations and S_e is the electronic entropy of the free electrons in the sample.
For simplicity we can assume that each of the contributions is temperature dependent and just the magnetic entropy is strongly dependent on magnetic field. This is not completely true, when the magnetic and crystalline lattice are strongly coupled, lattice and electronic entropy become function both of the temperature and the magnetic field [10].

In absence of magnetic field the magnetic material is characterized by a random arrangement of the atomic spin system and a certain lattice vibration. When a magnetic field is applied the magnetic spins reoriented them self parallel to that field, and the magnetic entropy is lowered due to the disordered-ordered phase transition.

If the magnetic field is applied in adiabatic condition the material does not exchange anymore heat with the environment and the total entropy is kept constant. This means that the decrement of the magnetic entropy is balanced by an increment of the other contributions increasing the temperature of a factor ΔT_{ad} (horizontal line in the Figure 1.1). When the magnetic field is removed the situation is reversed and the solid is cooling, since the magnetic entropy is increased but the system has to preserve the total entropy unchanged.

In case that the magnetic field is applied in isothermal process, the entropy of the magnetic material can change while the temperature is kept constant. The spins reorientation according to the field causes a decrease of the magnetic entropy while the other two entropy contributions, depending just on temperature, are unchanged. The magnetic entropy change ΔS_m is equal to the total entropy variation ΔS (vertical line in Figure 1.1).

The temperature variation, ΔT_{ad}, in adiabatic process and the entropy change, ΔS_m in isothermal conditions are the two parameters used for the characterization of magnetocaloric materials. The MCE can be measured directly through caloric measurement of ΔT_{ad}. In this case the sample can be put into contact with thermal sensors ([11, 12]) or not by using thermoacustic sensors ([13, 14]). Alternatively the MCE can be studied using a thermodynamic approach that will be generally explained in the next part.

1.2.1 Thermodynamic approach of the magnetocaloric effect

In the previous part we discussed in general how the magnetocaloric effect can be observed, for the description of the thermodynamic approach I mainly followed the Ref.[15, 16].

The internal energy, $\mathcal{U}$, of a thermodynamic system, constituted by a ferromagnetic sample subjected to magnetic field, is function of the volume $\mathcal{V}$, the magnetic field H and the entropy $\mathcal{S}$.

$$\mathcal{U} = \mathcal{U}(\mathcal{S}, \mathcal{V}, H) \tag{1.2}$$

The total differential of U is

$$d\mathcal{U} = Td\mathcal{S} - pd\mathcal{V} - \mu_0 Hd\mathcal{M} \tag{1.3}$$

where μ_0 is the magnetic permeability and $\mathcal{M}$ is the magnetic momentum. In order to evaluate the magnetocaloric effect we have to consider the Gibbs free energy $\mathcal{G}$.

$$\mathcal{G} = U - T\mathcal{S} + p\mathcal{V} - \mu_0 H\mathcal{M} \tag{1.4}$$

The total differential can be obtained easily as follows:

$$d\mathcal{G} = d\mathcal{U} - pd\mathcal{V} + \mu_0 Hd\mathcal{M} - Td\mathcal{S} - \mathcal{S}dT + pd\mathcal{V} + \mathcal{V}dp - \mu_0\mathcal{M}dH - \mu_0 Hd\mathcal{M} \tag{1.5}$$

By substituting 1.3 in 1.5 and considering isobaric condition, the final equation becomes:

$$dG = -SdT - \mathcal{M}dH \tag{1.6}$$

For the Gibbs free energy G the internal parameter $\mathcal{S}$ and $\mathcal{M}$ conjugated to external variables T and H, can be determined by the following equation state:

$$\mathcal{S}(T, H) = -\left(\frac{\partial \mathcal{G}}{\partial T}\right)_H \tag{1.7}$$

$$\mathcal{M}(T, H) = -\frac{1}{\mu_0}\left(\frac{\partial \mathcal{G}}{\partial H}\right)_T \tag{1.8}$$

Using 1.7 and 1.8, from the equalities of second derivative, $\frac{\partial}{\partial H}\left(\frac{\partial \mathcal{G}}{\partial T}\right) = \mu_0 \frac{\partial}{\partial T}\left(\frac{\partial \mathcal{G}}{\partial H}\right)$, we can calculate:

$$\left(\frac{\partial \mathcal{S}}{\partial H}\right)_T = \mu_0\left(\frac{\partial \mathcal{M}}{\partial T}\right)_H \tag{1.9}$$

By introducing the volumetric mass ,ρ, we generalize the equation 1.9 replacing the extensive variable ($\mathcal{S}$) with intensive quantities (S). In such way the formulation 1.10 does not depend on the system size or the amount of material in the system.

$$\left(\frac{\partial S}{\partial H}\right)_T = \frac{\mu_0}{\rho}\left(\frac{\partial M}{\partial T}\right)_H \tag{1.10}$$

The heat capacity C at constant parameter x is defined as:

$$C_x = \left(\frac{\delta Q}{dT}\right)_x \tag{1.11}$$

where Q is the heat quantity changing the system temperature on dT.
Using the second thermodynamic law $dS = \delta Q \backslash T$, 1.11 can be rewritten as :

$$C_x = T\left(\frac{\partial S}{\partial T}\right)_x \tag{1.12}$$

The entropy change of the system can be expressed as:

$$dS = \left(\frac{\partial S}{\partial T}\right)_H dT + \left(\frac{\partial S}{\partial H}\right)_T dH \tag{1.13}$$

When the material is subjected to a constant magnetic field the specific heat can be calculated as $C_H = T(\partial S \backslash \partial T)_H$. Replacing the heat capacity at constant field and the equation 1.9 in 1.13 the entropy change results to be:

$$dS = \frac{C_H}{T}dT + \frac{\mu_0}{\rho}\left(\frac{\partial M}{\partial T}\right)dH \tag{1.14}$$

This formulation is useful to quantify the magnetocaloric effect in adiabatic and isothermal process.

Adiabatic process

When the sample material is subjected to adiabatic process, for definition, the entropy change is null ($dS = 0$). Satisfying this condition in 1.14 is possible to calculate the reversible temperature change, ΔT_{ad}, which quantify the MCE.

$$\Delta T_{ad} = -\frac{\mu_0}{\rho} \int_{H_0}^{H_1} \frac{T}{C_H} \frac{\partial M}{\partial T}_H dH \tag{1.15}$$

Isothermal process

When the magnetocaloric material is subjected to isothermal procedure, the total entropy change, ΔS, is equal to the magnetic entropy variation, ΔS_m. In this case the magnetocaloric effect is quantified by determining the specific entropy change from the equation 1.14, considering $dT = 0$

$$\Delta S = \Delta S_m = \frac{\mu_0}{\rho} \int_{H_0}^{H_1} \left(\frac{\partial M}{\partial T}\right)_H dH \tag{1.16}$$

1.2.2 The phase transition

The stability of different phases depends on the evolution of the Gibbs free energy. The Gibbs free energy is defined as the thermodinamic potential that can be used to calculate the maximum reversible work performed by a thermodynamic system at constant temperature and pressure. Minimising the Gibbs free energy means for the system maximise the total entropy, when G assumes minima value the system reach the equilibrium.

The Landau theory allows to study the phase transition by means of Gibbs free energy. It is based on the idea that the free energy can be expanded in Taylor series, $\mathcal{G}$, in such way for a ferromagnetic-paramagnetic transition, in absence of external magnetic field and in proximity of the critical temperature T_c the Landau free energy given by:

$$\mathcal{G}(P, H, T) = \mathcal{G}_0 + a(T - T_c)\mathcal{M}^2 + b\mathcal{M}^4 + c\mathcal{M}^6 + ... \tag{1.17}$$

where $\mathcal{M}$ is the magnetic momentum, considered for simplicity independent on external parameter (pressure...), $\mathcal{G}_0$ is the free energy independent on $\mathcal{M}$ and a, b, c are the expansion coefficients called Landau coefficients. a and c are always positive while b is negative for second order phase transition and positive for first order phase transition [17, 18].

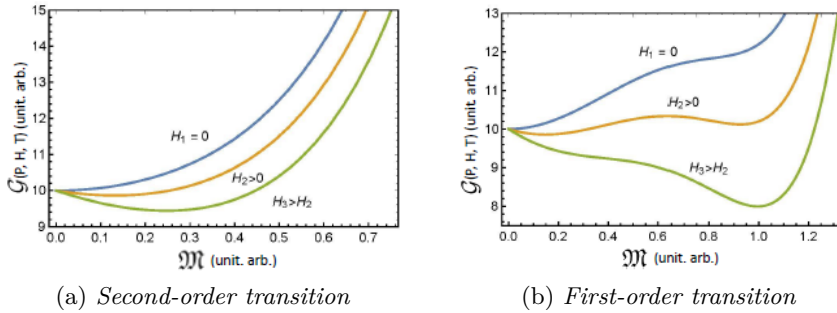(a) *Second-order transition*   (b) *First-order transition*

Figure 1.2: Free energy versus the magnetic momentum at different magnetic fields [1].
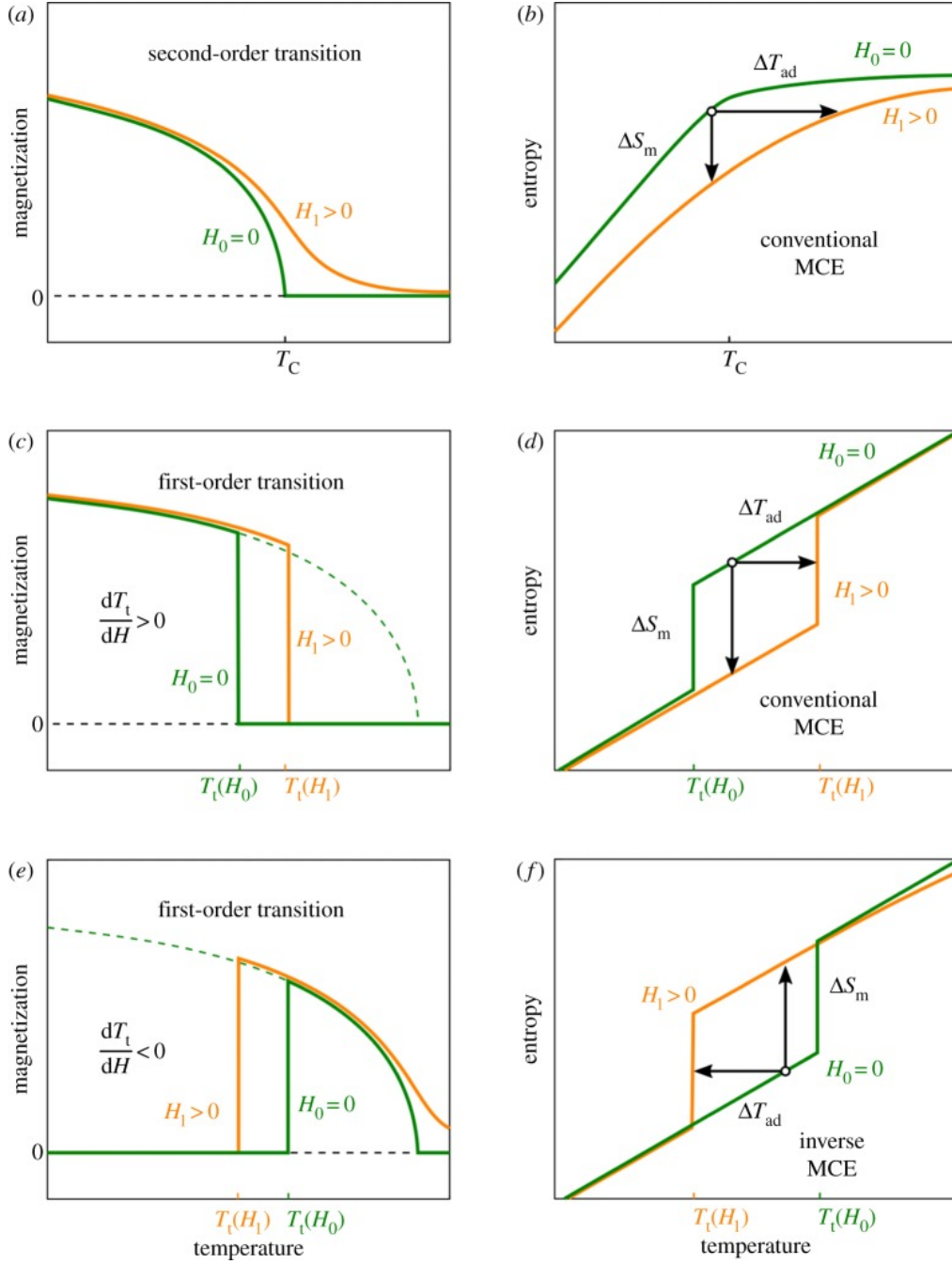
Figure 1.3: Schematic of the difference between the first (c)-(f) and second order phase transitions(a), (b). (a), (c) and (e) display the magnetization as function of the temperature. (b), (d) and (f) show the entropy as function of the temperature. In green the measures are performed with null magnetic field while in yellow are displayed the results considering the magnetic field. The first order transition is displayed both in conventional MCE (c), (d) and inverse MCE (e) and (f). Figure from Ref. [19].

Second order phase transition

Second order phase transition is defined by a Gibbs free energy function having continuous first derivative and a discontinuous second derivative. In this case the free energy function G is minimized by a single value of M, 1.2(a). This means that the transition goes continuously from one phase to the other without the coexistence of two phases in equilibrium. The magnetic momentum and the total entropy are computed by the equations 1.7 and 1.8, being the first derivative continuous, $\mathcal{S}$ and $\mathcal{M}$ will result to be continuous as well [20].

In Figure 1.3(a) the magnetization is displayed as function of the temperature. In absence of field, green curve, the material pass from ferromagnetic to paramagnetic state at the critical temperature, called Curie temperature. When the magnetic field is applied, yellow curve, a partial orientation of the spin, causes the preservation of a certain magnetization.
In Figure 1.3(b) the total entropy is shown, as we discuss in the previous part, the system passes from a disordered state to more ordered one by the application of the magnetic field and the entropy value is lowered [19]. The decrease of the total entropy is observable in isothermal condition, horizontal arrow ΔS_m. In case of adiabatic condition instead just the magnetic entropy contribution is lowered and the temperature is increased, vertical arrow ΔT_{ad}.

First order phase transition

The first order phase transition is characterized by a discontinuity in the first derivative of Gibbs free energy function. Remembering the equations 1.7 and 1.8, even the magnetization and the total entropy are discontinuous.
In first order phase transition, for a defined range of temperature and magnetic field, the minimization of the free energy can be obtained for two different values of $\mathcal{M}$, Figure 1.2(b). If in the second order phase transition the passage from ferromagnetic to paramagnetic state occurred continuously, in this transition we can observe a metastable condition in which both the two phases coexist [20].

The representation of the magnetization as function of the temperature, Figure 1.3(c), shows that the ferromagnetic state ($M > 0$) is stable for low temperature and abruptly changes in paramagnetic at defined transition temperature T_t. By the application of the magnetic field, $H_1 > 0$, the material is stabilized at higher magnetization causing a shift of the transition temperature.

In case of standart MCE the difference of the transition temperature shift $\frac{dT_t}{dH}$ is positive, while it is negative in case of the inverse MCE (Figure 1.3(e)). For a inverse MCE the magnetization of the material by means of magnetic field causes a decrease of the temperature in adiabatic condition and an increase of the entropy in the isothermal process (Figure 1.3 (f)) [19]. In Figure 1.3 (e) the ideal behaviour of the entropy is plotted as function of the temperature. The horizontal line between two isomagnetic curve corresponds to adiabatic temperature change ΔT_{ad}, while the vertical one represents the magnetic entropy variation ΔS_m .

The materials characterized by a first order phase transition, are called giant magnetocaloric (GMC) material because of the strong magnetocaloric response caused by the large entropy change [21]. The discovery of the giant MCE resulted to be an important breakthrough in the magnetic refrigeration. On the other hand, the first order phase transition is characterized by some problems related to the thermal hysteresis. Thermal hysteresis causes a strongly dependency on the material history, with consequent difficulty in the control of thermodynamic cycles and efficiency losses, and involves generation of latent heat and volumetric/structural changes [22].

Phase diagram

In giant magnetocaloric materials, the magnetic transition is often associated to modification of the lattice. In this case, to consider the contribution of the lattice-magnetic momentum coupling, a more general formulation of the Gibbs free energy is required:

$$G(P, H, T) = G_{lat,el}(P, H, T) + G_m(P, H, T) + G_{lat-spin,el-spin}(P, H, T) \tag{1.18}$$

where $G_{lat-spin,el-spin}(P, H, T)$ is the term describing the coupling.
The modifications occurring in the material depend on several parameters, the most important, working in isobar condition, are the temperature and the magnetic field.
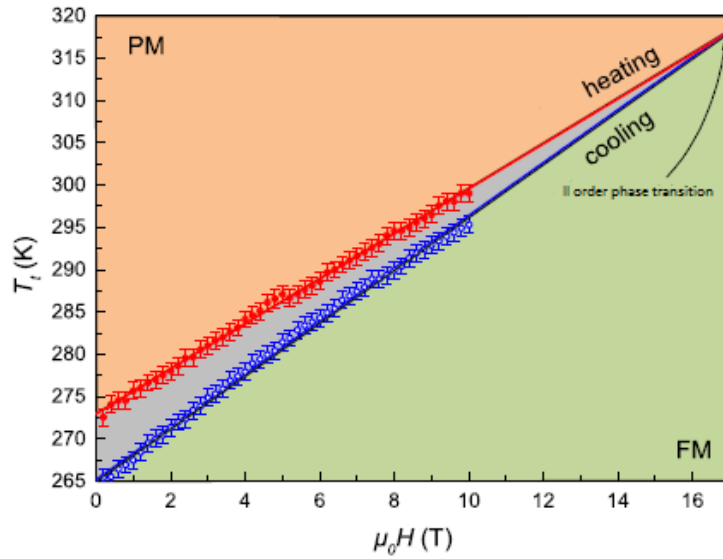

Figure 1.4: Inflection points of the heating and cooling transition temperature versus applied field up to 10T, by linear interpolation, the cooling and heating curves of the phase diagram of MnFePSi are obtained [23]. The portion of graph in red represents the conditions for which the material is in paramagnetic phase (PM), in green the conditions for reaching the ferromagnetic configuration (FM). In blue is defined the metastable case in which the two phases coexist. At the intersection points of the two straight lines the transition becomes of second order.

16

The phase transition of materials can be mapped through the phase diagram. It represents the combinations of the variables for which a specific phase exists. The phase diagram contains the information that helps to understand what phases are present in the material and which transformations can be expected when we change one parameter [24, 25, 26]. For a simple explanation of the structure of a phase diagram, in the following part we will consider the phase diagram obtained with MnFePSi taken from Ref [23]. The same magnetocaloric material will be analysed in the Chapter 4, there, a phase diagram will be extrapolated from our research activity.

In Figure 1.4 the phase diagram of MnFePSi was properly built representing the transition temperature versus the applied field for both the heating and cooling curves. Above the heating branch (in red) the material is in a paramagnetic phase while below the cooling curve (in green) it behaves as ferromagnetic. The area in blue represents the mixed state, there the compounds results in a metastable condition and both the two phases can be present. Investigations on magnetocaloric Fe_2P compound showed the presence of second order transition at relatively small magnetic field [27]. The amount of Mn and Si doping, in the sample we are going to analyse, are used to prevent the second order transition at the magnetic field between 0 and 10T. In Figure 1.4 the second order phase transition is defined by the intersection of the two straight lines(heating and cooling curves) representing the critical temperature (for a fixed field) and field (for a fixed temperature) when the phase transition occurs. In that point the hysteresis is no more observed and the type of material transition changes. Since the magnetic field conditions, for which the second order transition can be appreciated, will be too much elevated for our measurement purpose, the MnFePSi sample analysed in the following chapters 4 will be considered as a material characterized just by a first order phase transition .

1.3   Magnetic refrigeration

On the basis of the magnetocaloric effect is possible to create magnetic refrigerators. These refrigeration systems exploit the entropy change of magnetic materials, caused by variation of an external magnetic field, to absorb or release heat in cycles of magnetization and demagnetization.

The magnetic refrigeration (MR) is emerging technology that compared with the conventional refrigeration systems, based on compression and expansion of gases, is expected to have great applicable prospects. The interest in MR is related to their energy and cost saving potential, high efficiency and reliability. The efficiency of the new technique can be 30-60% of the Carnot cycle while the vapour compression refrigeration is only 5-10% [28]. In addiction the no need of compressor reduces the vibration and the moveable parts, resulting in longer system-lifetime [16, 9]. Finally a great advantage is its environmental-friendly aspect: not requiring gases, it does not have ozone-depleting and greenhouse effects.

The general working principle of a magnetic refrigerator consists in a cyclical repetition of a process. A magnetic material, whose entropy and temperature can be changed by means of an external magnetic field, absorbs heat from cold heat exchanger and transfer

it to a hot heat exchanger. Different types of cycles combine different isothermal and adiabatic magnetization to cool the load [29, 28].
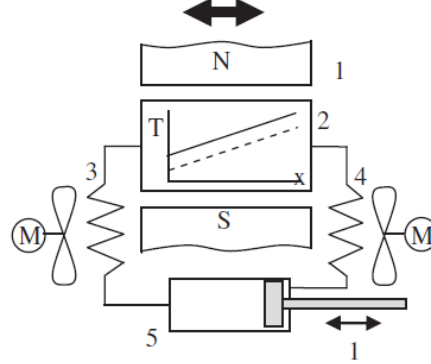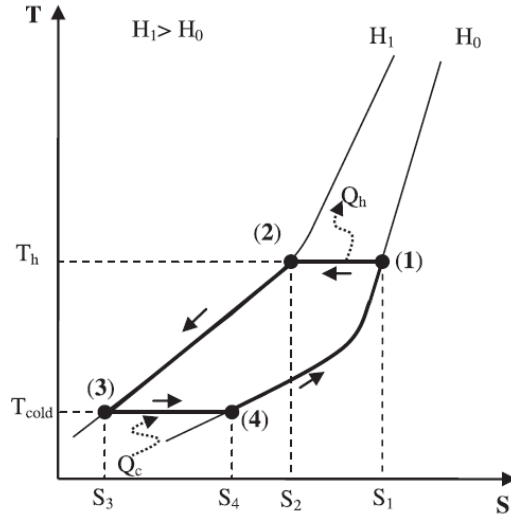

Figure 1.5: Schematic of magnetic refrigeration system. (1) magnet, (2) regenerator with magnetocaloric material, (3) cold source heat exchanger, (4) hot source heat exchanger (5) pump to allow the flow of the transfer fluid through the active generator [15].

The important development, that allows to obtain efficiently room temperature refrigeration, is the active magnetic regenerator (AMR), introduced in 1981 [30]. The AMR, added to a magnetic refrigeration system, uses a transfer fluid (that can be simply water) to absorb heat, expelled in one stage of the cycle, and release that in another stage [9]. Possible schematic of the MR system is displayed in Figure 1.5.
Among the possible refrigeration cycle, Ericsson and Brayton cycles, are the ones that allow room temperature cooling process with larger temperature span and easy operation. The working principles of these are explained in the Figure 1.6 and 1.7.

Figure 1.6: Schematic of the Ericsson refrigeration cycle.
1-2: Isothermal magnetization. The magnetic field is increased from H_0 to H_1 and the heat is transferred from refrigerant magnet to hot source.
2-3: Isofield cooling. Heat exchange from magnetic refrigerant and regenerator fluid.
3-4: Isothermal demagnetization. The magnetic field is lowered from H_1 to H_0 and heat is absorbed from cold source.
4-1: Isofield heating. The regenerator fluid absorbs heat. Figure from Ref. [15].
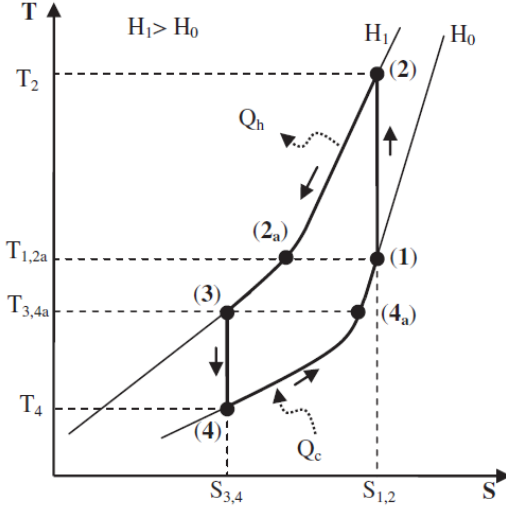
Figure 1.7: Schematic of Brayton refrigeration cycle.
1-2: Adiabatic magnetization. The temperature is increased from T_1 to T_2.
2-2a: Isofield cooling. The magnetic material transfer heat to hot source exchanger.
2a-3: Isofield cooling by means of regerator.
3-4: Adiabatic magnetization. The temperature is lowered to T_4.
4-4a: Isofield heating. The temperature increases absorbing heat from cold source exchanger.
4a-1: Isofield heating by means of the regenerator. Figure from Ref. [15].

The central core in the design of magnetic refrigeration system is the choice of the magnetic material [31, 32]. Numerous studies on magnetocaloric samples have been carried out to find good compromise among material's properties, refrigerator performance and parameters of the system design. The main aspects that researchers want to optimize are the values of ΔT_{ad} and ΔS_m in order to maximize the refrigerant power P_r.
The refrigerant power can be defined as the integral of the entropy variation over the temperature:

$$P_r = \int_{T_{cold}}^{T_{hot}} \Delta S(T) dT \tag{1.19}$$

where T_{cold} and T_{hot} are the temperature of the cold and hot source heat exchanger.
In Figure 1.8 crystalline materials are grouped into different families. The magnetic materials, have been selected with phase transition near room temperature, and each of them is categorized according to the entropy variation as function of the temperature, magnetic field constant at 5T [33].

In the research activity here reported, the attention will be reserved just to giant magnetocaloric material MnFePSi powders (V in Figure 1.8) and MnAs thin film (VI in Figure 1.8). The giant magnetocaloric material, being characterized by a first order phase transition, have a large entropy change in at the transition temperature. The application of GMC materials, nowadays, is still limited because the transition is often associated with a thermal hysteresis, which limits the refrigerant power and the efficiency of the system [34, 35, 36].
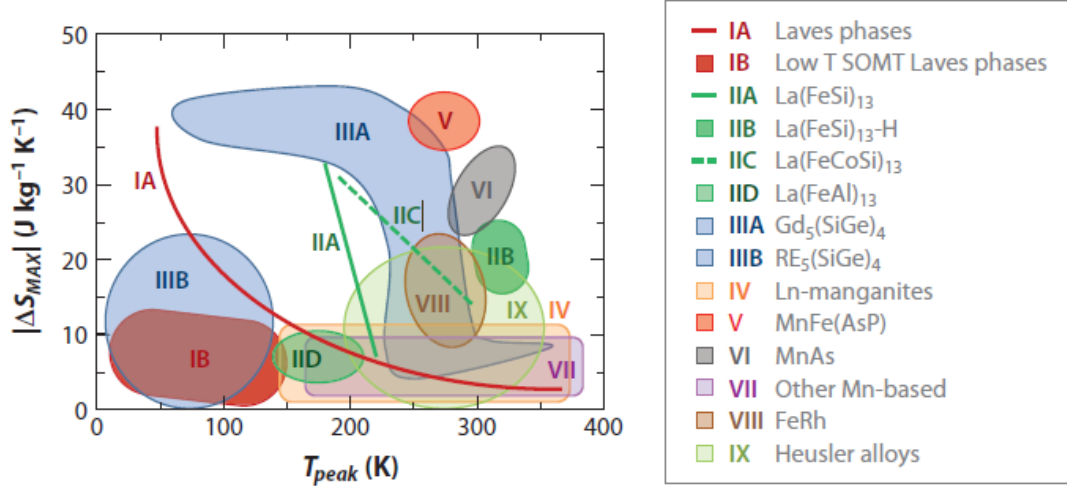
19

Figure 1.8: Maximum entropy change for ΔS_{max} for $\Delta H = 5T$ as function of the temperature for different magnetocaloric material having first order phase transition [33].

1.4 Modification induced in giant magnetocaloric material

Despite the fact that giant magnetocaloric materials exhibit large entropy change the practical application of giant magnetocaloric material is still limited. The materials for magnetic refrigeration have to fulfil several properties [15, 9] that can be resumed as:

- low Debye temperature values in order to avoid that the temperature makes the fraction of lattice entropy small in high temperature range.

- transition temperature near working temperature

- for a easy heat transfert is required low specific heat and large temperature conductivity

- no toxicity

- good mechanical properties

- low cost of the material and the manufacturing

- low environmental impact

In addiction the first order phase transition is often associated with thermal hysteresis that induces losses in thermal cycle reducing the cooling power of the refrigerator. With increasing interest scientists from the entire world are looking for a solution to reduce the latent heat. The most popular method is based on variation of the composition of the

material by doping the sample [37, 38]. This solution allows the suppression of small hysteresis but sometime causes the reduction of the magnetocaloric properties of the material. A different procedure consists in the application of strain on thin film or bulk material [39]. The technique proposed in the project is the irradiation of powders and thin films by accelerated ions. The reach activities, carried out at Institut des NanoSciences de Paris in years, demonstrated that ions bombardment can change the film properties [1, 40, 41, 42, 43, 44]. In particular it has been demonstrated that in some material induced defects allow to reduce or remove the thermal hysteresis without changing the magnetocaloric properties of the sample.

1.4.1   Basis process in ion-matter interaction

The irradiation of a target material, by means of accelerated ion beams, is one of the most powerful tools to modify the properties of a sample material. The technique requires a deep knowledge of the role of the defects in a crystalline structure. The nature of the ion-matter interaction depends on several factors connected both on the nature of the projectile and of the target sample [45, 46]. The process of interaction depends both on the potential energy (internal energy) and the kinetic energy of the projectile ions.

The potential energy of the impinging ions is given by the sum of all binding energies of the missing electrons and can reach values of several tens up to hundreds of keV. When the ion is penetrating into the material the potential energy is easily lost. The temperature of the sample increases because of the deexcitation of electrons captured by impinging ions. This process can cause amorphisation of the material. In case of very slow ions impinging conducting material portion of the potential energy can be converted into kinetic energy through the formation of hallow-atoms [47]. This effect will be neglected in the discussion, since the working conditions of the irradiation avoid this phenomenon.

The kinetic energy irradiation beam is obtained by the product of the acceleration tension and of the charge q. When energetic ion penetrates the solid it undergoes a series of collisions with atoms and electrons in the target and the energy is transferred. This process is described by the stopping power [48], the energy transferred per unit of path length of an ion on its trajectory, $\frac{dE}{dx}$. This can be expressed as:

$$S = \left(\frac{dE}{dX}\right)_{loss} = \left(\frac{dE}{dX}\right)_{el} + \left(\frac{dE}{dX}\right)_{n} \tag{1.20}$$

The total power loss is given by the sum of three terms. The first term describes the ion energy lost resulted from elastic atomic collision with the target atom, nuclear stopping energy, the second one is caused by the excitation and ionization of target electrons, electron stopping power.

The reciprocal integral of 1.20 defines the total projectile range. The projectile range defines the depth profile and the nature of the lattice disorder in the process. Since this phenomena is a non equilibrium random process, ions of a given type and given energy do

not have the same range of penetration.

The importance of the two contributes in the total energy loss depends on the energy and the atomic number of impinging ions [46].

- The nuclear stopping power is the average energy loss resulting from the interaction of ions with the nucleus of the medium. The interactions are generally elastic collisions that involve large energy loss and significant angular dispersion. This type of loss are predominant in irradiation with ions characterized by elevated atomic number (heavy ions) and accelerated at low kinetic energy, $E_k < 1 MeV$. The path of the impinging particle is limited by the low kinetic energy and as consequence the perturbations of the target material are concentrated in hundreds of nanometers below the surface, left in Figure 1.9. The collisions lead to atomic displacements and lattice vibrations in the target at the same time the energy transfer can be sufficient to induce a collision cascade.

- The electronic power stop is obtained consequent to inelastic interactions of ions and the electrons of the sample. This process is predominant with ions accelerated high energy range ($E_k > 1 MeV$) and with small atomic number. In this case, as displayed on the right of Figure 1.9 the impinging particle has a penetration depth considerably extended up to the order of mm. The energy transfer between the ions and the electrons surrounding the trajectory causes an increase of the internal temperature of the sample.
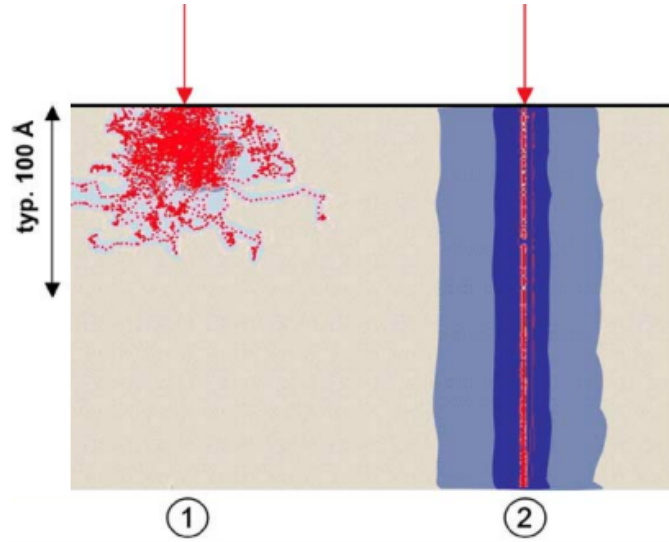

Figure 1.9: Scheme of the ion-matter interaction dominated by:(1) Nuclear collisions. Slow charged ions characterized by kinetic energy in the range between keV-MeV. (2) Electronic collisions. Fast charged ions characterized by kinetic energy in the range between MeV-GeV. Figure from Ref [45].

Both nuclear and electronic stopping power behaviour are displayed in the Figure 1.10. They both increase with increasing energy reach a maximum, that for nuclear stopping power is called Bragg peak, and then decreases. The accumulated electronic energy loss reaches its maximum at energy of magnitudes higher respect the nuclear case. This behaviour is due to the dependency of the interaction process on the ion velocity.
At ion velocities v significantly lower (low kinetic energy) than Bohr velocity of the atomic electrons v_0, the ion carries its electrons and tends to neutralize by electron capture, at these velocities, elastic collision dominate. As the ion velocity is increased (higher kinetic energy) the nuclear energy loss diminishes as $1/E_0$. The electronic energy loss (inelastic collision with atomic electrons) soon becomes main interaction [48].
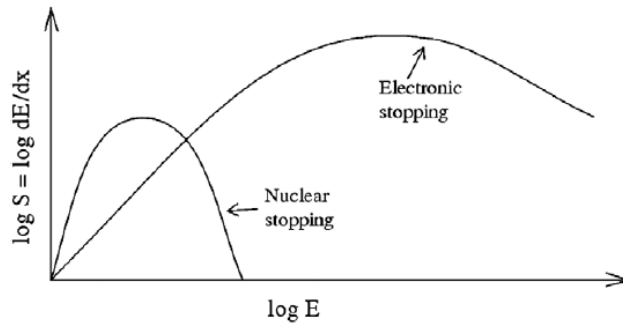

Figure 1.10: Projectile ion energy versus energy loss [48].

During the interaction between ions and solid surface many processes are involved (reflection of ions, emission of an electron, implantation of the ion, electromagnetic wave emission...) [49]. During binary collision, if the energy transferred to the recoil atoms is sufficiently large, this generates binary collisions between the target atoms with important distortion of the lattice. Depending on the energy of the recoil atoms a linear or spike regime can be established. In the first case the recoil atoms carry enough energy to produce further recoils but the density of recoil atoms is low and the knock-on collisions dominate. In the second case the density of recoil atoms is so high that within a certain volume (spike volume), the majority of atoms are in motion [50].
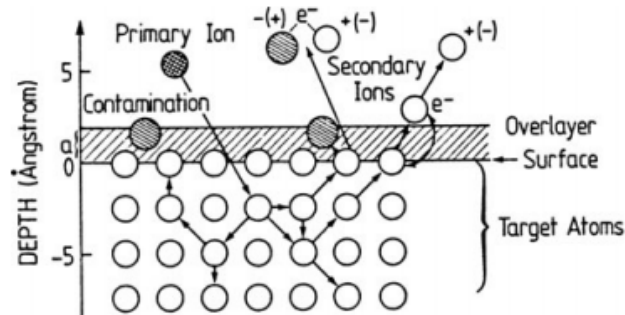

Figure 1.11: Summary of ions-solid interaction [50].

23

After the interaction between the solid material and the ion beam, stable or metastable point like defects are created. The defects can be organized in three categories [51]. If one ore more original atoms are missing in the original lattice site, a vacancy type of defect is created. In case original atom shifted from its native position or a foreign atom occupies the interstitial position of the crystal, an interstitial vacancy is formed. When foreign atom occupies the original atom, the defect is defined substitutional. The motion of the defects inside the crystal lattice can cause the extension of the defects in line-defects (edge or screw dislocation), surface-defects (grain or twin boundary) or volume-defects (void, crack, inclusion and precipitation) [52, 48].

1.4.2 Modification of magnetic properties

The studies on magnetic material modifications induced ion beams started in the 1998, when the magnetic properties of cobalt-platinum multilayer were changed by He+ irradiation [53]. This technique allowed to obtain regions with very different magnetic properties, extended at sub micron size, by means of the local coercivity change induced by irradiation. Many fundamental studies performed in the past concerned the characterization of second order transition material (see Ref[54, 55, 56, 57, 58, 59, 27]). In these case the research activity was focused on the control of the magnetic properties (the anisotropy, the magnetic saturation, the microstructural parameteters.) acting on induced disorder and variation of domain wall mobility caused by ion bombardment. The object of the study, presented in this thesis, is the evolution of recent studies on giant magnetocaloric material demonstrating that first order features can be changed by means of small ion fluencies.

(a)   (b)
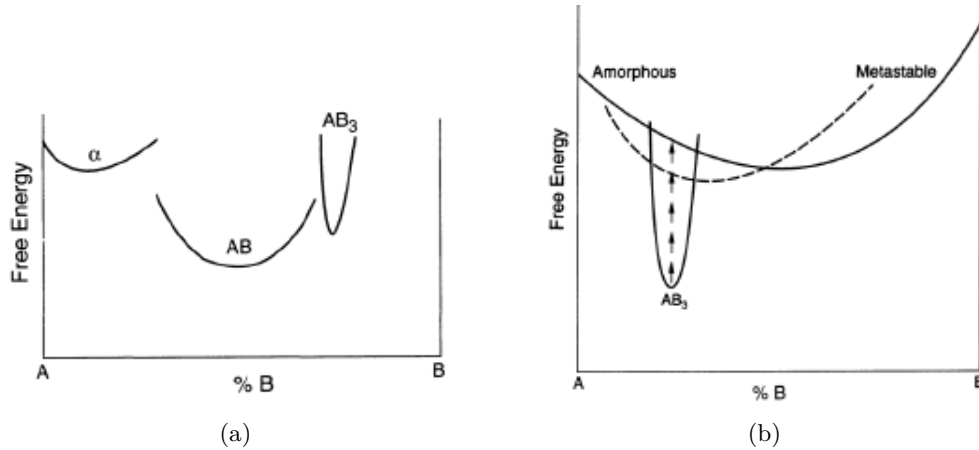
Figure 1.12: Schematic of the free energy as function of the concentration of *A* and *B* elements (a). Free energy as function of *A* and *B* elements in case of AB_3 alloy (b).

Depending on the kinetic energy of the impinging ion, the irradiation on solid material can locally increase the heat and generate metastable state or local annealing producing ordered structure in amorphous material. As we have previously seen, bombardment through ions generates defects. The magnetocaloric material responds to local modification

by changing the structural phase of the material. In fact the structure of a binary alloy depends on the percentage of A or B metal element forming the alloy. The stability of a phase is defined from the minimum of Gibbs free energy. By looking at Figure 1.12(a) , it is evident that the composition AB, having a wider minimum, is more stable than the AB_3 and it will be less affected by ion irradiation. In case of AB_3 alloy of the considered example, the irradiation can increase the free energy and induce the material to pass to a metastable or amorphous state 1.12(b).

Chapter 2

Instrumentation and methods

This chapter provides a brief description of the instrumentation and the experimental methods used. The first part is an introduction about SRIM (Stopping and Range of Ions in Matter), a free available computer program for simulating the interaction between the target and the ion beams. The second part concerns the description of two irradiation facilities available at INSP laboratories: an accelerator facility for fast ions beams production (SAFIR) and a multicharged ions source (SIMPA) for medium-slow ion beams. The third section is dedicated to the analysis of the magnetic properties. Two types of the magnetometers will be presented: the vibrating sample magnetometer (VSM) and the superconducting quantum interference device (SQUID). Particular attention will be reserved to measurements corrections required in case of measure of the magnetization by SQUID magnetometer.

2.1 Numerical simulation: the program SRIM

In the Chapter 1 we have seen that the nature of the interactions between ions and matter is intrinsic ballistic, as consequence the simulation of this phenomena required a Monte Carlo approach and high level of knowledge about quantum mechanical treatment of ion-atom collisions. Luckily comes to our aid the groups of programs collected in The Stopping and Range of Ions in Matter: SRIM. The results obtained from these simulations will be used to define the optimal working conditions for the irradiation of the sample.

SRIM is a collection of softwares useful to predict the behaviour during the transport of ions in the matter. In our specific case we will use a particular subgroups of programs TRIM (Transport of Ions in Matter).
The efficiency of the numerical computation consists in the use of statistical algorithms, which allows the ion to make jumps between calculated collisions and then averaging the collision results over the intervening gap [60].
The program in the setup calculation allows a proper description of the target electronic structure and interatomic bonds, taking into account:

- the screen coulomb collision of ion and atoms, including the exchange and the correlation interaction between the overlap of the shells

- the ion long range interactions, characterized by the creations of electron excitations and plasmons within the target

- the charge state of the ion using the concepts of effective charge

The scope of the SRIM simulations are mainly two: the determination of the experimental parameters of the future irradiation sections and the extraction of estimations of the collision characteristics as the number of collisions per ion for specific experimental conditions.

The simulation exploits as input experimental information about the target, the incident ions to extract parameters useful for a correct irradiation section. It is required to specify the elements which make up the target and build up the target-layer with defined thickness and density. For what concerning the beams, it is necessary to point out the type and the mass of the ions used, SRIM suggest as mass the one of the most abundant isotope. It is possible to work with different angle of incidence, or use the ions directed perpendicular to the surface. The time required for the calculation is defined by the type of simulation chosen, in our case we will work in modality "*Detailed Calculation with Full Damages Cascades*". This option takes into consideration every recoiling atom until the energy drops below the lowest displacement energy of any target atoms. It is the most efficient condition for the simulation, but on the other hand it requires more time respect the quick mode.
For a sample irradiated by a defined type of ions at certain incident angle, the kinetic energy of the particle defines the penetration depth into the material.

SRIM produces several outputs. In our case we are interested in the calculation of the amount of damages generated in the target and the relevant results can be:

- **Recoiling Energy**: the energy transferred from incident ions to target atoms and energy absorbed by target atoms [eV/angstrom/ion]

- **Ionization Energy**: the energy absorbed in electronic stopping by target atoms from incident ions and recoil atoms [eV/angstrom/ion]

- **Vacancies** Vacancies created[Vacancies/angstrom/ion]

- **Collisions** Table of all ion/target atom collisions which lead to target damage

These outputs are organized in table of values as function of the distance from the surface impinged by the ions. The profile is calculated by dividing the thickness of the target layer, specified by the user, into equal-width bins [61]. In the Chapter 3 the detailed simulations used for the analysis of MnFePSi-samples will be presented.

2.2   Irradiation technique

The characterization of the magnetic properties of the sample is made possible by the irradiation of the material with ions. Depending on the energetic profile at which we want to modify the samples, different types of accelerator of ions source can be required [62].
In our experience particles at high energy up to 2MeV will be provided by SAFIR, french acronym for "System of Analysis for Highly Accelerated Particles", while lower energy (order of keV) will be used at SIMPA, french acronym for "Highly Charged ion Source of Paris".

2.2.1   Systeme d'Analyse par Faisceux d'ions Rapides: SAFIR

SAFIR (French acronym for "Rapid Ion Beam Analysis System") is a device designed to probe the structural and compositional profile of surface region through the analysis of the interactions between fast particle beams and the atoms of a sample. It finds its application in the analysis of thin ($<1\mu m$) or ultra-thin ($<10nm$) layers. The acceleration of the ions is provided by a Van de Graaff accelerator. It is supplied by the company High Voltage Engineering Europa. A schematic of the structure is shown in Figure 2.1.
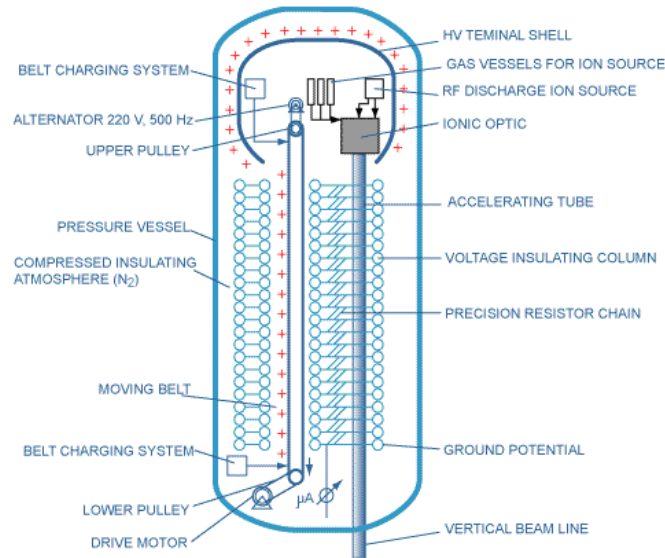

Figure 2.1: Schematic of Van De Graaff accellerator [63].

The ions are produced by a RF discharge ions source (Figure 2.2). The gases used for the ionization are contained inside the high voltage (HV) terminal of the accelerator. They are introduced selectively through thermomechanic valves, before being ionized by magnetic field at radio frequency, approximatively 100 MHz. The ions generated are then focalized on the extraction axis by magnets. The extraction electrodes allow the expulsion of particles toward the accelerator.
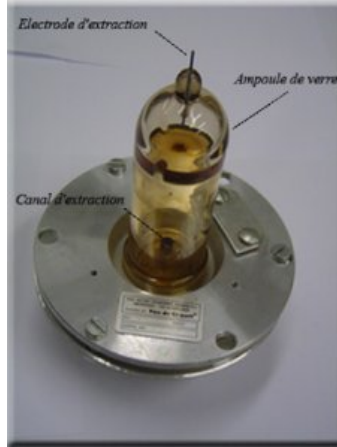
Figure 2.2: Schematic of the RF ions source. On the top of the glass ampule is visible the extraction electrode, while on the bottom there is the channel used for the extraction [64].

In Figure 2.1 we can see that the upper part of the column, the terminal, is gradually charged, by the charges generated on the lower part, they are accumulated and finally transported on dielectric belt. The terminal in such way results positively charged at high voltage. A precision resistor chain connects the system to the ground and creates an uniform potential gradient, that accelerates the ions toward the sample. The maximum accelerating potential is limited by breakdown across the accelerating tube and charge leakage from the high voltage electrode.
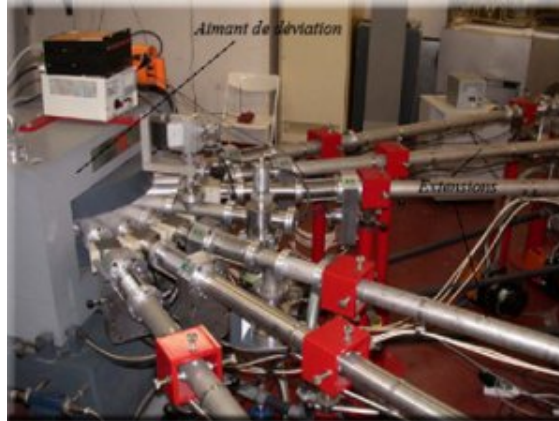

Figure 2.3: Schematic exit of the beam line deflected by electromagnets towards the detectors0. The arrow in the picture marks the position of the deviation magnet [64].

The beam is driven by an electromagnets towards six possible extensions and finally toward the different beam lines (Figure 2.3). The system can guarantee parallel beams of mono-charged and mono-kinetic particles like H+, He+ in an energy range from 100 keV up to 2.5 MeV [64]. The chambers connected with the ion beams are used for possible analysis such as RBS (Rutherford Backscattering Spectometetry), ERDA (Elastic Recoil Analysis Detection), NRA (Nuclear Reaction Analysis) and NRP (Nuclear Resonance Profiling).

2.2.2   Souce d'Ions Multichargés de Paris: SIMPA

SIMPA (French acronym for "Highly Charged ion Source of Paris") is an installation with Electron Cyclotron Resonance Ion Source (ECRIS) developed by Pantechnik society. It allows to generate highly charged ions beams at energy of several keV and transport them toward the sample through an ultra-high vacuum beam line. The most used types of ions are Oxygen of 1 at 8+, Ne from 1 to 10+ and Ar from 1 to 18+. The general scheme of the system is displayed in Figure 2.4.
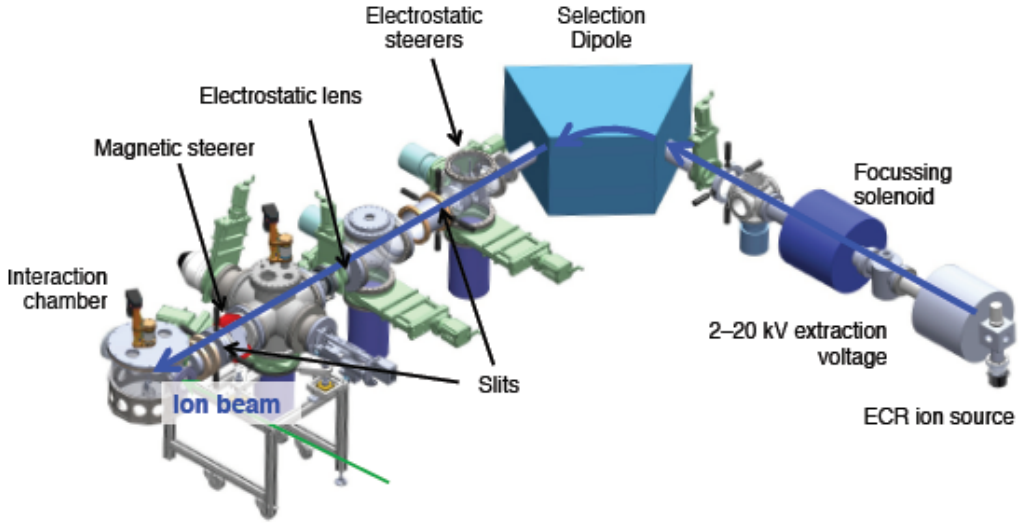

Figure 2.4: Scheme of SIMPA ions source [65].

The ions are generated in the plasma chamber. Ionized by subsequent collisions with fast electrons. The electrons are heated through micro-waves that have a frequency equal to the cyclotron resonance of the electrons in the magnetic field present in the plasma chamber. Permanent magnets (Fig. 2.5(a)), placed all around the plasma chamber in a hexapolar arrangement, allows radial confinement of the plasma while axial confinement is obtained through electromagnetic coils. Microwaves and gas, are guided by a cylindrical cavity to the plasma chamber. At the output of the source the extraction electrode (Figure 2.5 (b)) extracts the ions and imparts them an energy of the order of ten keV.
To check the operating stability of the source a mass quadrupole analyses the partial pressure of the residual gas. Once extracted, this beam is focused a first time using a strong magnetic field induced by a solenoid. Then, a magnetic dipole and a pair of slits perform a selection of the incident beam with respect to the charge-mass ratio values of the incoming ions. In such way ion beams containing a single charge state of a single chemical species can be obtained. Finally, a series of electrostatic and magnets deflectors and electrostatic lens guide and shape the ion beams into the interaction chamber [65, 66].
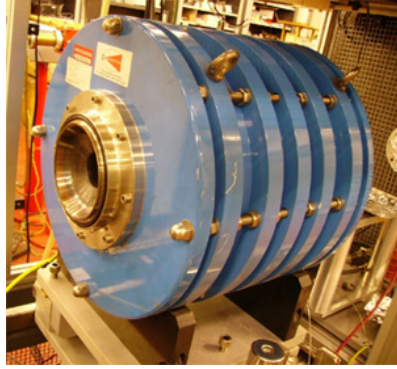
(a) Permanent magnets of the plasma chamber.
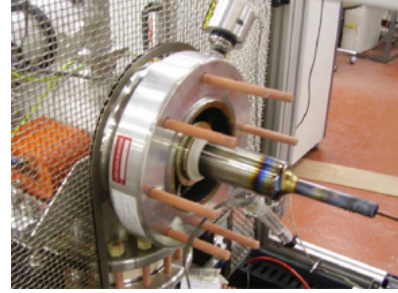
(b) Extraction electrode of SIMPA ion source.

Figure 2.5: Picture of SIMPA technical presentation [65].
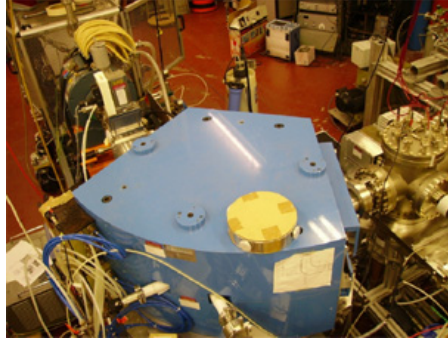
Figure 2.6: Magnets of analysis in the state of charge. The beam at the output of the magnetic dipole is then at 90 ° of the beam at the output of the source [65].

The system requires that the entire beam line is maintained under vacuum in order to prevent contamination and the capture of ions along the path. In our set up a turbo-molecular pump is used to obtain secondary vacuum of the order of 10^{-7} mbar.
With the aim of ensuring good irradiation conditions and in order to obtain a reliable estimation of fluence of the ions impinging the target, ion beam current is measured by two Faraday cages one located immediately after the analysis magnet and the other at the interaction chamber. In addiction to control the geometrical shape of the ion beam at the collision chamber, several patterns are mounted and the fluorescence on these targets is analysed using CCD camera.

2.3   Magnetic properties measurement

There are many methods for measuring the magnetic momentum. In general the sample in its environment produces a force a flux or indirect signal which is sensed by a detector and results in an electrical output signal in dc or ac. Depending on the types of response we can classify the technique into indirect and direct measurements. The indirect techniques involves microscopic measurement such as magnetic resonance, neutron scattering, analysis of the electromagnetic effect or microwave ferromagnetic resonance. The main problem of the indirect methods is the necessity of considerable prior knowledge about relationship between the response observed and the phenomenon occurring in the material. The direct technique, on the contrary, involves the direct analysis of macroscopic properties, flux and force, sensed by a detector [67, 68].
In our case we will analyse the evolution of the average magnetization (emu) exploiting just direct techniques. The magnetization properties of the sample will be measured under different conditions, of magnetic field and temperature. Because of the different measurement methods, the measurements of magnetization dependency over the magnetic field or temperature are better exploited in two different types of magnetometers [69]. The vibrating sample magnetometer (VSM) will be used to analyse the magnetization dependency on the magnetic field, while the superconducting quantum interference device (SQUID), will be used in the other case.

2.3.1   Vibrating Sample Magnetomer:VSM

The VSM has been one of the most popular magnetometer for more than the two decades. It allows to measure, with high sensitivity and high stability, the magnetic momentum of magnetic materials (even weakly magnetic) by inducing the sample in vibration in the presence of a homologous magnetic field.

A schematic of the instrument structure is shown in Figure 2.7. The sample is inserted into the magnetometer by means of long sample holder vibrating drive head by a non-magnetic rod Figure. Inside of the instrument the sample is suspended in a region of dc magnetic field produced by an electromagnet. The vibration unit put the sample in oscillation. The specimen vibrations are at known frequency, in our case 40Hz, parallel to the applied dc magnetic field. According to Faraday law, the motion of the sample causes a variation of the magnetic flux and this latter produces a distortion of the field detected by the detection coils, a pair of counter-wound and balanced coils located in the proximity of the sample. In order to keep the frenquecy and the amplitude of the sinusoidal motion constant is used a capacitor, which also acts as a reference signal generator. The electrical signal induced in the detection coils is proportional to the frequency and amplitude of the sinusoidal motion, the magnetic response of the sample to the applied magnetic field, and a geometrical factor that takes into account the surface area of the detection coils and their distance from the sample. Finally the output signal is extracted by means of phase-sensitive lock-in detection [67].

Cryogenic temperatures are required both for measurements at low temperature and

because of presence of superconducting elements. A warm-up from liquid nitrogen to room temperature can be extended for several days, lower temperature can be achieved by liquid helium reservoir. The resulting temperature working range is from 2 to 350K.
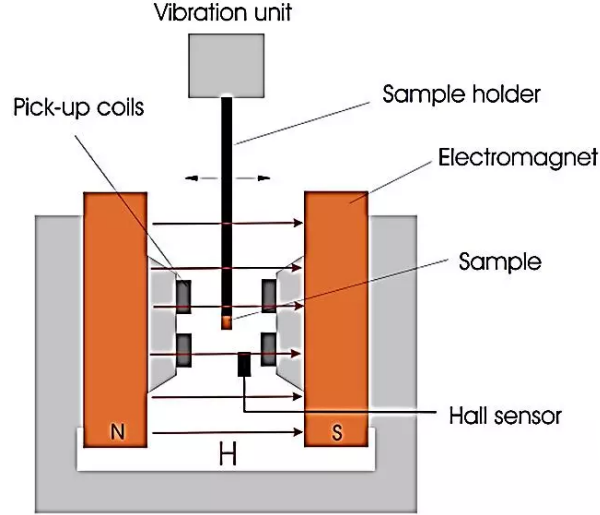

Figure 2.7: Schematic of VSM structure [70].

The sensitivity of the instrument is 10^{-6} emu. The main causes of noise, that limits the performance of the device, is the Johnson noise of the wired used for the coils. In addiction the use of minimal mass of weakly diamagnetic material for sample holder is essential to avoid noise. The main problem of this device is due to the request of an uniform magnetic field because it is difficult to correct the effect of nonuniformities [67, 68].

The VSM can be used for both measurement of the magnetic momentum as function of the temperature as well as function of the magnetic field. The field change is quite fast in isothermal condition (0.9 T/s), on the contrary the temperature variation results slower, because of the long time required for the thermalization of the device (more precisely between the temperature sensor and the sample). The VSM will be used to study the magnetic properties as function of the magnetic field. An example of this magnetometer application can be found in the study of the phase diagram of MnFePSi-sample in the chapter 4.

The standard procedure for isothermal measure by VSM is the following. Before the start of the process the sample is brought to a complete paramagnetic phase at high temperature (in our cases 350K), this ensures the elimination of any residual magnetization from previous measurements. After this, the sample is brought at desired temperature and the magnetic momentum is recorded, increasing the magnetic field in the range between 0 and 10T and 10 to 0T. Several magnetic cycles can be studied at different fixed temperature, in each case the residual magnetization is cancelled out bringing the sample in the paramagnetic phase with zero field applied.

2.3.2 Superconducting Quantum Interference Device: SQUID

The Superconducting Quantum Interference Device (SQUID) is one of the most sensitive device for the measure of magnetic flux. The detection is carried on in a superconducting ring with two Josephson junctions. If two superconducting regions are separated by a resistive barrier, for a distance less than the coherence length, with a current less than the critical current I_c, electrons can tunnel from one region to the other with no voltage drop. On the contrary if the current is higher respect the critical one, we can measure an additional potential drop. This effect is known as Josephson effect.
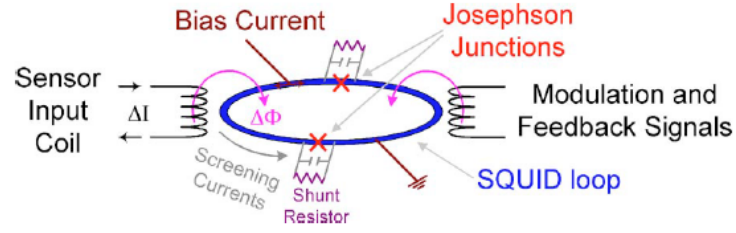

Figure 2.8: Dual juction SQUID loop. The capacitor represents the self capacitance.
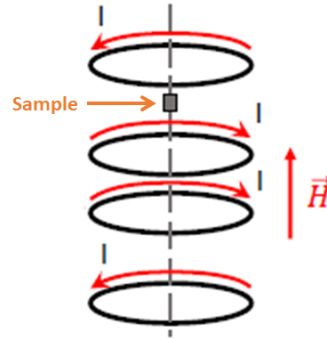
Figure 2.9: Schematic of the 4 superconducting detection coils system. The two coils at the centre have the wire wrapped around the same direction the other two coils have the wire wrapped in the opposite direction [71].

In figure 2.8 a schematic of the SQUID loop is displayed. The junctions are biased with alternating or continuous current I_b, in our analysis we will refer just to DC technique. The bias put the operation point of the Josephson between the superconducting and resistive behaviour. The shunt resistor is used to prevent the hysteric behaviour. Fixing I_b at slightly higher value than I_c, when an external magnetic flux is coupled into the loop, the voltage drop across the junction change periodically with period equal to the quantum flux $\phi_0 = h/2e$. The used magnetometer is based on four SQUID loops that detect variations of the magnetic field, Figure 2.9. The sample moves inside the four system coils and its motion induce a variation of the magnetic flux detected by the detection coils. This signal

is sent to SQUID loop that converts the magnetic flux change into voltage variation at the output of the instrument. Through the analysis of the voltage change, the magnetic momentum of the sample is extracted [71, 68].

In Figure 2.10 the complete structure of the device is shown. The superconducting detection loop array is rigidly mounted in the centre of homogeneous superconducting magnet. This latter generates an uniform field over the entire sample and induces a moment allowing a measurement of magnetic susceptibility. The sample temperature is regulated using a heater, located below the sample, and a thermometer located above. The cryogenic temperature is obtained through helium gas, obtained from evaporation in the Dewar. The flow rate is regulated by a precision valve. Thanks to these arrangements the analysis of the magnetic properties can be performed in a range from 1.8K to 400K for the temperature and from 0 to 7T for the magnetic field. The sensitivity of the instrument is quite high equal to 10^{-8} emu.
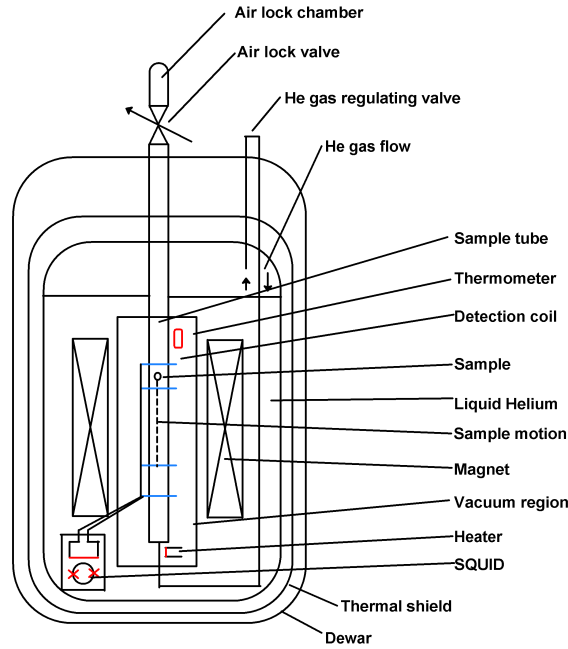
Figure 2.10: Typical structure of SQUID magnetometer [72].

The SQUID magnetometer will be used to analyse the magnetic momentum of the samples as function of temperature variation and constant field. In order to collect coherent measurements a standard procedure has to be followed. Each sample starts at initial temperature $T_0 = 350$K and a magnetic field $H = 1$T is applied. At this point it is performed a scan at ascending and descending temperature to record the magnetic momentum of the material and measure the thermal hysteresis associated, the velocity of the scan is chosen in a range from 0.5 to 8K/min.

The SQUID magnetometer is a sensitive and versatile device, but in order to obtain the most accurate measurements it is necessary to pay attention to some points [72]:

- The main cause of parasitic magnetic signal is due to the sample holder, for this reason it is important to define a proper technique to mount the sample. In first place it is necessary to choose a material with low magnetic susceptibility. In our case the sample is inserted through a plastic straw. The sample is first immobilized, according to the magnetic moment alignment, by threading a cross of white cotton thread. Using a needle of non-magnetic-metal we thread some cotton through the tube walls and tie a secure knot so that the thread platform is rigid. Then an additional thread cross the top to hold container in place.

- The sample length should not exceed 10 mm and it is important to keep the sample susceptibility constant over its length, otherwise the signal results to be distorted.

- The sample must be centred otherwise the coils read just partially the magnetic momentum. It is required to start the measure with centring procedure in which the instrument scans the entire length of the sample vertical travel path.

When the sample holder background contribution is similar to the one of the sample signal, the relative position of the sample and the material produce a noisy output signal. The combination highly distorts the result which is no more a characteristic of the dipole moment of the sample. In the following section 2.4 the procedure to correct this effect will be explained.

Performing the analysis of the magnetic momentum as function of the temperature by SQUID with different temperature sweep rates, we discovered that the temperature recorded during the cooling was a bit higher respect the real one of the sample. The method developed to correct the results will be explained in the section 2.5.

2.4   Correction of SQUID noisy measurements

The measurements performed at SQUID magnetometer can be strongly modified because of unconsidered movements of samples inside the instrument, wrong alignment or sample holder contribution to magnetic moment. In such cases data have to be corrected.

The Figure 2.11 represents the bad quality of the measure of the magnetic momentum dependency on temperature of MnAs-sample.

Figure 2.11: MnAs magnetic momentum measured after the annealing process as function of the temperature. The red curves are obtained when the temperature decreases, the blue curves instead represent the increasing temperature condition.
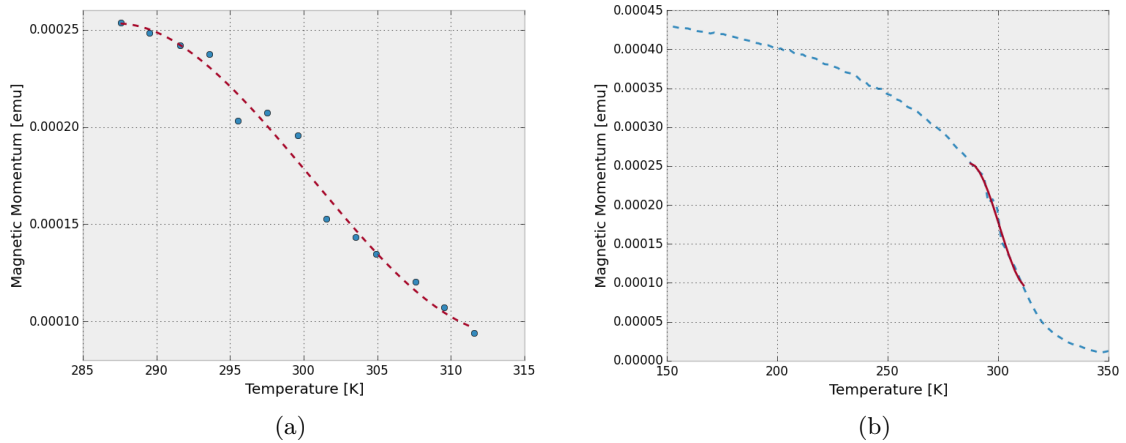
Figure 2.12: Focus on the cooling curve M(T):
(a) One-dimensional smoothing spline fit (red-dashed line) for a given set of points (blue dots)
(b) Magnetic momentum behaviour restored after the correction.

(a)   (b)
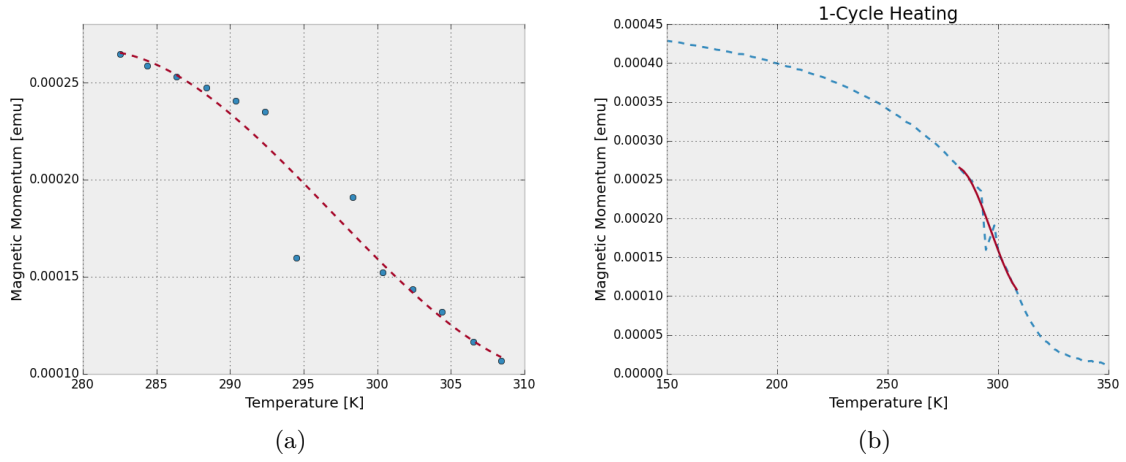
Figure 2.13: Focus on the Heating curve M(T):
(a) One-dimensional smoothing spline(red-dashed line) for a given set of points (blue dots)
(b) Magnetic momentum behaviour restored after the correction.

The measured points describing a wrong behaviour of the magnetizations are considered in a larger interval. The sets of points selected in such range are used to fit the curves by a spline both for the cooling (Figure 2.12) and heating (Figure 2.13) branch. These adjustments results in a proper computation showed in Figure 2.14.
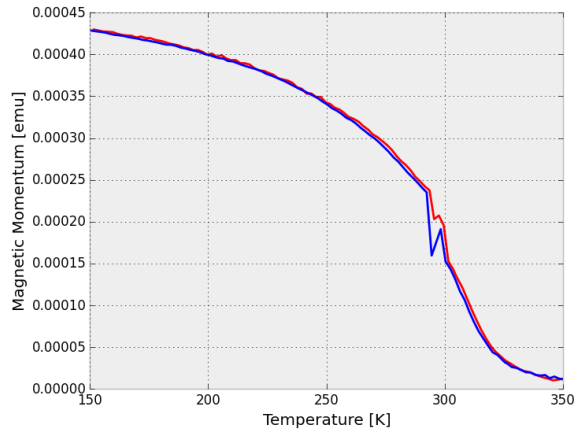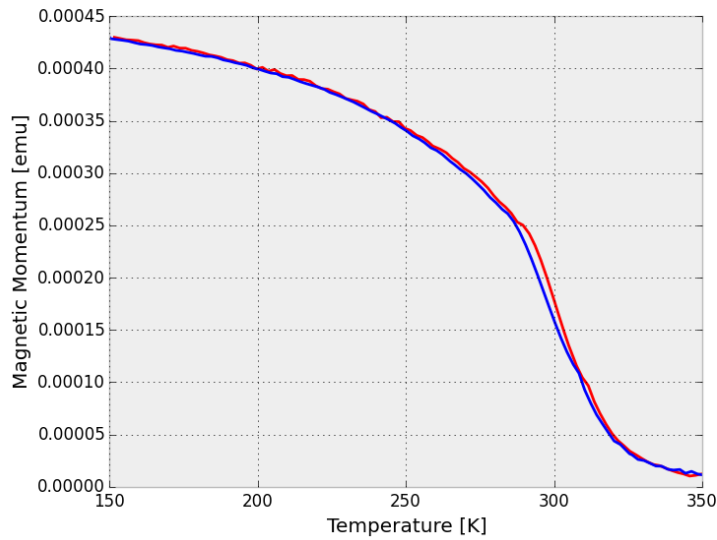

Figure 2.14: Corrected magnetic momentum measured after the annealing process as function of the temperature. The red curves are obtained when the temperature decreases, the blue curves instead represent the increasing temperature condition.

39

2.5   SQUID temperature corrections

For the investigations of the modifications of magnetocaloric materials submitted to the bombardment of highly charged ions, the sample magnetization dependency on temperature is obtained through SQUID magnetometer. As explained in the previous sections, the SQUID is a superconducting device that requires cryogenic temperature to operate. In order to ensure a stable cooling with no time varying magnetic signature, the thermal environment for the sensor and detection coil is helium and nitrogen contained in a vacuum insulated vessel known as Dewar.

The figure 2.10 shows the structure of the device. The distance between the sample and the detection coils can cause a slight mismatch between the temperature read T_{read} by the sensor and the real temperature of the sample T_{real}. This small error can lead in the worst case to negative values of the area of the hysteresis, inverse hysteresis Figure 2.15. In such cases two curves of the plot of the magnetization as function of the temperature are swiped each other. Since the reverse hysteresis is a phenomena difficult to explain through the physical process involved in our experiments, it could be useful verify if temperature has been calculated properly in each case.
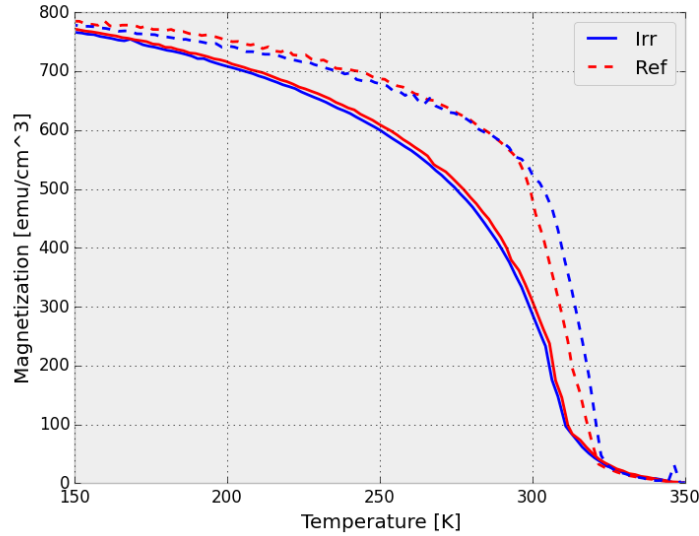
Figure 2.15: Magnetization of the reference (dashed-line) and the irradiated sample (continuous-line) as function of the temperature. Data are obtained by temperature increase (blue) and decrease (red). The reverse hysteresis is visible in the irradiated sample which present the two curves (blue and red) swiped respect the reference.

The aim of this chapter is to show some corrections adopted with the SQUID temperature measurements, and to explain the procedure followed to obtain the correction factors.

2.5.1 Analysis of the sweep rate

The magnetic dependency of the temperature of the sample is computed through a standard sequence. The measurement procedure starts with each sample initially brought to $350K$ with null magnetic field, after that cooled down to 100K applying a field H=1T . The magnetic moment is recorded continuously during the temperature variation from 100K to 350K, usually with a sweep rate ± 2 K/min. Since the measurement is reproducible, we can assume that for a fixed value of the magnetization corresponds a fixed value of the temperature of the sample (taking into account also the direction of temperature change). In order to verify the reliability of the process, we repeat the procedure using different values of sweep rate and we try to extrapolate the real value of the temperature of the sample.
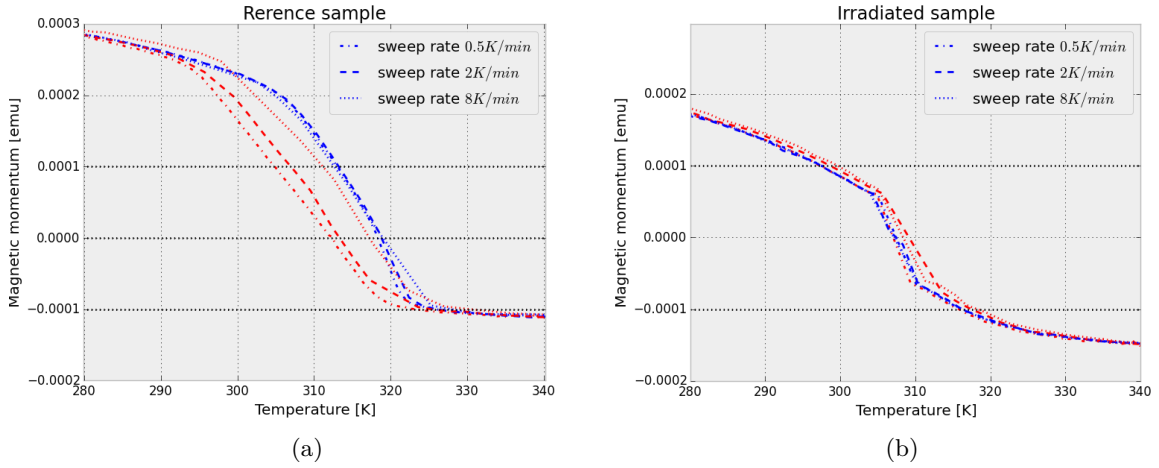
Figure 2.16: Magnetic momentum dependecy on temperature at different sweep rates for the reference(a) and the irradiated sample (b). The blue curves are obtained by increasing the temperature, reverse condition for the red curves. The black dashed lines point out the values of magnetization used for the analysis.

Figure 2.16 displays our choice of M(T) to calculate the read and the sample temperature at velocity v_{ref} = 0.5 K/min, 2 K/min, 8 K/min for the reference and at v_{irr} = 0.5 K/min, 2 K/min, 4 K/min, 8 K/min for the irradiated sample. The normal hysteresis is well visible in the reference sample while it results being reversed in reverse sample irradiated at high fluence. In Fig 2.16, it is interesting to note as the error in the temperature seems not to involve both of the branches, in fact if the blue curves (representing the increasing of the temperature) follow almost the same path, while the red ones (decreasing temperature) are considerately shifted each other.
A dashed line evidences the values of magnetic momentum taken into consideration, respectively $M = 0$ emu/cm^3 and $M = \pm 10^{-3}$ emu/cm^3 in the first case and
$M = \pm 10^{-3}$ emu/cm^3 in the second one (the points $M = 0$ emu/cm^3 is not taken for the irradiated sample because these latter measurements have been strongly modified around that 0-point, due to the undesired movement of the sample in the magnetometer).

Our aim is to determine from an extrapolation to an individual swipe velocity $v = 0$ the real temperature. We can consider the real measurement T_{real} as a variation of the read value T_{read}: $T_{real} = \Delta T + T_{read}$.

ΔT is a correction term that can be written as $\Delta T = av$ where $a(T)$ is a correction coefficient function of the temperature and v is the sweep rate. When the velocity is equal to 0 is evident that the read value becomes equal to the real one.

From this argument it is easy to understand the following step: the temperatures obtained at different magnetic momentum is plotted as function of the sweep rate at which they have been measured and the points collected in such way are used to extract the $a(T)$ and $b(T)$ parameters of the first-order fit $y = ax + b$.
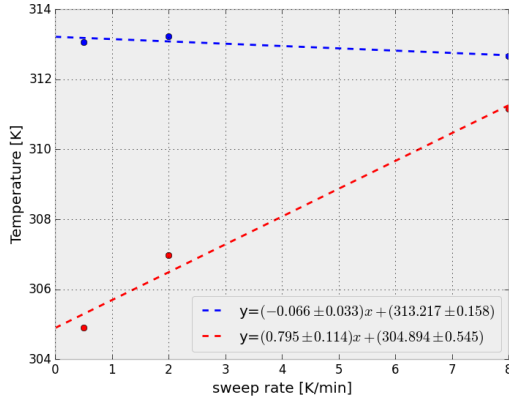
(a) $T_{ref}(v_{ref})$ *when* $M_{ref} = 10^{-3}$ *emu*
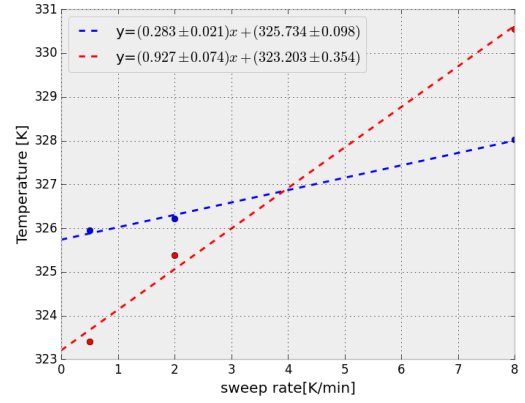
(b) $T_{ref}(v_{ref})$ *when* $M_{ref} = -10^{-3}$ *emu*
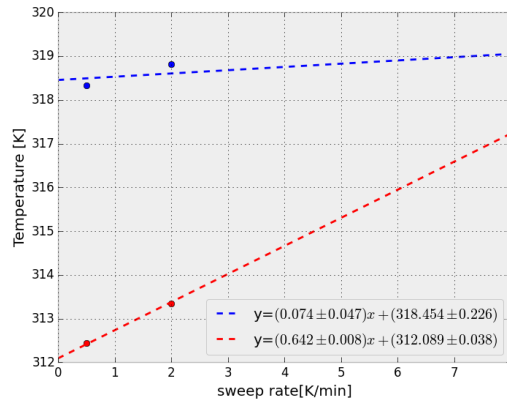
(c) $T_{ref}(v_{ref})$ *when* $M_{ref} = 0$ *emuu*

Figure 2.17: The blue (heating condition) and the red (cooling condition) dots represent the temperature of the reference sample at fixed magnetic momentum for different velocity $0.5\ K/min$, $2\ K/min$, $8\ K/min$. Through the values collected the first order fit-lines have been calculated, displayed as dashed-lines.

(a) $T_{irr}(v_{irr})$ when $M_{irr} = 10^{-3} emu$

(b) $T_{irr}(v_{irr})$ when $M_{irr} = -10^{-3} emu$
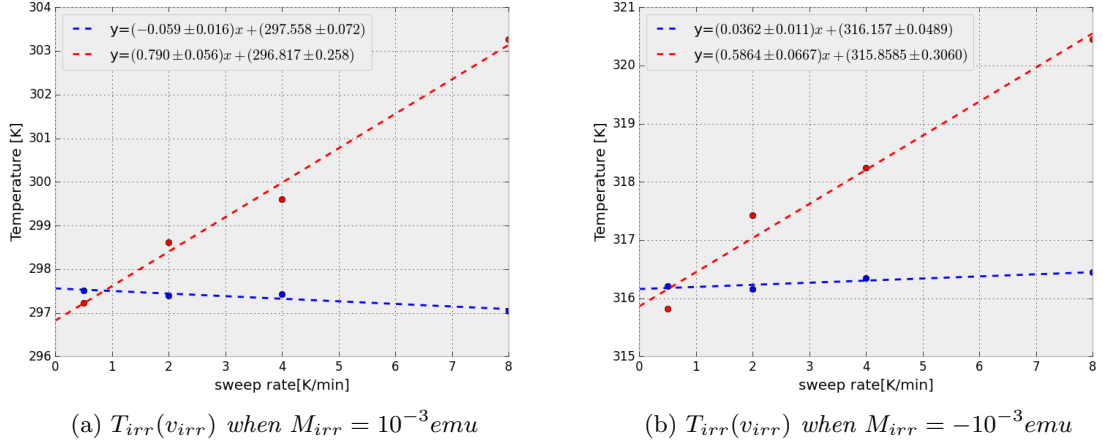
Figure 2.18: The blue (heating condition) and the red (cooling condition) dots represent the temperature of the irradiated sample at fixed magnetic momentum for different velocity 0.5 K/min, 4 K/min, 2 K/min, 8 K/min. Through the values collected the first order fit-lines have been calculated, displayed as dashed-lines

From the different magnetic momentum we obtain the results presented in Figure 2.17 and 2.18. From the fit results the parameter $a(T_{real})$ and $b(T_{real})$ can be determined. In fact $b(T_{real}) = T_{real}$ by constatation while $a(T_real)$ is unknown. We used the different results relative to different real temperatures to determine a possible depending of a in T_{real}. For this purpose the real temperature b is plotted as function of the correction coefficient a in Figure 2.19.

(a) *Temperature decreasing*

(b) *Temperature increasing*
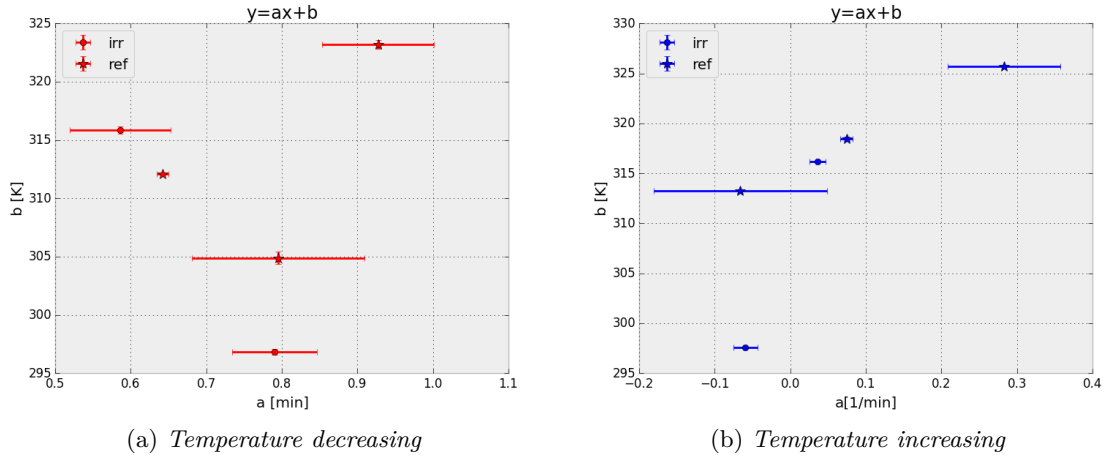
Figure 2.19: The real temperature b is studied as function of the correction coefficient a. The reference (star-points) and the irradiated sample (rounded-points) data are plotted together to get a more clear information about their distribution

43

The reference and the sample are considered together, separating as usual the cooling case (red) from the heating one (blue). The errors of a and b ae derived by the result of the singular fit.

The results do not show regular trend (Figure 2.19) and at the same time the uncertainties are very different each other. For this reason we can pragmatically consider that the temperature correction is constant for this range of temperatures $\Delta T = a(T) * T = a * T$. The value of a is considered to be equal to the average of the values and its error given by the standard deviation:

$$\sigma = \sqrt{\frac{1}{N-1}\Sigma d_i^2} = \sqrt{\frac{1}{N-1}\Sigma(x_i - \overline{x})} \tag{2.1}$$

where N is the number of points considered, x_i is the *ith* measure and $\overline{x}$ is the average value 2.1.

2.5.2 Results

| Correction coefficient	Cooling curve	Heating curve
Average value	-0.7482 min	+ 0.0537 min
Absolute error	$\pm$ 0.1335 min	$\pm$ 0.1418 min

Table 2.1: Summary of the correction coefficients average and uncertainties.

Table 2.1 resumes the results obtained from the analysis of the cooling curve and the heating one. From a quantitative point of view it is clear that the two cases are not equivalent, incoherent temperature evolution comes out when the sample is cooling. This is not an unexpected result, it was already evident in Figure 2.17 and Figure 2.18, in that case the blue curves were almost flat compared with the red ones and we know the slope identifies the difference between the real (0-velocity) and the read value. Due to the small heating-adjustment the measurement will is assumed to be correct, while the real temperature in cooling condition will be: $T_{real} = T_{real} + av$, substituting

$$T_{real} = T_{read} + v(-0.7482 \pm 0.1335) \tag{2.2}$$

The equation 2.2, is written in unusual way taking into consideration the errors associated to the correction. In fact the final validity of the method can be obtained by plotting the same result presented at the beginning of the section (Figure 2.15) including the temperature uncertainties. Figure 2.20 shows how the red branch of the measurement is shifted to the right respect the original one, this lead to the elimination of the reverse hysteresis artefact in the irradiated sample. The error associated to the correction is really small and can be pointed out just through a zoom Figure 2.21. Even if not very large this contribute will be taken into account when studied the error associated to the area of the hysteresis.
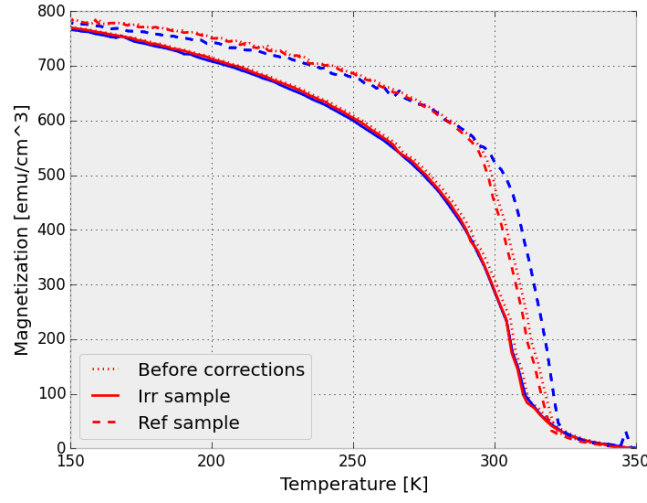
Figure 2.20: Magnetization of the reference (dashed-line) and the irradiated sample (continuous-line) as function of the temperature are presented before and after the corrections (pointed-lines). Data are obtained by temperature increase (blue) and decrease (red), respectively ferromagnetic-paramagnetic transition and paramagnetic-ferromagnetic transition. The reverse hysteresis has been corrected since the irradiated sample have no more the two curves (blue and red) swiped respect the reference.
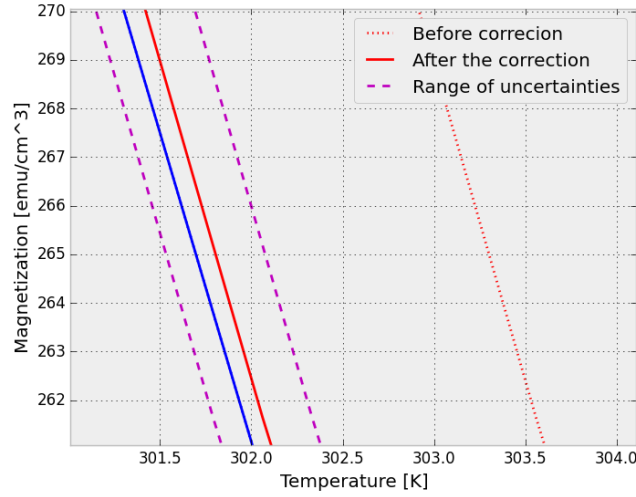
Figure 2.21: Zoom on the correction of the irradiated sample poits out the range of incertitudines of the methods

Chapter 3

Modification of manganese arsenide properties

In this chapter we present an investigation on giant magnetocaloric properties of MnAs. It will start describing the characteristics of the massive material and after the considerations will be adapted to the analysis of thin film epitaxially grown. The experimental method will be briefly explained considering both the growth and irradiation procedure. The central core of the chapter will be the corrections of data collected in a previous Ph. D. thesis. The corrections are relative to the measurement of the area of the sample and the temperature dependency of magnetization measured in a SQUID magnetometer. It will be demonstrated with these modifications, that new aspects of the magnetic behaviour of the material subjected to irradiation, will emerge especially in the evaluation of the magnetization at condition of saturation and in the calculation of the area of the hysteresis. After that, an investigation of the samples subjected to annealing process bring new insight on the nature of the defects. At the end, a summary of the results describes the conclusions obtained, and the future perspectives.

3.1   Bulk material properties

Manganese Arsenide is a metallic compound characterized by different polymorphic transformations that influence its properties both from the structural and magnetic point of view. Starting from a low temperature condition the material is characterized by an hexagonal ferromagnetic structure: α-phase. Through a first order transition at $T_c = 313K$ the configuration is modified into an orthorombic paramagnetic β-phase. Since both the magnetic and the structural properties of the materials change, this transition is defined as magneto-structural.
The transition is accompanied, as said, by a distortion of the lattice parameters and as consequence a reduction of the 2% of the volume [73, 74, 75] (Figure 3.1). Measurement as function of the temperature shows that the c lattice parameter increases with the temperature leading to an increment in the length of the lattice.

Further increment in the temperature can lead the structure to change again back into hexagonal paramagnetic γ-phase, through a second order transition at $T_c = 398K$.
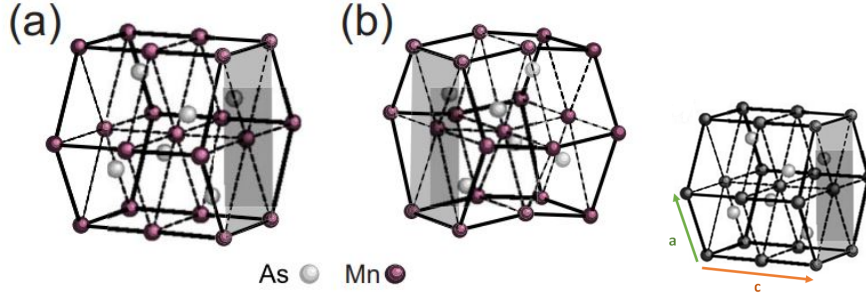
Figure 3.1:
(a) Hexagonal α- phase T<313K
(b) Orthorombic β-phase 313K<T<398K

This latter reconfiguration is defined as structural transition, since the material is paramagnetic in both β and γ phases.
The change between the α and β is associated to a variation of the magnetic properties. By plotting the magnetization as function of the temperature Figure 3.2 is evident that the magnetization during the magneto-structural transition reaches its maximum at low temperature, in a stable ferromagnetic configuration. By increasing the temperature there is a abrupt decrement of the magnetization, at the same time the volume decreases and on the contrary the electrical conductivity increases. Since the critical temperature in the para-ferromagnetic transition is not equal to the critical temperature in the ferro-paramagnetic case, it is possible to define a thermal hysteresis, that is a common characteristic of first order transformations.

The large change of magnetic entropy ΔS_{magn}, in proximity of the first order phase transition close to room temperature, is responsible to a large refrigeration power. From the Chapter 1 we remember that the refrigeration power is defined as the integral of the change in entropy in a defined temperature range.
Figure 3.3 displays the change in magnetic entropy as function of the temperature. The huge variation of the magnetization at the transition temperature (Figure 3.2) is related to a large variation of the magnetic entropy in a small temperature range. The peak height is not very sensitive to magnetic field change, whereas the peak width increases nearly linearly with the field.

Figure 3.2: MnAs magnetization dependency on temperature at different fields [76].

Figure 3.3: MnAs change in magnetic entropy as function of the temperature caused by a magnetic field [76].

3.2   Thin film analysis

The MnAs used for the investigation is not a bulk material but a thin film epitaxially grown on a GaAs substrate. This choice modifies the properties of the material.
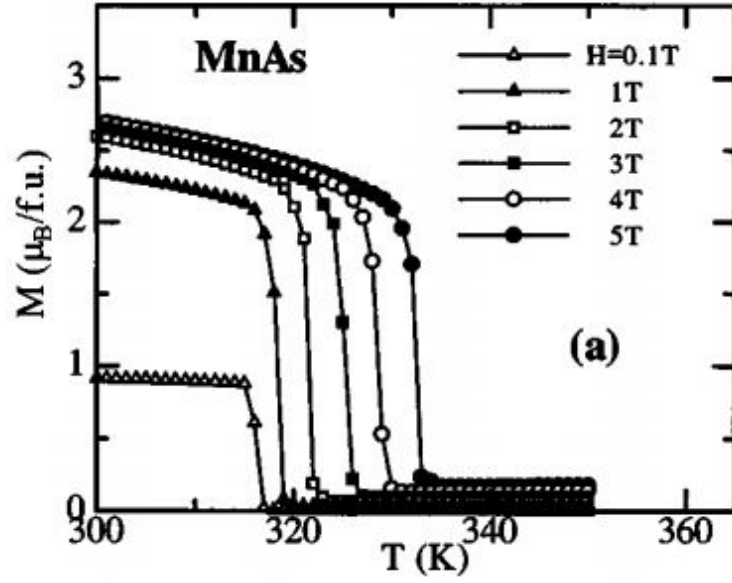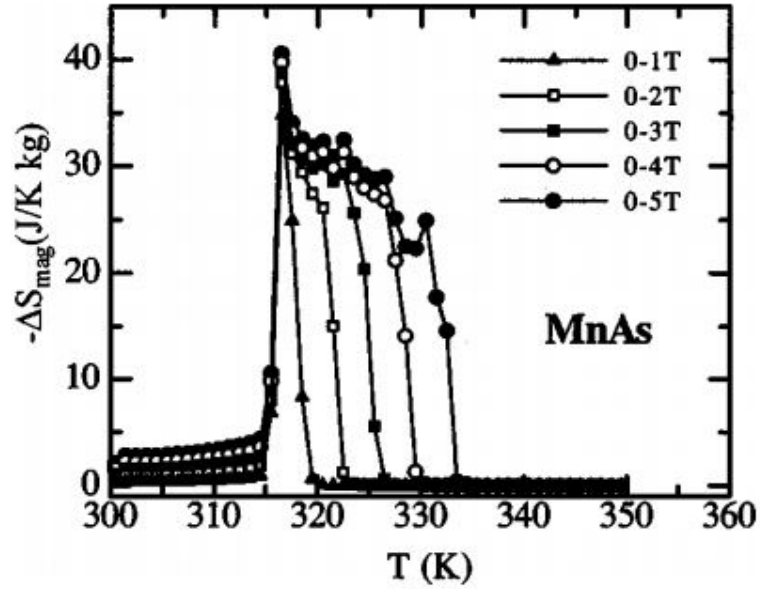The samples were prepared on laboratory following the procedure described in the Ref. [77]. A layer is grown by molecular beam epitaxy (MBE) on GaAs. This latter is characterized by face centred cubic structure with (001) orientation. The deposed MnAs is oriented with α-MnAs[001] and β-ManAs[001] axis parallel to GaAs[001]. To prevent the oxidation and the degradation at the end of the growth process samples are capped in situ with an amorphous As-layer about 10 nm thick. The resulting sample is considered monocrystal and characterized by a final thickness of $150 \pm 10 nm$

The constraints of the substrate cause a $\alpha - \beta$ coexistence in the temperature range of 290 - 320 K. Scanning probe microscopy (SPM) and scanning tunneling microscope (STM), used in this wide interval of temperature, reveal that the material generates a self-organization in longitudinal stripe-shape-regions of α and β phases. The period λ of the organization depends linearly on the MnAs thickness t according to the relation $\lambda = 4.8t$ [78].

(a) *Pure α-phase*   (b) *α-β stripes pattern*   (c) *Pure β-phase*
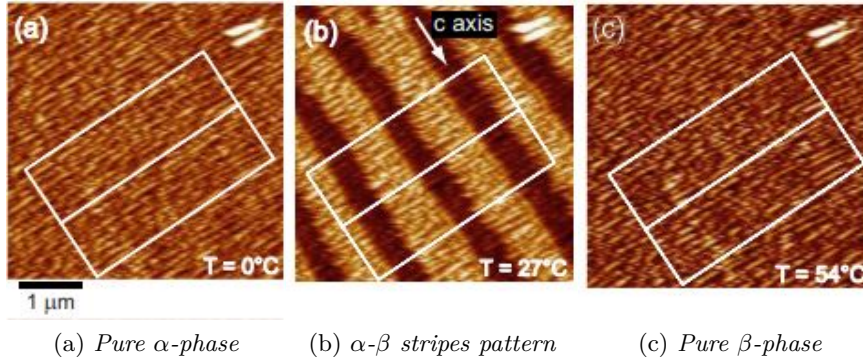
Figure 3.4: Surface-morphology evolution captured by STM at different temperature. The bright regions corresponds to α-phase, on the contrary the β-phase is represented by the dark zones [77].

The reason of this behaviour is the following: in an epilayer the lateral size is clamped by the substrate that induces an in-plane strain while the out plane parameter is free to relax, but by heating the sample the β-phase helps the system to release and minimize its energy.

The phase coexistence causes modifications of the thin films magnetic properties:

- First of all, since the transition inside the material from α to β phase is gradual, even the magnetic transition is less sharp respect the bulk material, where the structural composition changes abruptly.

- Secondary the thermal hysteresis results to be smaller.

- Third and last consequence, the maximum value of entropy change $\Delta S(T)$ is four time smaller, but since the range of transition temperature is larger, the refrigeration power is kept constant. In other words the MCE is preserved from the high quantity of ΔS per mole of material portion passing from one phase to the other.

3.2.1   Irradiation

The samples presented in this chapter can be categorized according to the type of irradiations they were subjected, leading to a different mechanism of interactions in the process of defects generations. The thin films were modified by two different types of instrumentations at two different laboratories: at Institut des NanoSciences de Paris (INSP) the electron-cyclotron ion source at SIMPA facility were exploited for irradiation with low-velocity ions while samples were irradiated at the IRRSUD beamline at the GANIL facility accelerator for irradiation with high-velocity ions.

In the first case the thin films were subjected to different types of ions (Ar,Kr,Ne,H,O). The conditions for the irradiations were defined through SRIM simulations to ensure the implantation of the particle in the thin films and the preservation of the substrate. The kinetic energy of the beam was precisely defined in a range 22-260keV (depending on the ion type) by varying the extraction voltage. The uniform generation of defects in the whole sample volume, as uniform as possible, is ensured by the choice of the incident angle from the interval from 0 to 60 degrees, with the average penetration depth of the ions corresponds to the half thickness. The fluence value was change in the range $[10^{12} - 10^{15}\text{ions/cm}^2]$ and it was measured in situ during the irradiation by an array of micro-Faraday coups coupled to a visible-light CCD camera (further information in Ref. [1, 79]).

In the second case, the ion source used isotropic ^{36}Ar-beam accelerated at 35.28 MeV. Uniform irradiations are obtained by swapping the ion beam over the samples. The angle between the ion beam and the surface was kept fixed at 0 degrees. The fluence varied in an interval from 10^{12} to 10^{20}ions/cm^2. The main difference from the procedure described above is that, due to the reduced thickness of the sample and the fast particles, no ions were implanted in the MnAs thin film.

Another remarkable difference between the two irradiation campaigns is that the interaction process, involving slow ions bombardments at SIMPA, is dominated by elastic nuclear collision, while fast ions process is governed by electron stopping power. It is better to precise that for the high-velocity case the leader mechanism is the inelastic interaction between electrons that cause an increment of the temperature, but nuclear collisions are always present.

3.3   Correction of data

The goal of this part is the corrections of the data that were pre-analysed during a previous Ph.D.[1]. The information relative to the magnetization of the samples at different temperature were affected by two types of errors. First of all the surface area of the samples were almost systematically overestimated by an imprecise measurement. As consequence, wrong considerations were obtained in the evaluation saturation value of the magnetization. Secondary, the sample temperature measured at SQUID magnetometer were biased respect the real one depending on the cooling or heating process of the sample. This error caused a wrong estimation of the area of the hysteresis and in the worst case the hysteresis resulted reversed.

The process for the correction of the values will be presented in the following two subsections. In parallel the analysis of MnAs will underline the new aspects of the magnetic properties of the material.

3.3.1   Surface area correction

The area of the sample in the precedent analysis was estimated with an approximated measurement using millimetric paper as reference and where the details of the surface condition were not visible. In particular, in more accurate observations it was possible to notice missing MnAs thin film parts on the substrate. In order to eliminate this imprecisions the surface value can be approximate by exploiting an imaging software of a calibrated optical microscope.

(a)   (b)
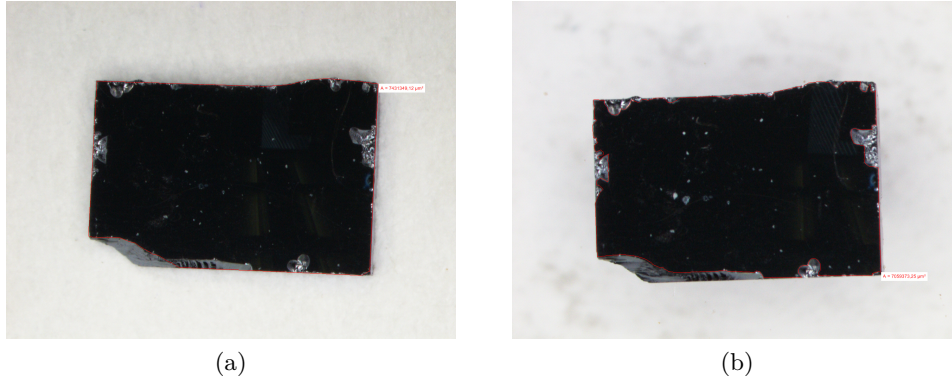
Figure 3.5: Two pictures of the sample 21 obtained at microscope hypotizing different contributes in area of the sample, marked in red.

In Figure 3.5 (a) and (b) the same sample is captured by the stereoscopic microscope and the surface area is evaluated through the related software *NIS-Elements D*. The efficiency of the new method consists in the possibility of measuring the surface area several times without varying the set-up of the instrument. A more precise analysis of the structure allows to estimate which defects actually influence the volume of the sample .

Analysis of the magnetization at saturation

The revaluation of the surface area caused a variation in the measurement of the magnetization, being this last one obtained by the measurement of the total sample magnetic moment divided by the volume of the sample, the magnetization in the most of the case is increased after the correction of the area measurement. The most important consequence is evident in the magnetization saturation value. In order to analyse the effect of the corrections we consider the evolution of the magnetization as function of the temperature before and after irradiation in two cases.

- The first case, represented by Figure 3.6, are chosen samples irradiated at low energy by argon ions but at difference levels of fluences ($3.64 * 10^{11}$, $3.46 * 10^{13}$, $1.9 * 10^{13}$ and $8.59 * 10^{14}$ ions/cm^2).
  Analysis considering the irradiation of samples at increasing level of fluence, demonstrate that higher is the number of impinging particles, better is the suppression of the hysteresis, on the other hand, excessive fluence causes deterioration of the magnetic power of the material resulting in a decrease of the slope of the curve. In our investigation we show that in condition of high level of fluence even the saturation value of the magnetization is not preserved 3.7 (c) and (d), probably due to strong perturbation in crystal lattice.

- In the second case, represented by Figure 3.7, samples irradiated with ions of different masses (Kr, Ar, Ne, O and Ne) but with same fluence (10^{13}ions/cm^2) at energy range [22-260keV] are considered.
  Previous studies, collected in Ref. [1], demonstrated that even if smaller hysteresis was observed with more massive ions, these latter causes a stretch of the curve leading to a decrease magnetic power of the material. On the other hand here we show that materials keep the same saturation value before and after the bombardment considering irradiation with both light (Fig 3.7 a, b, c) and heavy ions (Fig.3.7 d, e).
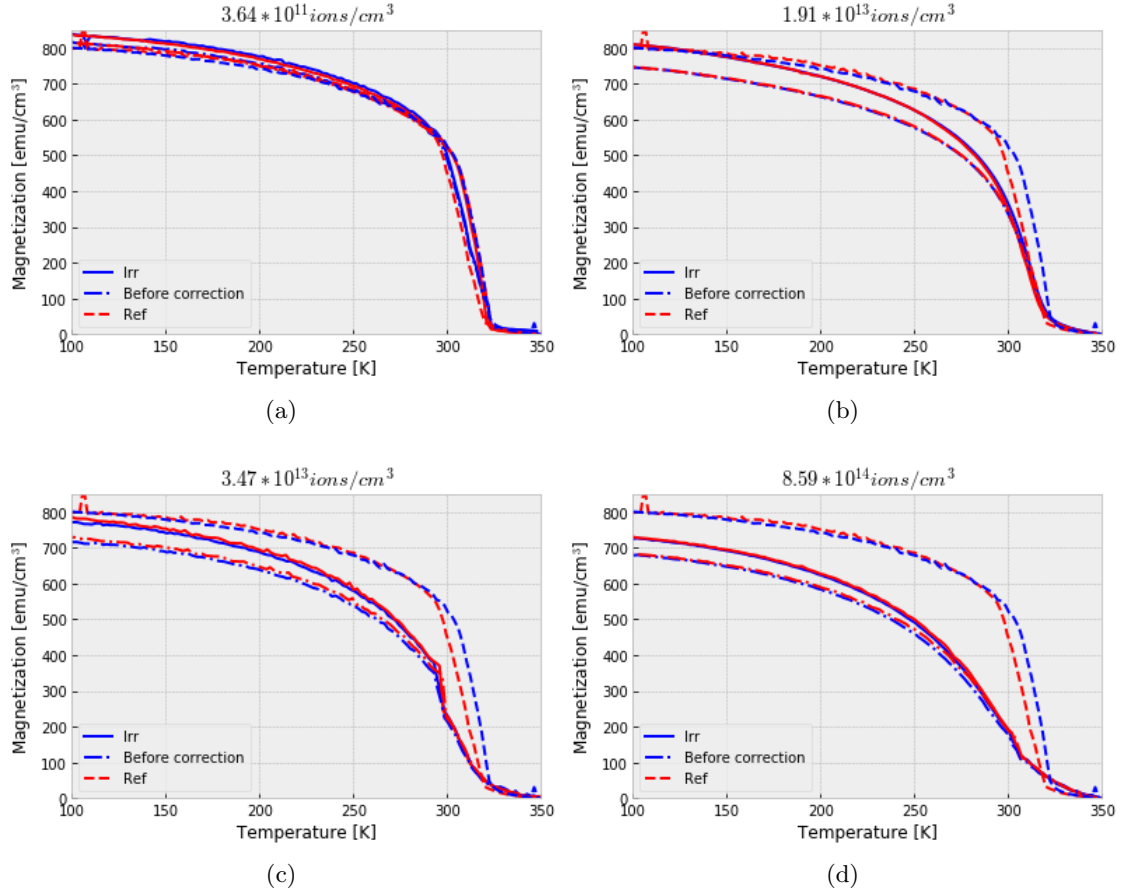
Figure 3.6: Magnetization is measured as function of the temperature for difference fluences of Ar-ions, magnetic field equal to H=1T, ion kinetic energy in the range 208keV. Blue lines process at increasing temperature, red lines process at decreasing temperture, respectively ferro-paramagnetic transition and para-ferromagnetic transition. The plot compares the results before and after the correction in the irradiated and the reference sample.

Figure 3.7: Magnetization plotted as function of the temperature for 5 different types of ions (He,O,Ne,Ar and Kr) at fluence equal to 10^{13}ions/cm^2 and a magnetic field constant at 1T energy in range 25-300keV corresponding to an average ion penetration equal to the half of the film thickness. Blue lines process at increasing temperature, red lines process at decreasing temperture. The plot compares the results before and after the correction in the irradiated and the reference sample.

3.3.2 Temperature correction

In the chapter 2 we have seen that the measure of the temperature by the SQUID magnetometer is affected by an error. This leads to an uncorrected representation of the magnetization as function of the temperature itself. In this chapter we will apply the correction discussed previously and we will analyse the consequences on the area of hysteresis. The entire method of correction will be explained by using an example: sample 17. The same procedure was applied to each sample.

Sample 17 is a MnAs thin film irradiated by O-ions at 84keV with a fluence equal to $1.34*10^{13}$ ions/cm^2. Its magnetization as function of the temperature is displayed in Fig. 3.8. As we have seen in the chapter 2, the temperature read results higher respect the real one when material is cooled (dashed red line). In the same chapter we have demonstrated that it is possible to correct the curve as follows $T_{real} = T_{read} - v(0.75 \pm 0.13)$, where v is the sweep rate in our case equal to $2K/min$. The modification is applied in Figure 3.8 as represented by the continuous red curve.
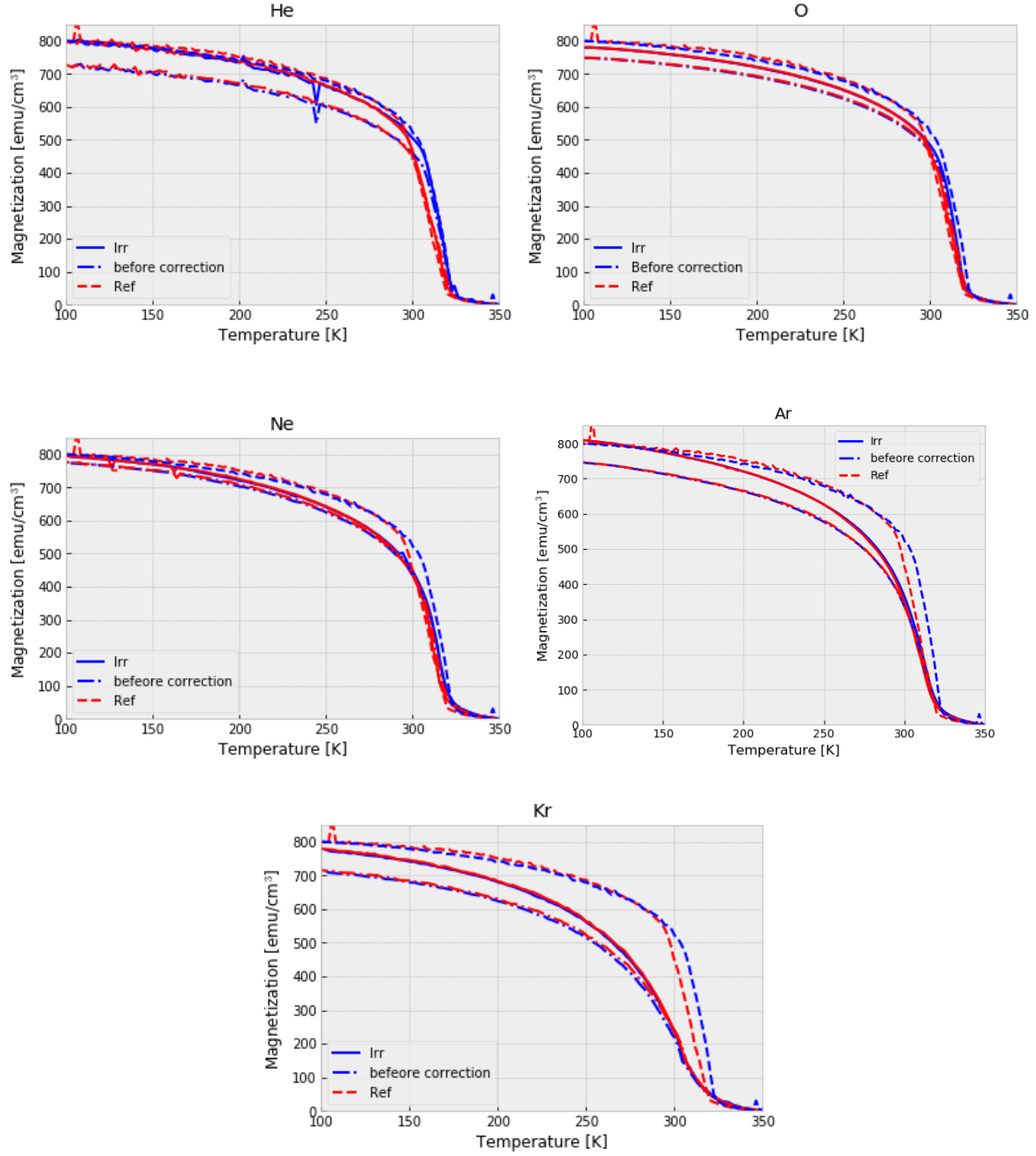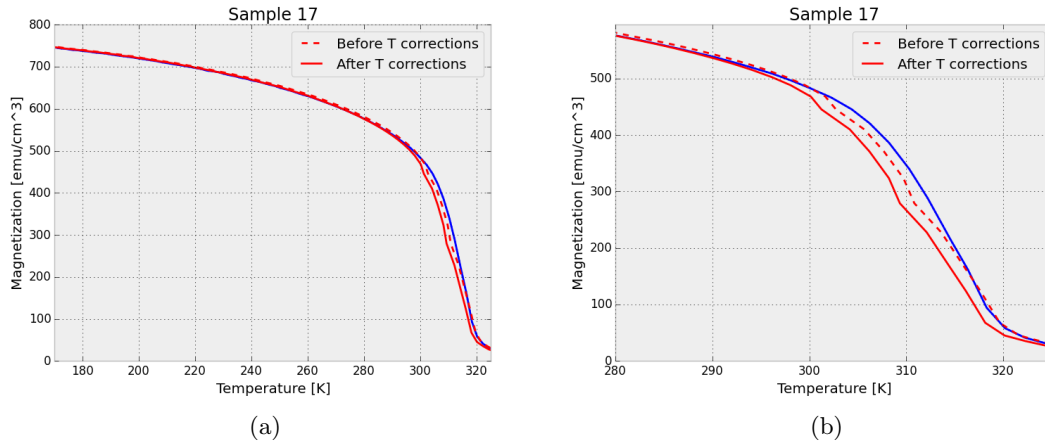

Figure 3.8: (a) Magnetization as function of the temperature of the sample 17 and zoom on the hysteresis (b). The measurement is represented before (dashed line) and after (continuous line) the temperature correction. The red and blue curves are respectively the cooling and heating branches.

The right shift of the cooling curve of the magnetization avoids the possibility of reverse hysteresis but as natural consequence modified the area between the two curves as well evident in the zoom of figure 3.8 (b). A new computation of the area of the hysteresis is then required to include error evaluation related to the applied correction and uncertainties.

In order to ensure that the area between the two functions is closed and not excessively affected by possible noise of the data collected, three different temperature intervals are considered for the interpolation. The first interval is small and includes the measurement collected in the temperature range from 288K to 325K (Figure 3.9 (a)) . The value 325K

56

is not arbitrary but it is a specific value at which in each sample the hysteresis results null. By lowering the temperature a second range of interpolation is defined from 250K to 325K (Figure 3.9 (b)), at 250K most of the samples have the hysteresis area already closed but to consider every case a third interpolation interval is considered from 170K to 325K (Figure 3.9 (c)). The point at 170K is a good compromise that ensures the closure of the hysteresis even in extreme cases, without including possible noise occurring at low temperature saturation.
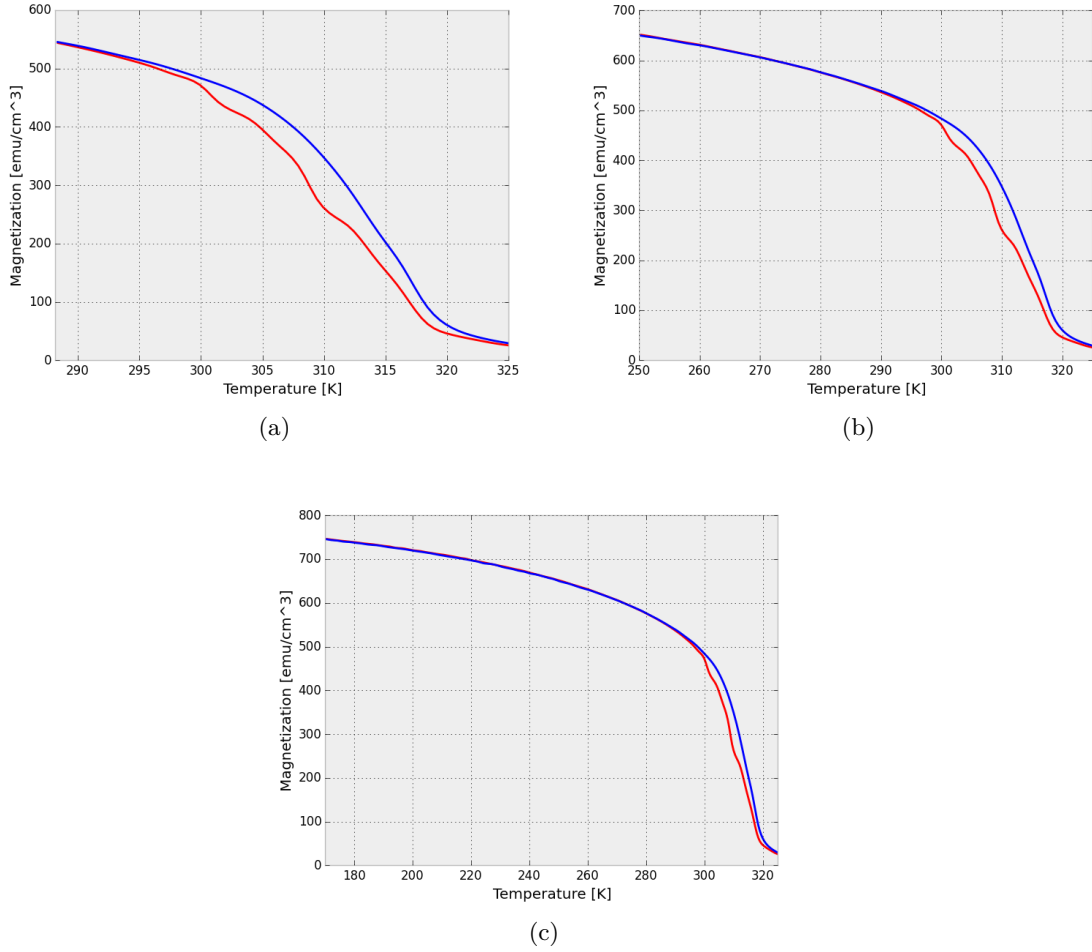
Figure 3.9: (a) $288-325K$, (b) $250-325K$, (c) $170-325K$ interpolation intervals considered for the M(T) curves.

In each range the integral, as approximated by the trapezoidal rule is used to calculate the area under the cooling and heating curve, the difference between the two integrals gives us the area of the hysteresis. Finally, an average value and estimation of the uncertainty will be calculated considering the results of the three different cases.

To define the final error associated to calculation we have also to consider the uncertainties related to the temperature correction. In Figure 3.10 the magnetization as function of the temperature is presented already corrected, the uncertainties, violet dashed lines, display the interval in which the position of the red curves can vary and that can change the value of the area of the hysteresis.
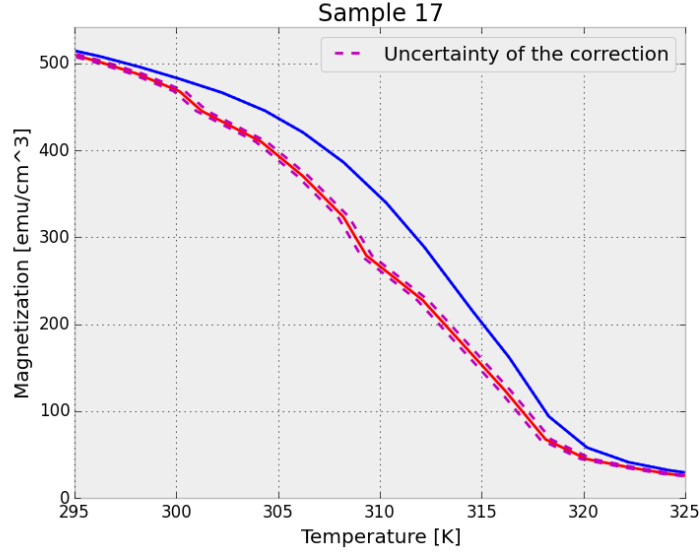
Figure 3.10: Magnetization as function of the temperature of the sample 17. In red and blue are displayed respectively the cooling and heating curves while the dashed violet lines represent the uncertainties associated to the correction in temperature.

We repeat the computation of the area considering the uncertainties. The results will be increasing in the case of negative contribution (farther left shift possible) and decreasing in case of positive one. Since the final hysteresis area value is obtained from the algebraic average between the maximum and minimum obtained value, the associated error is obtained from their difference divided by two. The final value of the hysteresis area A is determined from the values of A, obtained from different temperature ranges, and by applying temperature corrections $\Delta T + \delta(\Delta T)$ or $\Delta T - \delta(\Delta T)$. As example for sample 17, we report the corresponding values in Table 3.1.

Area Sample17 $[emu * K * cm^3]$					
T correction	**288-325K**	**250-325K**	**170-325K**	**Average**	**Error**
$T_{real} = T_{read} - av$	1065.93	1061.01	975.69	1034.21	
$T_{real} = T_{read} - av + \delta$	806.19	747.89	988.94	847.67	300.78
$T_{real} = T_{read} - av - \delta$	1065.93	1061.01	1349.45	1158.80	

Table 3.1: Area of the hysteresis of the sample 17 calculated for the three intervals of interpolation and considering the uncertainties in the temperature correction.

The table resumes the corrected data for each sample is presented below Figure 3.11.

Sample	Type of ions	Corrections	Area hyst [emu*K*cm^3]		Volume [cm^3]	Ions density [ions/cm^3]		Collision density [coll/cm^3]		Fluence [ions/cm^2]		Energy kinetic [keV]
			avg	error avg	volume	ions-den	err-ions	coll-den	err-coll	fluence	err-fluence	
2	Ne	With	606,655	306,7155	1,03E-06	4,96E+19	2,48E+19	7,11E+22	3,55E+22	1,00E+15	5,00E+14	90
		Without	-981,182	-148,927	1,03E-06							
9	Ne	With	539,2374	260,3133	5,46E-07	7,44E+17	3,72E+17	1,07E+21	5,33E+20	5,33E+20	7,50E+12	90
		Without	-550,206	451,7575	1,22E-06							
16	Ar	With	499,2329	376,6217	1,30E-06	1,04E+18	5,19E+17	3,47E+21	1,74E+21	1,91E+13	9,57E+12	208
		Without	-93,9667	145,7684	1,41E-06							
17	O	With	1034,215	300,7816	1,15E-06	6,70E+17	3,36E+17	7,18E+20	3,60E+20	1,34E+13	6,74E+12	84
		Without	-55,2912	164,6972	1,19E-06							
18	He	With	123,7962	434,5582	1,43E-06	2,63E+20	2,74E+19	3,26E+22	3,39E+21	5,76E+15	6,00E+14	22
		Without	-779,579	318,0836	1,53E-06							
19	He	With	1993,135	562,6644	6,25E-07	1,49E+18	2,73E+17	1,85E+20	3,38E+19	3,27E+13	5,97E+12	22
		Without	288,3256	418,2159	6,90E-07							
20	O	With	107,4649	419,0796	5,90E-07	7,30E+19	8,94E+16	7,82E+22	1,28E+20	1,46E+15	6,60E+13	84
		Without	-745,221	218,6858	6,54E-07							
21	Ne	With	914,3541	320,8494	1,06E-06	6,54E+17	8,94E+16	9,37E+20	1,28E+20	1,32E+13	1,80E+12	89,6
		Without	21,777	133,2128	1,14E-06							
22	Ne	With	-303,149	403,5114	1,06E-06	5,34E+18	5,70E+17	7,66E+21	8,17E+20	1,08E+14	1,15E+13	89,6
		Without	-983,262	-263,022	1,23E-06							
23	Ne	With	-548,543	837,4027	5,81E-07	4,48E+19	7,09E+18	6,42E+22	1,02E+22	9,03E+14	1,43E+14	89,6
		Without	-1597,28	-654,335	6,59E-07							
24	O	With	-38,0762	528,1451	7,74E-07	1,01E+19	2,76E+18	1,08E+22	2,95E+21	2,02E+14	5,53E+13	84
		Without	-1637,89	-633,688	8,45E-07							
25	Ne	With	4245,004	375,6557	3,14E-07	2,52E+16	3,37E+15	3,61E+19	4,83E+18	5,08E+11	6,79E+10	90
		Without	2226,783	792,4935	3,47E-07							
26	Ar	With	-456,768	659,4192	3,86E-07	1,89E+18	1,30E+17	6,31E+21	4,33E+20	3,48E+13	2,39E+12	208
		Without	-1826	-735,02	4,16E-07							
27	Ar	With	2460,525	324,4844	6,94E-07	1,97E+16	1,19E+15	6,60E+19	3,98E+18	3,64E+11	2,20E+10	208
		Without	734,7809	401,6081	7,25E-07							
28	Ar	With	-444,016	539,735	9,16E-07	4,65E+19	3,85E+18	1,56E+23	1,29E+22	8,59E+14	7,10E+13	208
		Without	-876,296	-211,122	9,79E-07							
29	Kr	With	-219,367	369,5898	6,18E-07	5,24E+17	7,47E+16	2,69E+21	3,84E+20	8,00E+12	1,14E+12	260,1
		Without	-774,502	132,2639	6,80E-07							
30	Kr	With	-462,435	502,2113	4,98E-07	9,36E+18	3,93E+18	4,82E+22	2,02E+22	1,43E+14	6,00E+13	260,1
		Without	-1046,13	-342,148	5,01E-07							
31	Kr	With	240,4156	486,3837	6,78E-07	9,17E+16	4,58E+16	4,71E+20	2,36E+20	1,40E+12	7,00E+11	260,1
		Without	-655,994	-43,7409	7,36E-07							
32	Ar*	With	2177,422	292,5132	9,41E-07	//	//	4,83E+19	2,41E+18	4,00E+12	2,00E+11	7800
		Without	1456,405	112,0625	9,41E-07							
33	Ar*	With	1122,63	268,6625	8,16E-07	//	//	2,41E+20	1,21E+19	2,00E+13	1,00E+12	7800
		Without	157,1523	49,16806	8,16E-07							
34	Ar*	With	-123,942	492,4231	1,05E-06	//	//	1,21E+21	6,03E+19	1,00E+14	5,00E+12	7800
		Without	-735,68	186,496	1,05E-06							
REF	Ref-2018	With	3799,284	555,9903	6,69E-07	//	//	//	//	//	//	//
		Without	3242,378	529,4048	6,69E-07							
REF	Ref-2012	With	2697,56	612,0594	1,16E-06	//	//	//	//	//	//	//
		Without	1590,945	634,0328	1,16E-06							

Figure 3.11: This table resumes conditions at which the materials were irradiated and the results obtained. The first eighteen materials have been modified at SIMPA. The Ar-samples marked with asterisk are the ones irradiated with high energy at GANIL facility. The last two specimens are two different reference sample used characterized in different years to check on the stability of the sample in time.

Analysis of the area of the hysteresis

New values of the area of the hysteresis require new analysis. For this purpose, we will follow almost the same path of the investigation of the causes of the suppression of the hysteresis used in the previous Ph.D. work on this topic. We hope that the corrected values will show more insights of the main mechanism of the process.

In a first moment of investigations, it was believed that the principal causes of the reduction of the hysteresis was the presence of ions implanted into the material. From these considerations the choice of the ion energy at SIMPA facility for having the average penetration depth of the ions equal to half of the sample thickness. However, a regular behaviour of the area of the hysteresis was not found as shown in Figure 3.12.
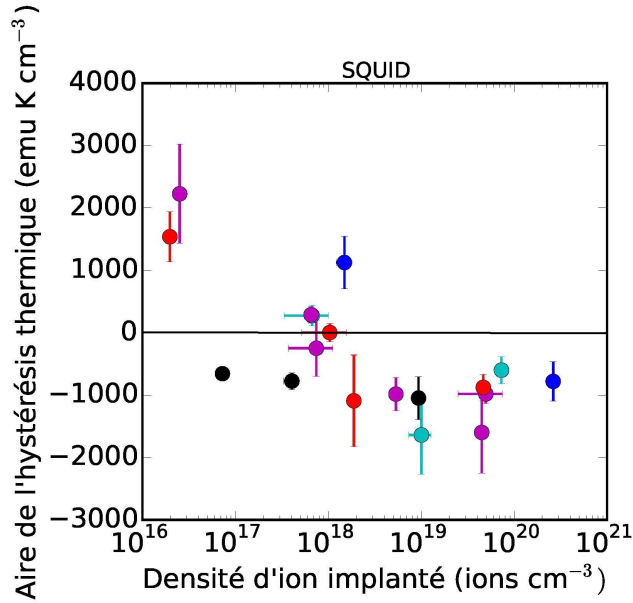

Figure 3.12: Area of the hysteresis versus the density of ions implanted considering the irradiation by five different types of ions (He, O, Ne, Kr, Ar). Results are obtained before the corrections.

Following the same idea we display the corrected area of the hysteresis versus density of ions implanted in Figure 3.13 to see if a more clear trend emerges. We can note that the reverse hysteresis has been corrected in most of the samples and even in that case in which the area has negative values the related uncertainties allows us to conclude that the reverse hysteresis is just an artificial effect due to wrong measurement of the temperature. In the corrected data neither regular trend is present that means that implantation plays no roles in the suppression of the hysteresis.
In Figure 3.13 we can see another important fact, as marked with yellow dashed lines the hysteresis is reduced in samples irradiated with Ar ions highly accelerated. In these cases the implantation of ions is not present while we can still consider the nuclear collisions between the nuclei ions and target atoms.

Figure 3.13: Area of the hysteresis versus the density of ions implanted considering the irradiation by five different types of ions (He, O, Ne, Kr, Ar) irradiated at low energy. As further comparison yellow dashed lines represent the value of density of hysteresis obtained by Ar-irradiation at high energy. The violet bar defines reference uncertainties range. Results obtained after the corrections.

Figure 3.14: Area of the hysteresis versus the density of collisions considering the irradiation by five different types of ions (He, O, Ne, Kr, Ar). Results are obtained before the corrections.

In figure 3.14 are shown the previous results of the investigation of area of the hysteresis as function of the density of collisions. The set of corrected data in Figure 3.15, including the irradiation both at high (star-points) and low energy (round-points), generates a regular disposition according to the density of collisions generated. For each type of ions, higher is the amount of collisions, higher is the reduction of the hysteresis. At certain value of the density of collision the thermal hysteresis is completely suppressed and the behaviour of the curves results in a plateau close to the zero value of the area without unnatural negative values present in the previous analysis.
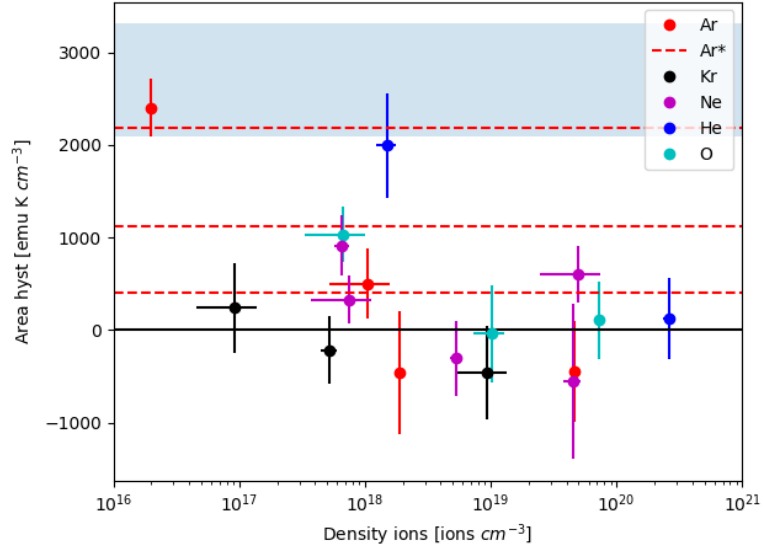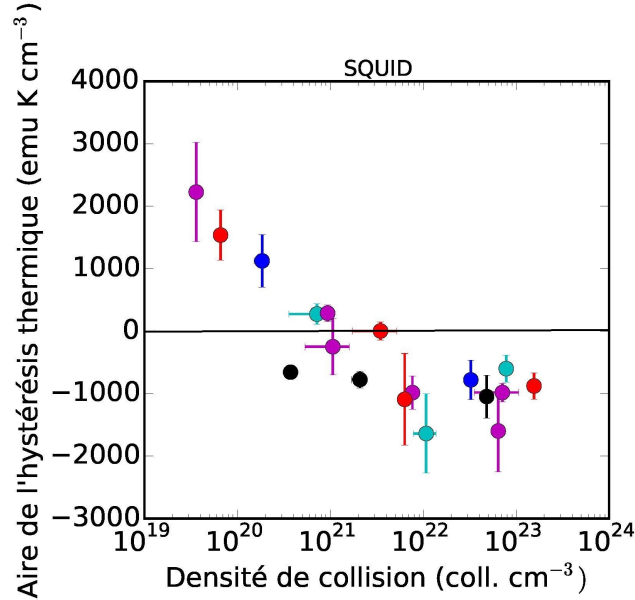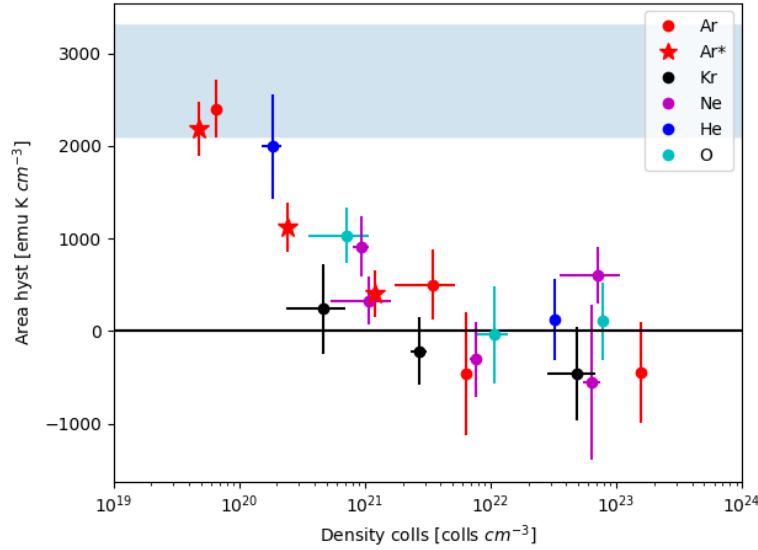

Figure 3.15: Area of the hysteresis versus the density of ions implanted considering the irradiation by five different types of ions (He, O, Ne, Kr, Ar) irradiated at low energy. The star points represent the value of the area of the hysteresis obtained by Ar-irradiation at high energy. The violet bar defines reference uncertainties range.

It is interesting to investigate if the density of collisions is the parameter leader in the process of suppression of the hysteresis, for this purpose we compare the irradiation obtained with the two isotopes of argon ions, the one highly accelerated at GANIL and the one used at SIMPA.

We can start considering irradiation at different fluences. In Figure 3.16 is shown the area of the hysteresis as function of the fluence in the two cases. The star-points represent the results obtained at high energy bombardment while the reverse condition (low energy irradiation) is marked by simple points. For ions with the same kinetic energy, higher fluence causes a more efficient suppression of the hysteresis. On the other hand comparing the outcomes at different energies this assumption is not always true, for example the star-point at fluence equal to 10^{14}ions/cm^3 is associated to a lower hysteresis respect the point at 10^{13}ions/cm^3. This indicates that the fluence has an important role in the experimental set-up but it is probably not the key parameter of the hysteresis reduction of the process.
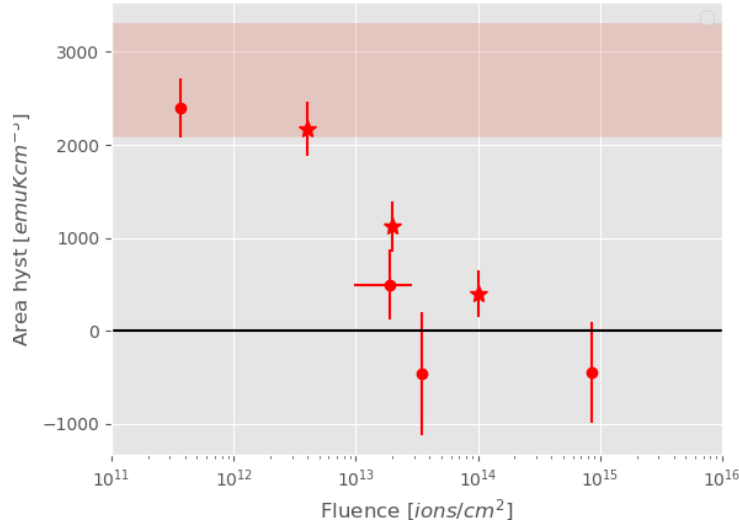
Figure 3.16: Area of the hysteresis versus density of collisions. Irradiation at high energy (star-points) and low energy (round-points) using Ar-ions.
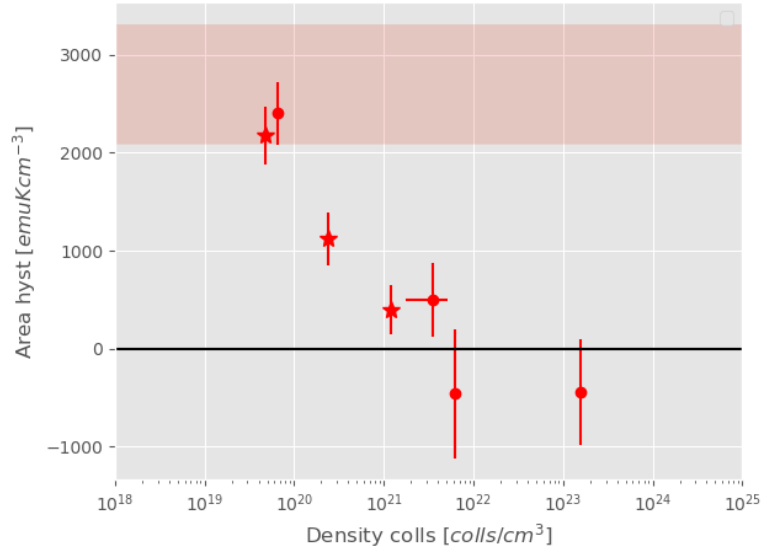
Figure 3.17: Area of the hysteresis versus density of collisions. Irradiation at high energy (star-points) and low energy (round-points) using Ar-ions.

As second approach we can test the dependency of the two irradiation as function of the density of collision: Figure 3.17. Differently from what was observed at different levels of fluence higher is the density of collisions, smaller is the associated hysteresis. This assumption results always true even if we consider the example used before, it is evident

63

that the star point at fluence equal to $10^{14} ions/cm^3$ has a lower hysteresis respect the point at fluence $10^{13} ions/cm^3$ because the first has a lower $(1.21 * 10^{21}\ colls/cm^3)$ density of collision respect the second one $(6.31 * 10^{21}\ colls/cm^3)$.

3.4   Study of the defects

In the first order transitions, the passage from one phase to the other requires to overcome the nucleation energy barrier between the two minima of the Gibbs energy corresponding to the two phases. The presence of barrier causes presence of phenomena like metastability and hysteresis. The irradiation induced defects act as nucleation sites to facilitate the transition between one phase to the other causing the suppression of the hysteresis. However, the exact nature of the defects responsible for this suppression is still not clear.

To investigate the nature of the induced defects, we study their stability against temperature treatment (annealing). We consider here just some samples corresponding to the irradiation performed at SIMPA. We remember that due to the energy range [22 keV-260 keV] at which the samples were subjected, the predominant interaction processes between the beam and the target are nuclear collisions. These mechanisms lead to the generation of lattice disorder through point-like defects such as implantations, displacement of atoms and productions of vacancies. Thermal treatment can partially recover the defects and test the robustness of the modifications induced by irradiations.

Sample	Type of ions	Area hyst [emu*K*cm^3]		Volume [cm^3]	Ions density [ions/cm^3]		Collision density [coll/cm^3]		Fluence [ions/cm^2]		Energy kinetic [keV]
28	Ar	-444.016	539.735	9.16E-07	4.65E+19	3.85E+18	1.56E+23	1.29E+22	8.59E+14	7.10E+13	208
20	O	107.4649	419.0796	5.90E-07	7.30E+19	8.94E+16	7.82E+22	1.28E+20	1.46E+15	6.60E+13	84
23	Ne	-548.543	837.4027	5.81E-07	4.48E+19	7.09E+18	6.42E+22	1.02E+22	9.03E+14	1.43E+14	89.6
30	Kr	-462.435	502.2113	4.98E-07	9.36E+18	3.93E+18	4.82E+22	2.02E+22	1.43E+14	6.00E+13	260.1
18	He	123.7962	434.5582	1.43E-06	2.63E+20	2.74E+19	3.26E+22	3.39E+21	5.76E+15	6.00E+14	22

Figure 3.18: The table resumes the conditions of irradiation of the samples. After the bombarding the sample have been subjected to annealing process

The table, in figure 3.18, is a summary of the samples chosen for the annealing process. Among the several thin films we choose the ones subjected to higher fluence, because they are the ones more modified by the irradiation.
The annealing process was performed under helium atmosphere at a temperature of 400K for about two hours. This temperature has been chosen because i) modifications of samples properties have been observed when treated to 400 K and ii) this temperature can be obtained within the SQUID magnetometer. To note, in a period of several years no sign of sample properties changes has been observed for temperatures equal to 350 K or lower. The sample magnetic properties of the materials were measured before and after the thermal treatment through SQUID magnetometer.

3.4.1   Results

The samples, that we are going to investigate, were irradiated at high fluency ($10^{14} - 10^{15}$ions/cm^2) with 5 different types of ions. The relative magnetization behavior as function of the temperature is displayed in the Figure 3.19.

Before being thermal treated the magnetic properties of sample irradiated at high level of fluence are characterized by an evolution of the magnetization as function of the temperature less sharp, the curvature is less marked and as consequence the saturation value of the magnetization is lower respect the reference sample. This different behaviour is clearly visible in the M(T) curves (Fig. 3.19), where a large curvature, and a different slope in proximity of the transition temperature differentiate the sample before annealing (dashed lines) and the reference(pointed lines). The shape of the curve is more stretched in case of irradiation with massive Ar and Kr ((d) and (e)) and less the opposite case, He and O ((a) and (b)).

The idea to restore the magnetic behaviour of the material by annealing process comes from two observations. First of all similar observations in studies on ferromagnetic thin films irradiated with charged ions ([80], [81], [58]). They assume that the decreasing of the magnetization at fixed temperature can be caused by amorphisation or structural phase changes of the material. Considering the same behaviour we try to restore the correct dependency by partially recovering of the defects of the crystal lattice. Secondly the irradiation in the annealing performed at 400K could induce the formation of γ-phases in the material. In fact this temperature is also the temperature where MnAs has a second order transition between the β-paramagnetic-orthorombic phase and γ-paramagnetic-hexagonal phase [82].

In figure 3.19 are displayed the results before and after the thermal treatment of the relative magnetization as function of the temperature. The samples are ordered from the lighter (H) to the heavier (Kr) ion beams used in the irradiation. Some comments can be done on the visible modifications of the material:

- The first important evidence is that in each case the hysteresis is kept suppressed. This means that the defects responsible for it are enough robust and cannot be easily recovered Fig. 3.19 (a)-(d).

- Samples irradiated with light ions, such as He, O or Ne-ions, display dependency of the magnetization on temperature more similar to the reference sample, and the slope of the curve is partially recovered. Fig. 3.19(a), (b) and (c).

- The annealing treatments seem not to be efficient for materials subjected to heavy ions such as Ar and Kr. The behaviour of the magnetization stay really different from the reference and it is well evident by looking at the relative magnetization at limits of high or low temperature. Fig. 3.19 (d) and (e).
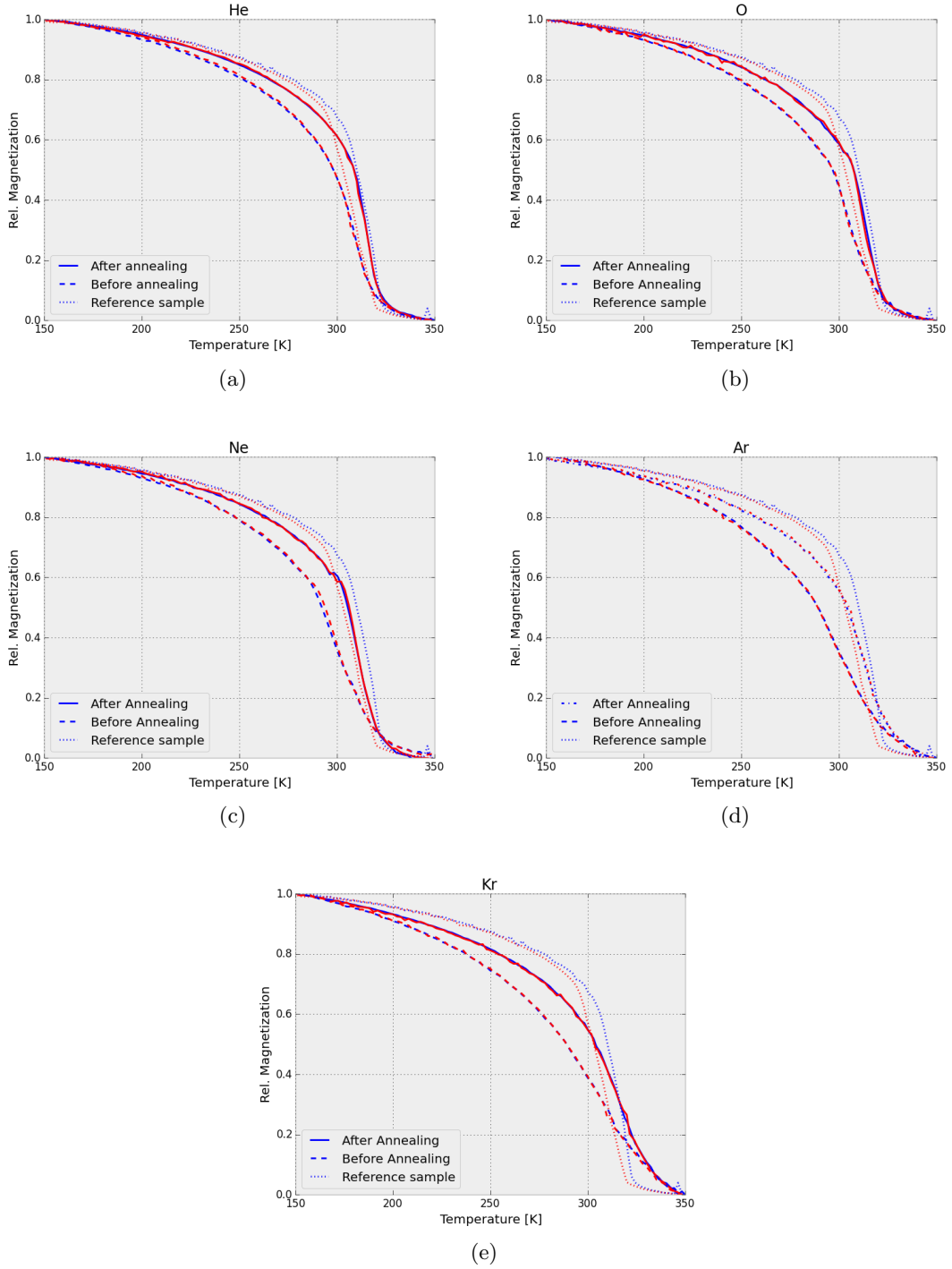
Figure 3.19: Relative magnetization the samples irradiated by different types of ions (H, O, Ne, Ar, Kr) before (dash-dot lines) and after the annealing (dashed lines) treatment. The reference sample is displayed by continuous line, while the temperature correction is represented by point lines.

66

The annealing process acts on these three cases of lattice disorder recovering some defects due to implantation, interstitial atoms and vacancies, this can lead to a partial restore of the magnetization. Past structural analysis at XRD demonstrated that defects, generated by Ne-ions bombardment, are certainly repaired after the annealing process [42]. However in our case, when the material is subjected to irradiation of ions excessively massive its lattice is strongly compromised and the defects generated are too much strong and complex to be cured.

In order to a study the process from a quantitative point of view we can consider to study the relative magnetization at fixed temperature. In figure 3.20 we show of the relative magnetization at temperature equal to 250K as function of the mass of the impinging ions. A complete recovery is never reached but as we had already hypothesized a partial recovery is higher for samples irradiated with of light ions.
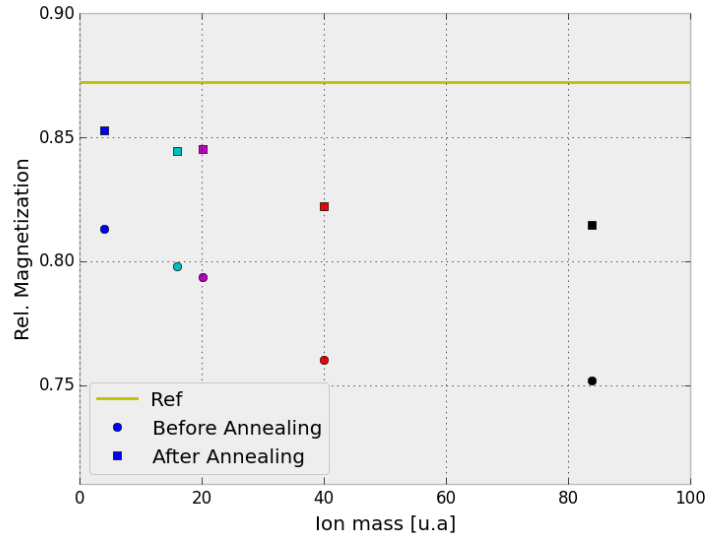

Figure 3.20: Measurements at 250K of the relative magnetization of the samples irradiated by different types of ions (H, O, Ne, Ar, Kr) as the mass of the impinging ions.

3.5   Summary of the results

Corrections on temperature and area considerably improve the quality of the data and help for the comprehensions of the magnetic modifications induced by ion irradiation. The correct value of the area of the sample ensures a more precise quantification of the saturation value of the magnetization and on the other hand this means a more clear idea on the magnetic power of the material. The correction in temperature allowed us to correctly determine the area of hysteresis after the irradiation and at the same time to neglect the presence of unnatural reverse hysteresis. As was already demonstrated irradiation of MnAs thin films leads to the suppression of the hysteresis, by creating defects that facilitate the first order transition. In this process many parameters influence the final results.

- **Fluence**: higher fluence of impinging ions can lead to a faster suppression of the hysteresis, but our results demonstrate that for values higher than the material result to be strongly compromised, reducing the magnetic power of the material. In this case an annealing treatment can be required

- **Type of ions**: for an equal value of fluence, massive ions can guarantee a more efficient reduction of the hysteresis, on the other hand as in the previous case they can cause robust damages (especially if associated to high fluence), that cannot be recovered through annealing process.

- **Collision density**: this is the key parameter that ensures to have a proper control of the hysteresis suppression mechanism. Its value can be evaluated using simulations such as SRIM as follows:
$$D_{colls} = \frac{N_{colls} * Fluence}{t_{film}}$$

  where N_{colls} is the average value of collisions per ion and t_{film} is the thickness of the sample.

- **Density of ions implanted**: differently from what was suspected at the beginning, new measures demonstrated that this parameter has no influence in the final result.

These results demonstrate that the high level of knowledge acquired in the comprehension of the process of suppression of the hysteresis. However a further improvement should be an investigation from a deeper point of view of the phenomena, in fact still missing a good investigation of the inner mechanism of interaction and of defects caused by the irradiation. A first attempt is the analysis of the stability of the defects presented here. This study on one hand points out the robustness of the damages induced by the collisions of ions, but on the other shows that a more deep investigation is required in order to explain the different behaviour of sample irradiated by heavy and light particles.

Future perspectives, following the idea of some preliminary studies at magnetic force microscope [83], will deal with the characterization of induced defects by Raman spectroscopy. In parallel a future target will be the development of more complete numerical simulations able to take into account at the same time the molecular dynamics with nuclear and electronic stopping power.

Chapter 4

Modification of MnFePSi-powders properties

In this chapter we develop an investigation on a new giant magnetocaloric material. The samples taken into account are powders characterized by a composition of MnFePSi. Even if the material seems a good candidate for the magnetic refrigeration, its properties results difficult to manage. The main topic of this chapter is the presentation of the procedure for the modification and study of the magnetic properties of the material. The initial part deals with the description of the phase-transition of the compound and the presentation of the general context in which the research is set. Starting from 10 µm considerations about obstacles on the irradiation procedure and sample preparation new methods will be developed. The results obtained are resumed in the conclusion, open to many possible future outcomes.

4.1   Introduction

The MnAs-compounds were considered promising materials for magnetic refrigeration. The first studies concerned the MnFePAs. This compound had the advantage of a small hysteresis, well tunable by P/As ratio, and the disadvantage of containing a well known toxic material. Due to possible environmental problems, a lot of efforts were spent to substitute the As with Ge. However even this latter resulted to be inefficient, because of limited availability and its nature too much influenced by the composition. A good compromise is found through MnFePSi. In fact, the tunability of the transition temperature is ensured acting on the Si concentration, and on the other hand, the material is neither toxic or expensive. The only disadvantage results to be the area of the hysteresis larger than the previous cases. The development of new methods for tuning the material properties became essential to optimize the material characteristics [84].

4.1.1   Analysis of the magneto-structural transition

The MnFePSi compound is a magnetocaloric alloy characterized by a first order transition. At low temperature the material is in paramagnetic state, as the temperature is increased up to a critical point, the ferromagnetic state is obtained. The magnetic behaviour can be demonstrated presenting the curve of the magnetization as function of the temperature Figure 4.1 (a). The material properties results to be influenced by its native characteristics such as composition and chemical order, and at the same time, they are affected by extrinsic aspects like structural disorder and strain in bulk [85].
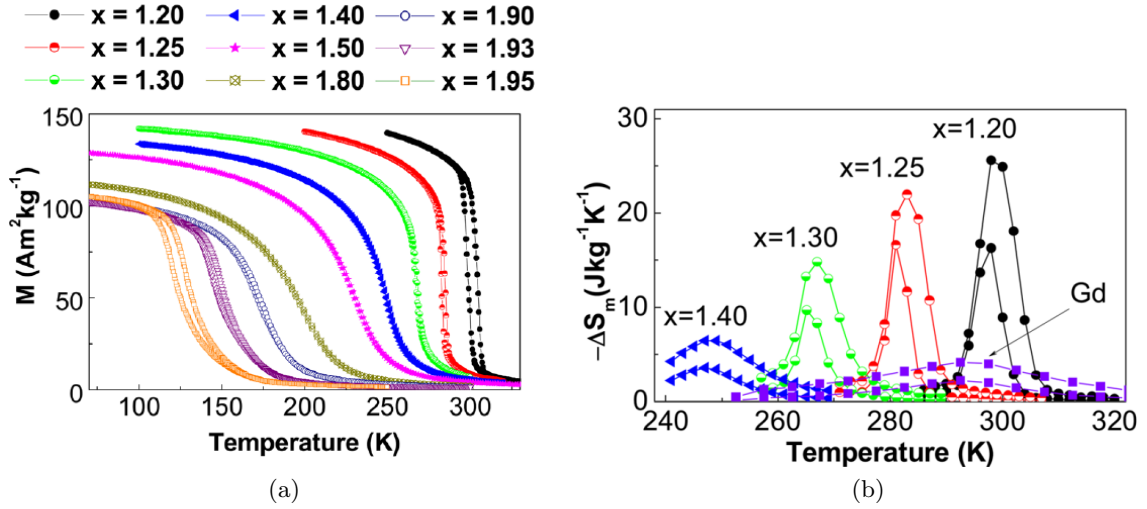

(a)   (b)

Figure 4.1: $Mn_xFe_{1.95-x}P_{0.5}Si_{0.5}$ magnetization dependence on temperature measured at magnetic field equal to 1T (a). Magnetic entropy change as function of the temperature measured at magnetic field varying 0-1T (lower curves) 0-2T (upper curves). The Gd magnetic entropy variation displayed for additional comparisons [86].

In Figure 4.1 (a) we can see that the material is at low temperature ferromagnetic and the magnetization reaches its maximum value. As the temperature is increased up to the critical point the paramagnetic phase is reached and the magnetization becomes abruptly null. The different composition of the material can be used to tune the temperature range at which the transition takes place. The thermal hysteresis is well visible and it confirms the first order nature of the transition. The great magnetization change causes a great variation of the magnetic entropy visible in Figure 4.1 (b). In this last picture, we can note that the ratio between iron and manganese allows the modulation of the thermal hysteresis. The absolute value of the magnetic entropy change is lower in material containing higher amount of Mn, but even in condition in which the thermal hysteresis is small the entropy change is larger respect reference materials such as Gd. For example in Figure 4.1 the ΔS relative to $x = 1.3$ (green curve in Fig. 4.1) is still four times higher respect the Gd-case (violet curve in Fig. 4.1 (b)) [86].

Similarly to the MnAs, MnFePSi alloy is characterized by a first-order magnetic transition associated with changes in the crystal lattice, that causes an increment of the magnetocaloric effect. The main difference between the thin film previously studied and the new sample is in the mechanism by which the structural configuration varies. We remember that in the MnAs the entire structure changes from an hexagonal phase into an orthorombic one by increasing the temperature. Differently the MnFePSi keeps the same hexagonal crystal structure both at low and high temperature, but the lattice constants suddenly change at the magnetic transition. The transitions typical of materials such as MnFePSi compounds are defined as first order magneto-elastic transition.
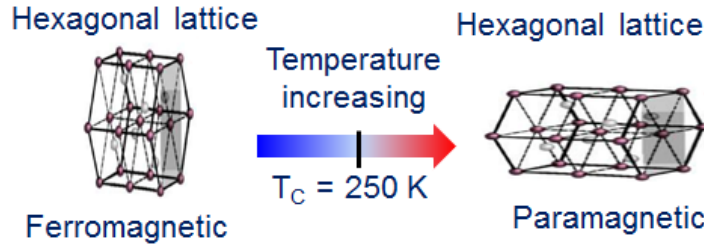
Figure 4.2: Scheme resuming the magneto-structural transition of MnFePSi compound before and after the critical temperature $T_c = 250K$.

Figure 4.2 resumes the effect of the transition on the material, if the material is at low temperature the structure results to be vertically shirked while the increment of temperature causes an horizontal elongation. Studies about the variation of the lattice constants of the material performed by XRD [87] confirm the stability of the hexagonal configuration and demonstrate that the lattice constant a and c change in opposite sense Figure 4.3.

Figure 4.3: MnFePSi lattice parameters behavior at temperature variation [87].

4.2   Context

In the last few years many attempts were made to tune the material properties and raise its performance. Most of the attempts concern the increase of both the mechanical stabil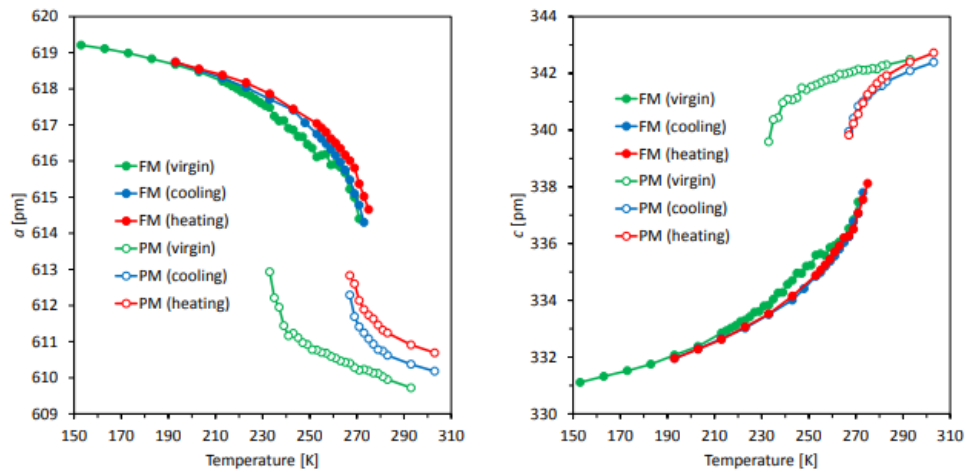ity and the magnetic properties of the system by doping or inducing stress/strain. In our case we will try to reduce the hysteresis following almost the same path used for the well-known MnAs thin films. We will induce damages through accelerated ion-beams and these will act as nucleation sites for the reduction of the hysteresis.

This section presents the context in which a new method for the treatment of the material is developed. The aim is to describe how the research on modification of MnFePSi powders started and which were the resulting problems that required a solution.

4.2.1   Sample preparation

The powders we are going to analyse are polycrystalline of $Mn_{1.3}Fe_{0.65}P_{0.5}Si_{0.5}$. The specimens are prepared by highly-energy ball milling under Ar atmosphere. The composition is properly chosen from high purity Fe_2P powders and P, Mn, Si chips in order to ensure the transition temperature near room temperature. The use of off-stechiometric compounds of $(MnFe)_{1.95}(P,Si)$ instead of $(MnFe)_2(PSi)$ is a way to obtain a sharp first order transition (Article [85]). The components grinding balls and starting material are mixed and pre-milled in grinding bowl put in rotation. After the polycrystalline sample undergoes to two cycle of annealing in Ar atmosphere. At this point the powders are pressed in Ar atmosphere and then sealed in quartz ampoules in 200hPa Ar atmosphere, before being annealed again. The material is then milled and filter in size, just particles below $10\mu m$ will be taken into account in this report.

Sometimes a further size selection can be necessary, the following method allows the separation of particles taken as limit the 2 μm length. The powders, collected in a test tube of solution of methyl alcohol, are put in an ultrasonic bath (frequency > 20kHz). The ultrasonication agitates the particles and part of them are induced in suspension. In particular due to their dimension the heavier particles ($2 > \mu$m) quickly decade, while the smaller ones ($< 2 \mu$m) remain suspended in the solution. Powders according to the necessary size are withdrawn for the sample preparation. It is important to precise that even if they are selected in size, the particles are characterized by different shapes (Figure 4.4) that can influence the irradiation or the successive measurements.

To have the possibility to analyse the structure of the material before and after, the irradiation and to move the sample from one instrument to the other, a secondary treatment of immobilization of the particles on substrate is necessary. The method has to ensure the creation of a fixed monolayer of MnFePSi compound. This process is one of the main problems in the treatment of the material, first of all, because the creation of a homogeneous single layer is complicated, secondly, the substrate does not have to interfere with their magnetic response of the material during the measurements at constant temperature or magnetic field.

The initial method adopted consisted in pasting the powder on a kapton tape. This

procedure was not satisfying for the following two reason: first of all the packaging resulted to be not enough solid and manipulations during the move from one instrumentation to the other caused the deteriorating of the sample itself, secondly the tape was partially cooked after irradiation at high energy, causing the possible contamination of the experimental environment.
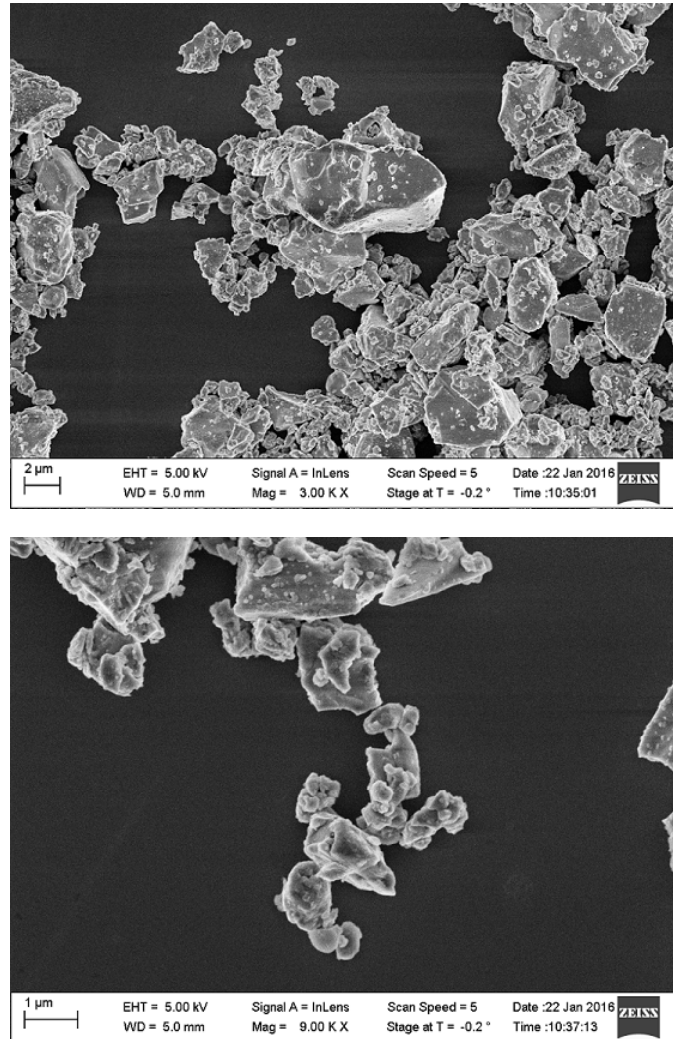

Figure 4.4: Pictures of MnFePSi-powders captured by transmission electron microscope (TEM) display the different shapes of the particles.

4.2.2 Irradiation

The first attempt to modify the magnetic properties of MnFePSi alloy was at the electron-cyclotron ion source at SIMPA facility in our laboratories. The sample studied was prepared as described in the previous section by selecting the particles 2 μm long and then subjected to Ne ions beams accelerated at 135 keV. For simplicity we will call this sample Sample 4

The previous analysis of MnAs-thin films demonstrated that the main mechanisms that guarantee the suppression of the hysteresis are the nuclear collisions between impinging ions and the target atoms. From this assumption, we want to obtain the most uniform irradiation of sample as possible, and penetrate the entire thickness of the material. However, in the initial stage of the research it was believed that the suppression of the hysteresis was mainly due to the density of implanted ions. Consequence of this misunderstood idea as is shown in Figure 4.5 (a) the energy of the impinging ions was not enough to guarantee the creation of homogeneous damages, just the 15% of the thickness of the material was irradiated (300nm over 2 μm).
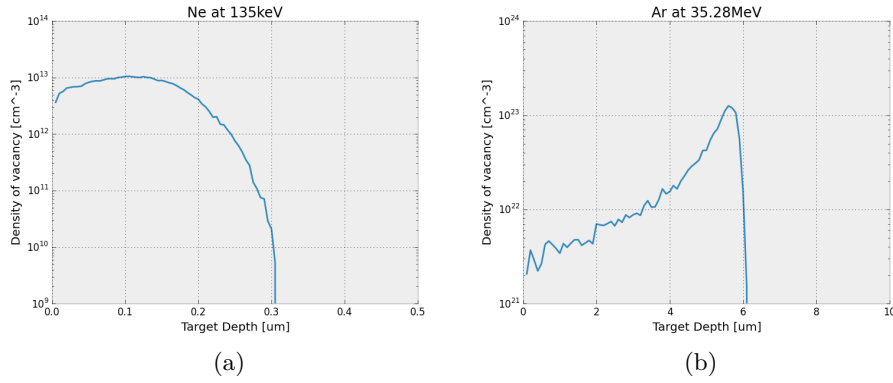

(a) (b)

Figure 4.5: (a) Numerical simulation of SRIM program displays the penetration depth of MnFePSi-powders subjected to irradiation by Ne-ions at 135keV. (b) Numerical simulation of SRIM program displays the penetration depth of MnFePSi-powders subjected to irradiation by Ar-ions at 35MeV.

In order to increase the penetration depth, a new irradiation section was performed at GANIL facility. Similarly to the MnAs thin films, the sample at the IRRSUD beam line was irradiated at high energy (35MeV) by ^{36}Ar-ion, this sample will be called Sample 7 . In this case the sample used for the bombardment was prepared by selecting the larger dimension of the particles (10 μm).
As displayed in Figure 4.5 (b) the penetration depth was increased up to 6 μm but on the other hand, the powders were thicker (no ultrasound selection).

Even if no homogeneous irradiation of the sample was performed, a reduction of the hysteresis was visible for both the two cases, as reported in the measurement of the magnetization as function of the temperature by SQUID magnetometer in Figure 4.6.

74

(a)   (b)
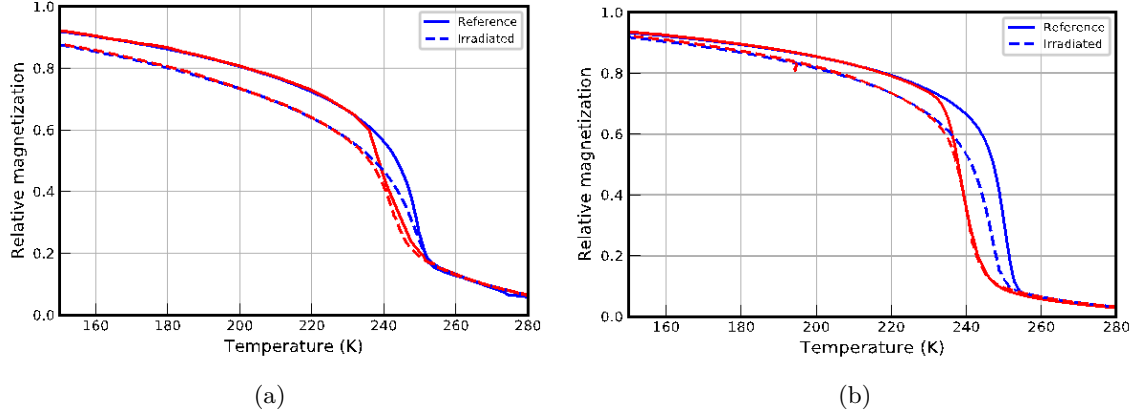
Figure 4.6: Relative magnetization as function of the temperature measured by SQUID magnetometer at fixed magnetic field equal to 1T. Image (a) displays the behaviour of the sample before and after being irradiated by Ne ions. Image (b) shows the response of the sample before and after the irradiation by Ar ions. The blue and red curves represent respectively the heating and cooling condition.

4.2.3   VSM measurements and phase diagram

The magnetic momentum can be measured as function of the magnetic field through VSM magnetometer, in our case the remeasure of the magnetic properties of Sample was necessary for the extrapolation of the phase diagram of the material.

Figure 4.7: Sample 7 magnetic momentum vs magnetic field at five different temperature measured at VSM before (dashed lines) and after (continuous lines) the irradiation. The red points represent the critical field calculated

In Figure 4.7 is shown the magnetic measurement performed at VSM. The magnetic

75

momentum was studied in isothermal condition for five different temperature and for cycle the critical field was studied twice (one for the cooling curves).
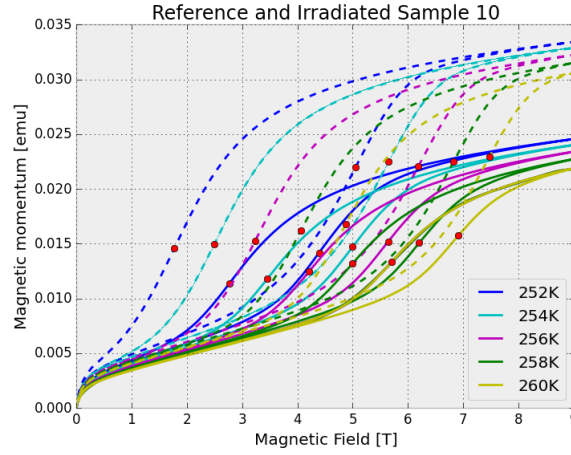
Each curve of the diagram was first of all fit by one-dimensional smoothing spline fit of 5 degree. The result of the fit was used to calculate the second order derivative and the respectively zero-points. It can be demonstrated that the critical field is equal to the flexural point, in other words the field at which the second order derivative of the magnetic momentum curve results null. In Figure 4.7 the critical field is marked with red points.

The data obtained in this way are used to build the phase diagram (critical magnetic field versus temperature) displayed in Figure 4.8. The phase diagram, as we have already explained in chapter 1, is used to predict the behaviour of the material when the parameters associated to its phase transition are changing. In our case (Figure 4.8) the material is paramagnetic at high temperature but low field (under the red curve), while over the blue curve (high field, low temperature) is ferromagnetic. The area between the straight lines defines the hysteresis, metastable situation in which the two phases coexist. If we compare the area between the dashed lines, representing the reference sample, with one between the continuous lines, representing the sample irradiated, is well visible the reduction of the hysteresis caused by the bombardment.
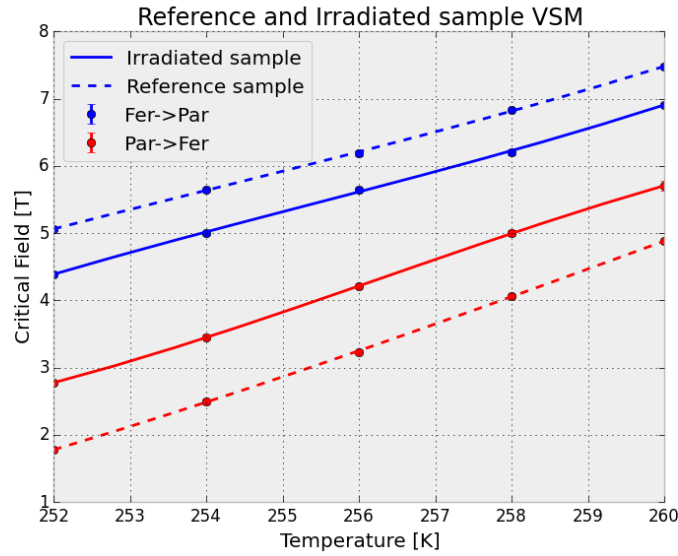

Figure 4.8: Phase diagram of the MnFePSi-sample7 before (dashed lines) and after (continuous lines) the irradiation. In red and blue are represent respectively the cooling and heating curves.
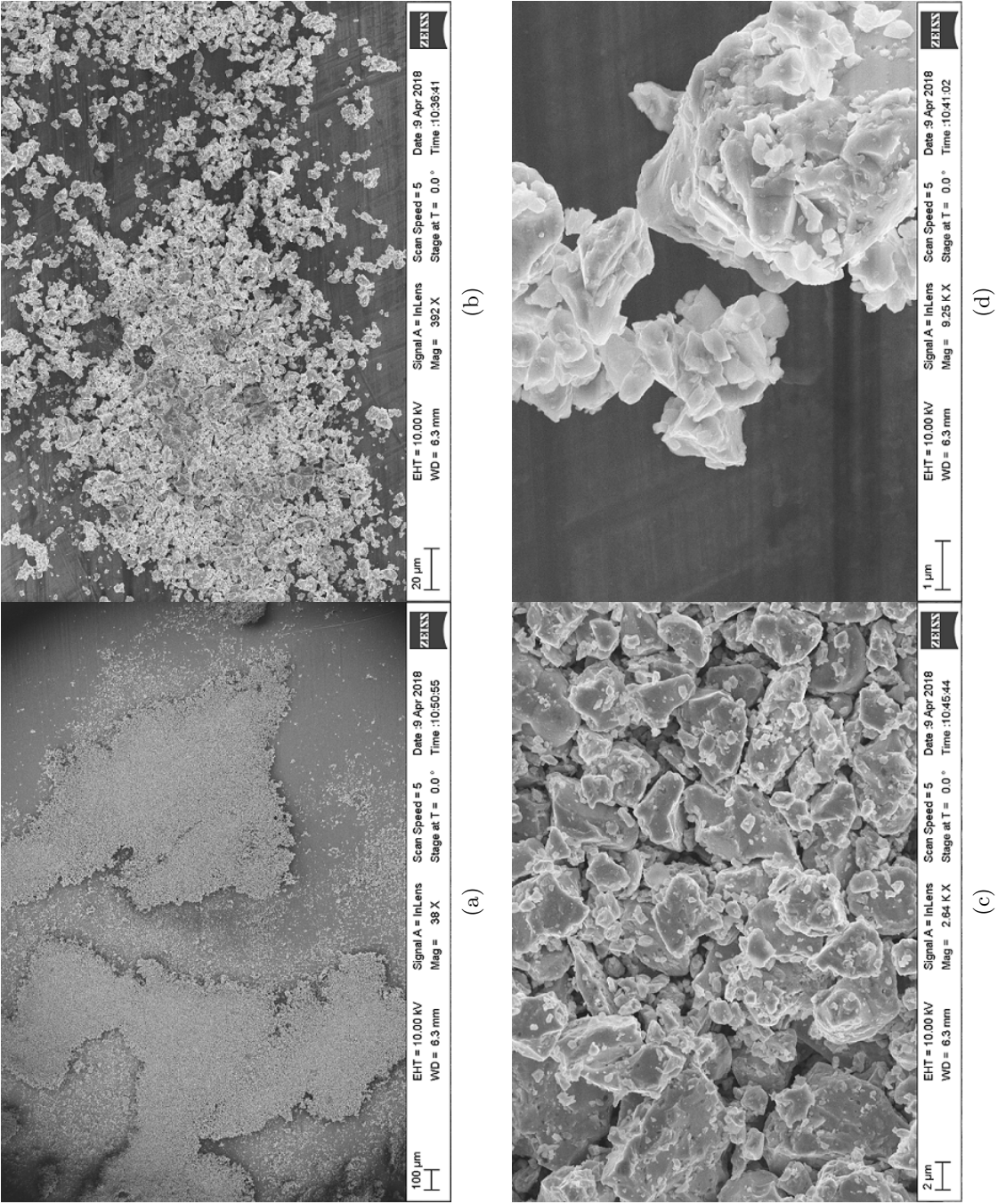
Figure 4.9: Pictures taken by transmission electron microscope (TEM) of the MnFePSi deposited on aluminium substrate

4.3 New method of sample preparation and irradiation

The results obtained by the irradiation at low and high energy demonstrated that the suppression of the hysteresis in MnFePSi-powder was possible, on the other hands they underline the relevance of problems that had to be solved. The material considered was more difficult to manage respect the MnAs thin film because of its nature.

- The particles were difficult to immobilize on a single layer (Figure 4.9) and as consequence the description of the material in morphology and volume were impossible or inaccurate.

- The material resulted really thick even when the size selected is below 2 μm as consequence the uniform irradiation of the sample resulted impossible.

- The kapton tape substrate was not efficient neither to carry the material or to support the irradiations and measurements.

Consequence of all these considerations this chapter will present a new method developed in order to optimize the sample preparation and irradiation of the material.

4.3.1 Sample preparations

Taken as inspiration the preparation of the sample in Article [88] we can think to encase a thin layer of powders on a substrate. The substrate has to be properly chosen by verifying that the thickness of the sample is much less than the range of ions, so that the ion passage through the entire material is dominated by electronic loss. For example aluminium in Figure 4.10 seems a good option. In addiction the metal will not interfere with the magnetic measurements and being a good conductor avoids the charge accumulation that could interfere with the irradiation.
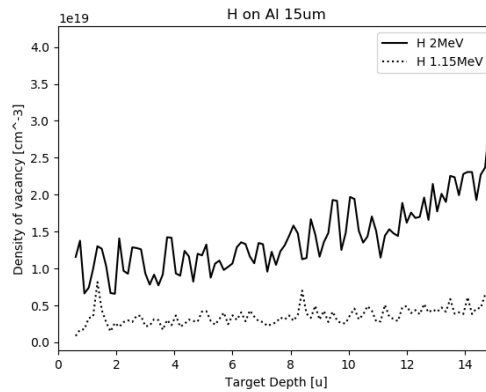

Figure 4.10: Study of the penetration depth of the Al substrate irradiated by protons using SRIM. The study was performed under the condition of H-ions bombardment because, as we will see in the following section, the simulations predict this beam as the most adapted for damages generation.

78

In order to avoid the coagulation and to ensure a good uniformity in the deposition, the MnFePSi-powders are prepared in a solution of methyl alcohol and the particles are subjected to ultrasonic bath to be selected in size.

To ensure the collimation of the particles a kapton-mask is created over the aluminium layer, eventually fixed on silicon chip just for support. A thick layer of kapton tape defines the area where the particles will be deposited as shown in Figure 4.11(a). Few drops of material, withdrawn from the solution, are let them fall on the aluminium lamina. When the drop is completely dried, the particles are encased in the substrate by pressing them through a glass lamina resulting in Figure 4.11 (b). In order to guarantee the possibility of moving the sample from one instrument to the other different samples dimensions where tested, the final 2x4mm chips are displayed in Figure 4.11(c).

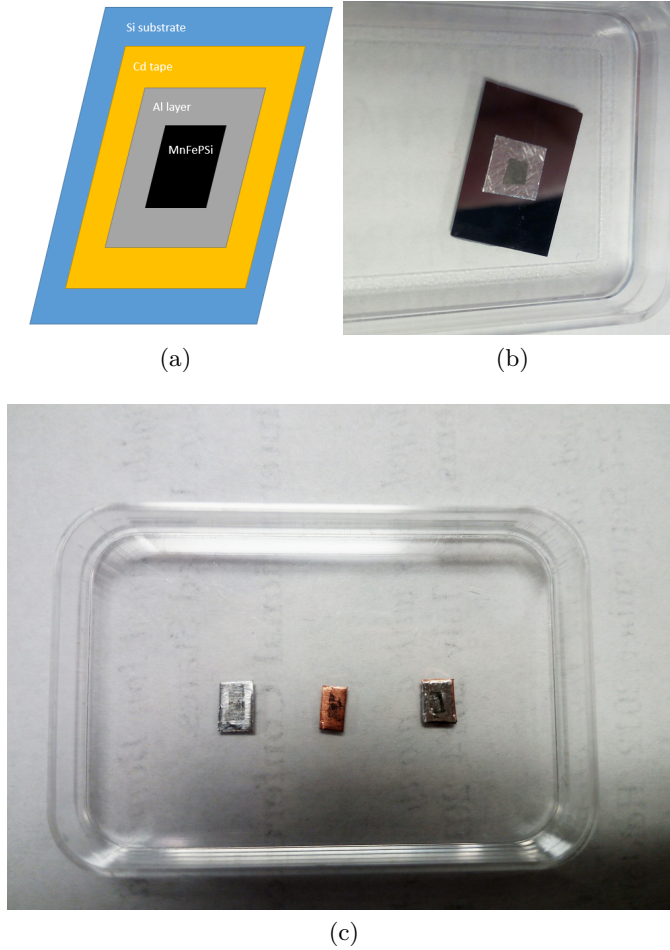(a)   (b)

(c)

Figure 4.11: (a) Scheme of the mask used for the sample preparation. (b) MnFePSi final sample wrong dimensions(c). Test of different samples 2mmx4mm, starting from left Al-substrate, Cu-substrate, Cu-Al-substrate.

4.3.2 Preparation for irradiation: SRIM simulations

The conditions for the irradiations of the MnFePSi target material have to be preliminarily studied by means of SRIM programs. The numerical simulations we are going to discuss come from the purpose of evaluating and comparing the collisional events caused by different ion-beams at different energies.

The simulation set up can be resumed as follows:

- The target is MnFePSi-compound with the following composition $Mn_{1.30}Fe_{0.65}P_{0.5}Si_{0.5}$ and density equal to $5.76g/cm^3$.

- Considering the possible size selection the calculations will be performed for both $2\mu m$ and $10\mu m$ of length.

- To obtain an uniform penetration of the sample the impinging particles will be accelerated at the maximum value 2MeV. This energy value is not arbitrary, on the contrary it is the maximum value achievable by SAFIR accelerator in our laboratory.

- As impinging particles will be used different types of ions: Ar, C, N, He, H and O

- The fluence used is initially set equal to 10^{15}ions/cm^2 for each type of ions, in a second moment it will be modified to obtain the desired amount of damages.

Sample			10μm	2μm
Ions	Energy [MeV]	Fluency [ions/cm^2]	Density of vacancies [ions/cm^3]	Density of vacancies [ions/cm^3]
Ar	35.28	10^{15}	$1.38 * 10^{22}$	$4.04 * 10^{21}$
C	2	10^{15}	$1.59 * 10^{21}$	$7.91 * 10^{21}$
N	2	10^{15}	$2.02 * 10^{21}$	$1.01 * 10^{22}$
O	2	10^{15}	$2.68 * 10^{21}$	$1.34 * 10^{22}$
He	2	10^{15}	$2.44 * 10^{20}$	$1.12 * 10^{20}$
H	1.15	10^{15}	$2.27 * 10^{19}$	//
H	0.35	10^{15}	//	$8.86 * 10^{19}$

Table 4.1: Table resuming the input condition for the simulation with sample 10 μm and 2 μm longs, and the output density of vacancy obtained.

Figure 4.12 (a) and (b) shows the density of vacancy generated as function of the thickness of the sample, respectively for $10\mu m$ and $2\mu m$ of length. The majority of the particles are not able to penetrate completely the sample 10 μm longs. On the contrary, protons are able to cross completely the material and ensure the generation of uniform damages. In addition, it looks like that proton-beam requires a lower energy respect the other ions.
The interactions between H ions and powders have been studied at different energy as shown in Figure 4.13. The comparison among different acceleration allows us to choose the best condition for the irradiation. The optimum situation ensures an uniform and complete penetration of the material and a density of vacancy peaked just after the length of the

sample desired. 2 MeV results to be an energy too much elevated for the beam, on the other hand lower values allow the generation of an higher amount of damages. To conclude a proper value of acceleration can be chosen: 1.1 5MeV for the 10 μm sample and 350MeV for the 2 μm one Table 4.1.
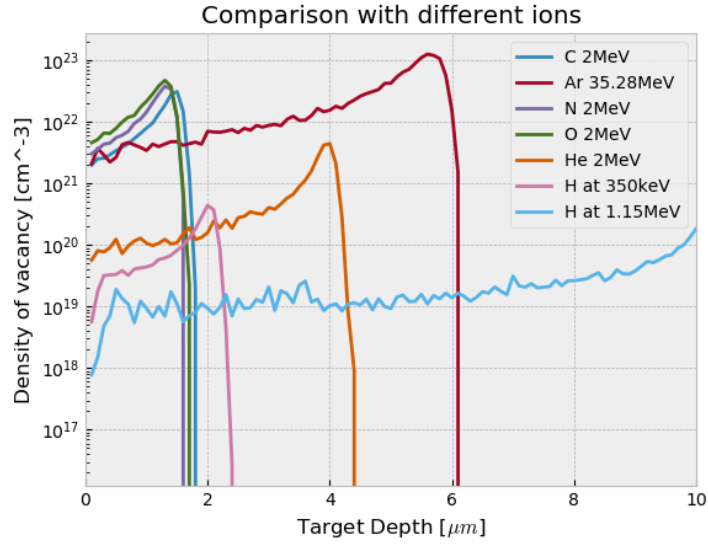
(a)
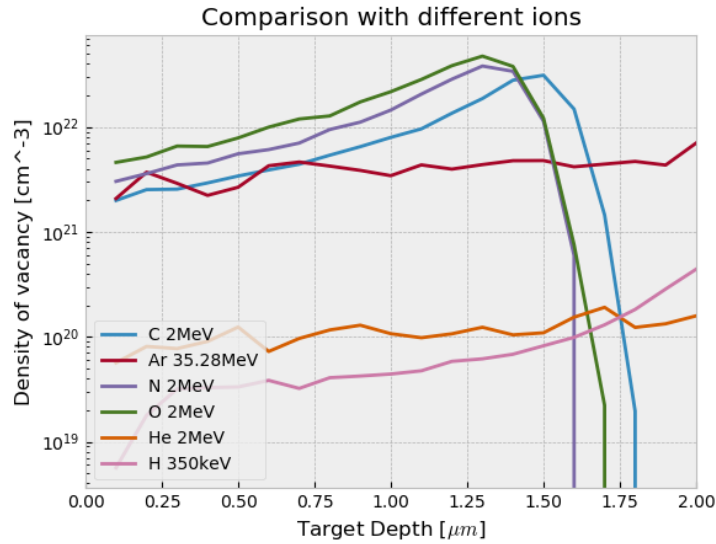
(b)

Figure 4.12: Plot on semi-logarithmic scale of the density of vacancy generated by different impinging ions properly accelerated. (a) Displays the entire 10μm length of the sample, (b) is a focus on 2μm length.
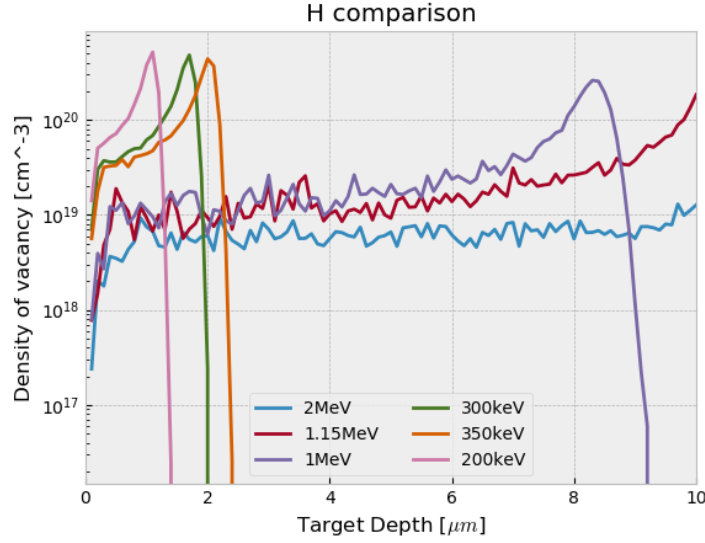
Figure 4.13: Comparison among density of vacancy caused by proton-beams acelerated at different energies in MnFePSi target.

The Ar-ions beam, displayed in red in Figure 4.12, is used as reference, this means that our aim is to generate the same amount of defects. The fluence condition is one order of magnitude higher respect the Ar irradiation presented in the previous part, this choice is justified by the new set-up of SAFIR. Differently from SIMPA, it allows the possibility of higher amount of impinging particles.
From the datas of the table 4.1 is possible to calculate the average amount of defects created through Ar bombardment characterized by a fluence $\Phi = 10^{15}$ions/cm^2,

$$\texttt{density of vacancy = number of defects* fluence}$$

Reversing the previous formula we can calculate the fluence necessary with different types of ions to obtain the same amount of damages. The results computed in this way are resumed in the first columns of Figure 4.14 (a) and (b).

As anticipated, in order to obtain an uniform irradiation of the sample at high energy is required the use of an accelerator. For this purpose in our laboratory is available SAFIR that enable us to obtain energy up to 2MeV with light particles such as protons and He-ions. To validate the simulation done is to demonstrate that the process is feasible through the instrumentation available.

Considering a standard process SAFIR exploits a spot of 2mm^2 large at 500nA, providing an average fluence of $1.50 * 10^{14}$ions/cm^2. It is possible to calculate the time required by the accelerator to obtain the fluence of ions necessary to characterize the sample:

$$Time \ = \ \frac{fluence_{SRIM} * e * A_{spot}}{i}$$

$fluence_{SRIM}$ is the fluence required by SRIM simulation
e is the electron charge
A_{spot} is the area in cm^2 of the SAFIR spot, in general equal to $200 cm^2$
i is the current used in the irradiation, standard value of $500 nA$.

Using the standard parameters of the spot and average fluence the times required in each case are displayed in the last columns of Figure 4.14. Again the protons seems to be the best choice for the irradiation. Considering samples 10μm long, if the calculations are correct, by H-ions we should provide the same amount of damages created at high energy with Ar, and the time necessary is more or less an hour.

10um				
	SRIM fluence	**SAFIR fluence**	**Time required**	
	[ions/(cm^{2}s)]	[ions/(cm^{2}s)]	[s]	[min]
H(1.15MeV)	6,05E+17	1,50E+14	4,03E+03	6,72E+01
C (2MeV)	8,69E+15	1,50E+14	5,79E+01	9,65E-01
N (2MeV)	6,81E+15	1,50E+14	4,54E+01	7,57E-01
O (2MeV)	5,12E+15	1,50E+14	3,41E+01	5,69E-01
He (2MeV)	5,62E+16	1,50E+14	3,75E+02	6,25E+00

2um				
	SRIM fluence	**SAFIR fluence**	**Time required**	
	[ions/(cm^{2}s)]	[ions/(cm^{2}s)]	[s]	[min]
H (350KeV)	4,56E+16	1,50E+14	3,04E+02	5,06E+00
C (2MeV)	5,10E+14	1,50E+14	3,40E+00	5,67E-02
N (2MeV)	4,00E+14	1,50E+14	2,67E+00	4,45E-02
O (2MeV)	3,01E+14	1,50E+14	2,01E+00	3,34E-02
He (2MeV)	3,59E+16	1,50E+14	2,39E+02	3,99E+00

Figure 4.14: Table resuming the conditions of fluence and time necessary to obtain the same amount of damages obtained through Ar-ions accelerated at 35MeV. (a) Displays the results for samples 10μm long. (b) Displays the results for samples 2μm long.

4.3.3   Medium-energy irradiation and induced modifications

The SAFIR accelerator can provide monocharged beams of ions H+, He+ in an energetic range from 100keV to 2MeV. In the following part we will analyse three different samples, named respectively sample 11, 12 and 13, irradiated at different conditions of type of impinging particles and energy.

H-ions irradiation

The sample 11 was properly prepared through size selection of 10μm on Al-substrate. It was subjected to protons irradiation at $E = 1.2$MeV, by a spot of 2mm^2 and the current equal to 1μA. The entire process lasts for one hour and half.

The magnetic properties of the material were studied before and after the irradiation by exploiting the SQUID magnetometer. The procedure for the measurement of the powders is the following. If the sample is virgin, never subjected at low temperature condition, the material is first heated at 350K before the field calibration. This process allows to record the *Virgin effect*, a peculiar phenomenon consisting in a change of in the slope of the magnetization versus temperature curve and a lower transition temperature upon the first cooling. The virgin effect is visible as yellow curves in the Figure 4.15 when material is cooled down to 150K in a isofield condition. Leaving aside this fact, the magnetic momentum is performed varying the temperature from 350K to 10K and then back through a sweep rate of 2K/min.

In Figure 4.15 the magnetic momentum function of the temperature of the sample 11 is displayed before and after the irradiation. The reference sample shows, as yellow line, the virgin effect. This phenomenon was largely studied [85, 89]. In particular analysis performed by using Hall-Probe imaging revealed the presence of cracks after the first cooling and reported a phenomenological relation between particle size, dislocation density and the virgin effect [85]. Formations of cracks captured by light microscope, were observed at the transition temperature of the M(T) curve during the first cooling. Consequent of the damages was evidenced an increment of the magnetization and transition of portion of the sample into ferromagnetic phase. Further decrement of the temperature leaded to creation of additional cracks in avalanche process. The studies concluded that the ferromagnetic behaviour was exhibited just by the cracked part of the sample resulting in the change of the slope of the curve known as virgin effect.

Some modifications in the properties of the material can be pointed out comparing the sample before and after the irradiation in Figure 4.15

- The M(T) curve results to be a bit stretched after the irradiation, the curvature is increased Fig. 4.15 (a). Even if the protons are for sure the lightest ions, the same behaviour was observed in MnAs when subjected to heavy particles.

- The saturation value of the magnetic momentum at 10K is well different considering the two cases Fig. 4.15 (a). This results in a reduction of the magnetic power of the 8%. This can be due to a wrong calibration of the fluence at which the sample was subjected as seen in the MnAs case.

- Finally the hysteresis reduction is well visible in the normalized version of the magnetic momentum versus temperature Fig. 4.15 (b).

- The mass of the sample was measured before and after the irradiation. Being the difference of the order of 10^{-5} the sample can be considered unchanged from this point of view.
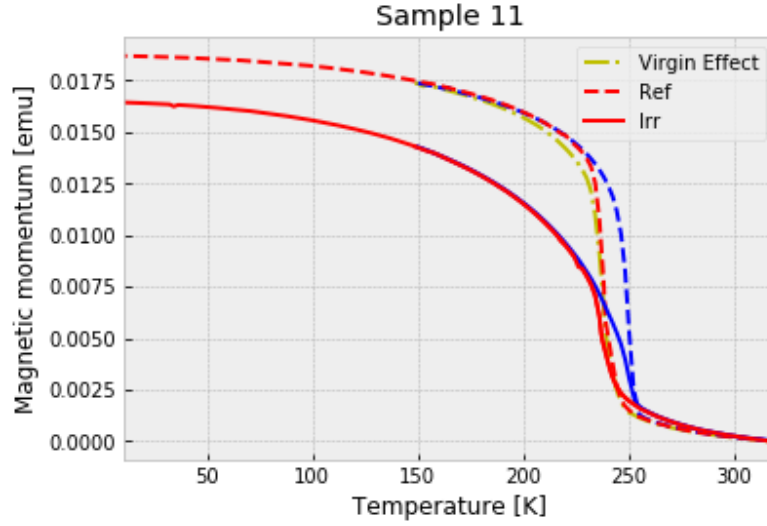
(a) Magnetic momentum versus temperature
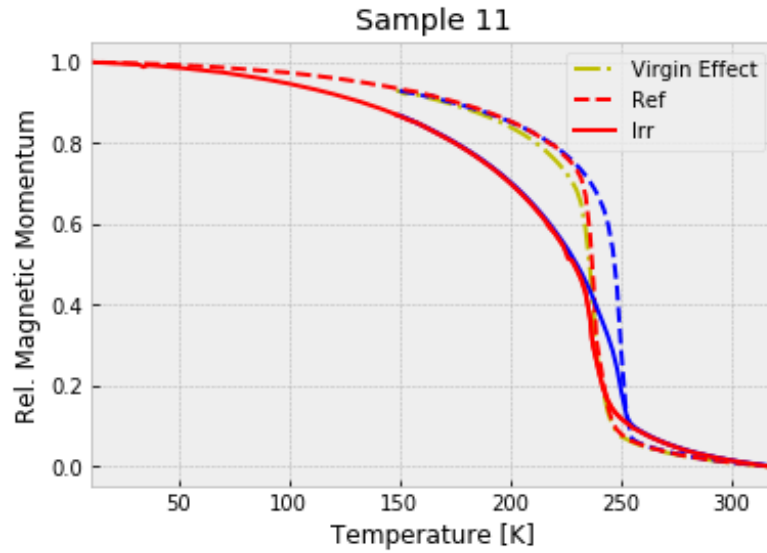
(b) Relative magnetic momentum versus temperature

Figure 4.15: In red and blues represent respectively the cooling and the heating curve, while in yellow is displayed the virgin effect. The sample is studied before (dashed-lines) and after (continuous line).

He-irradiation

The sample 12 and 13 are prepared considering the size selection under 2μm. They were both subjected to irradiation of He-ions accelerated at $1.8MeV$ with a spot of 2mm^2 at 850nA. The difference between the two cases consists in the exposure time: the sample 12 was irradiated for two minutes, while the sample 13 for four minutes.
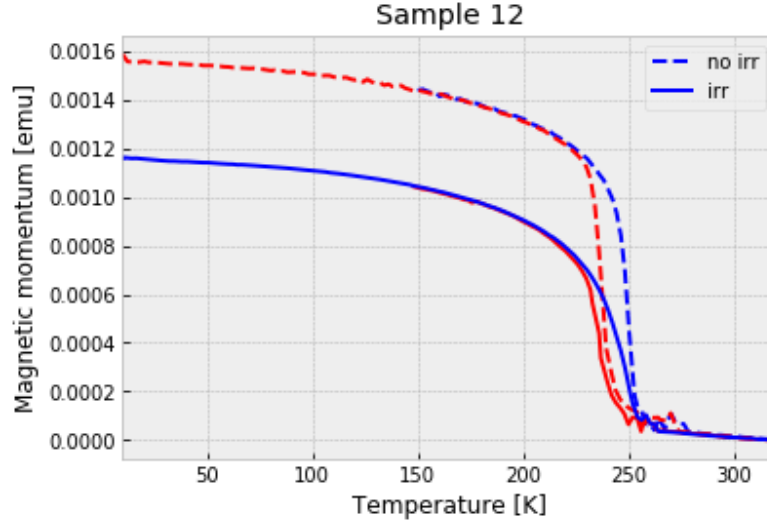
(a)

(b)

Figure 4.16: (a) Magnetic momentum versus temperature (b) Relative magnetic momentum versus temperature of the sample 12 irradiated for 2 minutes with He-ions. In red and blues represent respectively the cooling and the heating curve, while in yellow is displayed the virgin effect. The sample is studied before (dashed-lines) and after (continuous line).

86

(a) Magnetic momentum versus temperature

(b) Relative magnetic momentum versus temperature

Figure 4.17: (a) Magnetic momentum versus temperature (b) Relative magnetic momentum versus temperature of the sample 13 irradiated for 4 minutes wi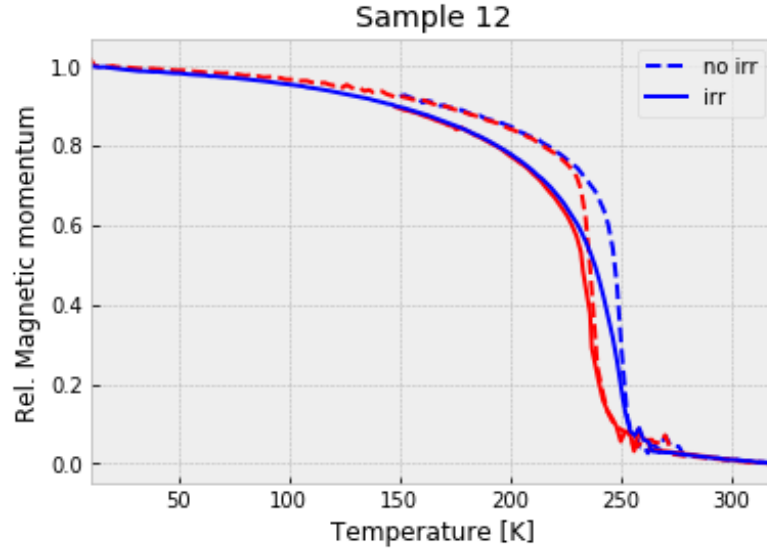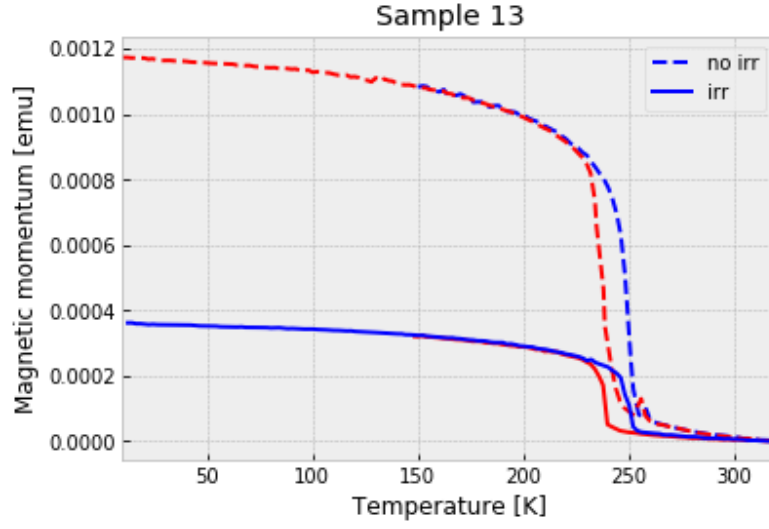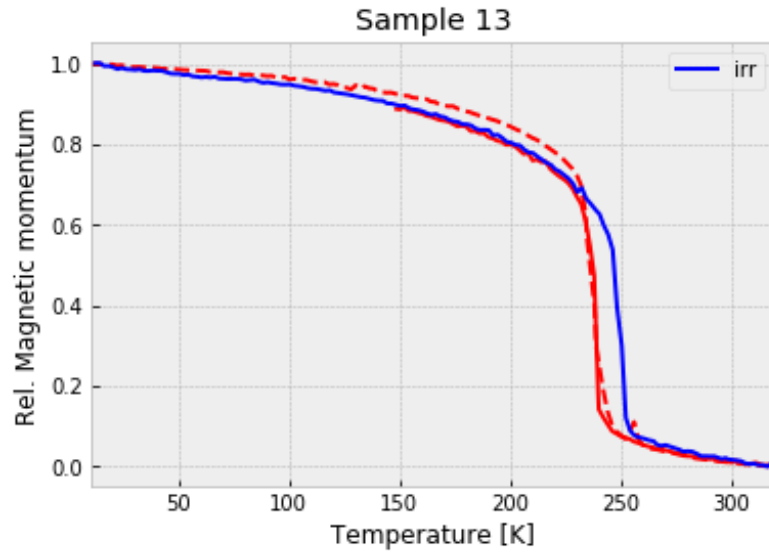th He-ions. In red and blues represent respectively the cooling and the heating curve, while in yellow is displayed the virgin effect. The sample is studied before (dashed-lines) and after (continuous line).

The results of the two types of irradiation are displayed in Figure 4.16 and 4.17. Considering the sample 12 Figure 4.16 (a) the curvature is increased in the irradiated sample respect the reference one. The saturation value of the magnetic momentum at 10K seems really deteriorated before and after the irradiation leading to a decrement of the 26% that will effect the magnetic power of the material. In addiction in Figure 4.16 (b) the hysteresis seems just lightly reduced by the bombardment.

If considered the sample 13 the situation results more dramatic. The material subjected at He-ions highly accelerated for a longer time displayed a reduction of the hysteresis almost null Figure 4.17 (b). Furthermore the magnetic power of the material is very degraded, in fact the saturation value of the magnetic momentum before and after the irradiation is decreased of the 69% (Figure 4.17 (a)).

Sample	Ions	Length [um]	Energy [keV]	Fluence [ion/cm2]	Exposure Time [s]	Density of damages [damages/cm^3]	Density of ions [ions/cm^3]	Suppression of the hysteresis
4	Ne	2	135	1,00E+15	1200	8,14E+21	4,97E+18	indefinible reduction
7	^{36}Ar	10	35000	1,00E+14	1200	1,38E+21	1,01E+33	possible reduction
11	H	10	1187	1,6875E+18	5400	2,93E+22	2,96E+19	indefinible reduction
12	He	2	1800	3,1875E+16	120	5,36E+21	3,17E+16	indefinible reduction
13	He	2	1800	6,375E+16	240	1,07E+22	6,33E+16	indefinible reduction

Figure 4.18: Resume of the condition of the irradiation of MnFePSi samples

The table above 4.18 resumes the conditions at which the samples were subjected for the irradiation and the successive results. By looking at the column of the density of the damages induced is evident that the excessive fluence in case of Ne, H and He bombardment cause distortion of the lattice that in a second time cause an deterioration of the magnetic power of the material. Under this condition, it is difficult to understand which one present a real reduction of the hysteresis or which is just stretched picture of the M(T) curve. Probably the He and H ions are too much light to ensure the creation of such defects responsible for the suppression of the hysteresis, on the other hand it is more probable that in the case of irradiation with Ar ions the hysteresis is reduced for real. In the Ar-irradiation the main obstacle was related to the dimension of the sample, a good option for the future will be to repeat the same experiment with the selection size of 2 μm for the sample preparation.

4.4   Results and perspectives

The MnFePSi-powders, as demonstrated in this chapter, are difficult to manage. Numerical simulations reveal that new possibilities for the modifications of the magnetic properties of the material can be achieved. The irradiation sections show us that it is necessary a deep control of each parameters involved, such as time, fluence, energy and types of beams. On the other hand a number more elevated of experiment should be processed, to clarify the better strategy to use. From the experiments performed the heavy ions seems the more efficient particles for reduce the hysteresis in MnFePSi-compound

Unexpected results, obtained before and after the bombardment, should encourage us in the investigations of the defects responsible for the suppression of the hysteresis, and the ones created with irradiation. In fact we must consider that, even if the SRIM results ensure a density of defect comparable with the one created with Ar-ions, the protons are much more lighter than argon ions. As consequence maybe they can create weak damages, that can be easily recovered by the crystal in a short time.

The new method for the sample preparation is a good compromise for the immobilization of the particles but on the other hand has to be optimized. Results obtained especially with small size powders (sample 12 and 13) can be influenced by the fact that the extraction of a good quantity of material from the solution result quite difficult, especially during the selection of the smaller particles.

All these assumptions lead as to the necessity of studies on the structural properties of the MnFePSi-compounds before attempting new irradiations sections. Xray or raman spectroscopy could represent new approaches in the characterization of the material.

Chapter 5

Conclusions and perspectives

The irradiation of a giant magnetocaloric material is a complex process that has proven to be an adequate technique for the suppression of the thermal hysteresis. In order to achieve a global comprehension of the mechanism of action, it is necessary to have good knowledge of the target material, ion beam, interaction mechanism and the of the resulted defects. In this context, this thesis is aimed at enhancing and deepening some aspects of the magnetic properties characterization process through the interaction between giant magnetocaloric materials and ions beams. Further purpose is the investigation on other giant magnetocaloric materials, like MnFePSi-powders, that, on one hand, are challenging to manage but on the other can be seen as optimum candidate to enter in the market of materials for magnetic refrigeration.

In the presented work a first challenging investigation is performed about the relations occurring between the temperature read by sensors and the real temperature of the sample during magnetic measurement at SQUID magnetometer. The observations prove incorrect temperature values in case of cooling of the material. In the report, it is provided a method for the extrapolation of a correction coefficient. For any sample, the magnetic properties that could be extracted from the study of the temperature dependency of the magnetization have been corrected. The results allow to neglect in a rigorous way the improbable presence of reverse hysteresis, a phenomenon not explained by means of reasonable scientific argumentations.

Starting the analysis of MnAs giant magnetocaloric, thin films more detailed aspects in the hysteresis reduction process are pointed out. The new quantification of the area of the hysteresis, extracted from the magnetization function of the temperature for sample irradiated at different conditions, permits to outline a regular trend between the area of the hysteresis and the density of collisions. Corrections in the areas of the samples resulted in a more precise evaluation of the saturation value of the magnetization, that means a precise quantification of the refrigerant power of the material. As confirmation of data already collected, the density of collisions is the main actor in the process of elimination of the hysteresis. The hysteresis area is reduced for increasing amount of collisions, then, at defined density, it saturates at null values. With the aim of investigating the stability of

the defects induced by ion bombardment, the MnAs samples have been subjected to thermal annealing. The process is able to restore the correct slope of the magnetization curve keeping the hysteresis suppressed, that means that the defects causing the elimination of the hysteresis are quite robust. The magnetocaloric material in most of the case is cured by thermal treatments, in hardest case, when the sample was subjected to irradiation of too massive beams the magnetic properties are compromised.

The problems in previous irradiation sections of MnFePSi giant magnetocaloric powders have been considered as basis for the new strategy adopted for both the sample preparation and bombardment. The new package of the powders by means of aluminium substrate prevented the contamination of the measurement when excessively heated and constitutes a solid support easy to move from the irradiation to the measurement set up. With the scope of establishing the same amount of damages obtained by means of heavy ions (Ar), we have irradiated samples through light ions (H and He). Even if the simulations of the interaction between ions and material were promising for the suppression of the hysteresis, the measurement of the magnetic properties of the material after the irradiation showed results difficult to understand for the moment. The saturation values of the magnetization are reduced as well as the slope of the curve, the hysteresis, on the other hand, is still evident. Problems can be related to the type of damages caused by the ions or problems in the irradiation sections. In the first case, it is possible that the defects generated are too much weak and they are easily restored by the crystal lattice. On the other case to test the validity of the method it is necessary to perform a larger number of irradiation experiment in different conditions, and in particular with heavier ions. It is worth bearing in mind that negative results in this technique validate the theory for which the suppression of the hysteresis is better obtained using massive ions.

The future of the comprehension of the process leading to modifications in giant magnetocaloric properties will consist in a deep analysis of the defects associated with the phase transition. In the thesis we mention the theory according to which defects acts as nucleations sites which facilitate, avoiding metastable state, the transition from a phase to the other. Even if this interpretation is sustained by studies of local magnetic properties that show, for example in MnAs the persistence of non-magnetic phase even at low temperature, the complete understanding of the process inducing the modification is still not completely clear. The analysis of the defects will have to consider both a theoretical investigation of the process and practical measurements of the structural modifications induced. A possible defects characterization technique that can be adopted is the Raman spectroscopy while a method the study of structural changes in the material lattice can be achieved through X-ray diffraction. In first place, a more precise method for numerical simulation of the ion-matter interaction will be required. A good model to simulate the ion matter interaction will have to consider nuclear and electronic stopping power, the possibility of reparation of point-like defects and the possibility of defects diffusion through thermal agitation.

The research activity on the control of giant magnetocaloric material phase transition should be encouraged by the possibility of exploiting the entropy change in real magnetic refrigeration prototype but also in many energetic applications, for example, one purpose could be the exploitation of the direct conversion of heat into electricity (alternative to

the Seebeck effect). About this last point, from my personal point, as continuity of the research activity of study the magnetocaloric material I will join a Ph. D. project for the demonstration of thermo-magnetic power generation using giant-magnetocaloric material in Grenoble at Nèel Institute.

Acronym

Acronyms

ECRIS Electron Cyclotron Resonance ion source

ERDA Elastic Recoil Analysis Detection

MBE Molecular Beam Epitaxy

MCE Magnetic Caloric Effect

MCM Magnetic Caloric Material

MnAs Manganese Arsenide

MnFeSiP Manganese Iron Silicon Phosphorus (powder compound)

NRA Nuclear Reaction Analysis

NRP Nuclear Resonance Profiling

RBS Rutherford Backscattering Spectometetry

SAFIR Système d'Analyse par Faisceaux d'Ions Rapides

SPM Scanning Probe Microscope

SIMPA French acronym for Highly Charged Ion Source of Paris

SQUID Superconducting Quantum Interface Device

SRIM the Stopping and Range of Ion in Matter

STM Scanning Tunneling Microscope

VSM Vibrating Sample Magnetometer

Bibliography

[1] Sophie Cervera. «Manipulation des propriétés magnétiques de matériaux à effet mag-
     nétocalorique géant par impact d'ions lurds». Thèse de doctorat. Université Pierre et
     Marie Curie, 2017. URL: https://hal-mines-albi.archives-ouvertes.fr/INSP/
     tel-01706419v1.

[2] P. Weiss and A. Piccard. «Le phénomène magnétocalorique». In: *J. Phys. Theor.
     Appl.* 7 (1917), pp. 103–109.

[3] P. Debye. «Einige Bemerkungen zur Magnetisierung bei tiefer Temperatur». In: *An-
     nalen der Physik* 386 (1926), pp. 1154–1160.

[4] Giauque WF. «A thermodynamic treatment of certain magnetic effects. A proposed
     method of producing temperatures considerably below 1° absolute». In: *J. Am. Chem.
     Soc* 49 (1927), pp. 1864–1870.

[5] Giauque WF and MacDougall DP. «Attainment of temperatures below 1 K absolute
     by demagnetization of $Gd_2(SO_4)_3\ldots 8H_2O$». In: *Physical Review Letters* 43 (1933),
     p. 768.

[6] G. V. Brown. «Magnetic heat pumping near room temperature». In: *Journal of Ap-
     plied Physics* 47 (1976), pp. 3673–3680.

[7] W. A. Steyert. «Stirling-cycle rotating magnetic refrigerators and heat engines for use
     near room temperature». In: *Journal of Applied Physics* 49 (1978), pp. 1216–1226.

[8] V. K. Pecharsky and Jr. K. A. Gschneidner. «Giant Magnetocaloric Effect in $Gd_5(Si_2Ge_2)$».
     In: *Physical Review Letters* 386 (1997), pp. 4494–7.

[9] B. F. Yu et al. «Review on research of room temperature magnetic refrigeration».
     In: *International Journal of Refrigeration* 26 (2003), pp. 622–636.

[10] V. K. Pecharsky and K. A. Gschneidner. «Some common misconceptions concerning
     magnetic refrigerant materials». In: *Journal of Applied Physics* 90 (2001), pp. 4614–
     22.

[11] BK Ponomarev. «Apparatus for measuring the magnetocaloric effect in metal spec-
     imens in pulsed fields up to 8 T». In: *Instruments and experimental techniques of
     applied physics* 26 (1983), pp. 659–662.

[12] Kato et al. «Instrumentation for highly sensitive measurement of magnetocaloric
     effect: application to high Tc superconductors». In: *Cryogenics* 31 (1991), pp. 424–
     430.

[13] W Otowski et al. «New acoustic detection technique for a magnetocaloric effect». In: *Thermochimica acta* 218 (1993), pp. 123–133.

[14] BR Gopal et al. «Noncontact thermoacoustic method to measure the magnetocaloric effectt». In: *Review of scientific instruments* 66 (1995), pp. 232–238.

[15] J. RomeroGòmez et al. «Magnetocaloric effect: A review of the thermodynamic cycles in magnetic refrigeration». In: *Renewable and Sustainable Energy Reviews* 17 (2013), pp. 74–82.

[16] Tishin A. and Spichkin Y. *The Magnetocaloric Effect and its Applications. Series: Condensed Matter Physics.* 2003.

[17] John Y Fu. «On the Landau theory of phase transitions: a hierarchical dynamic model». In: *Journal of Physics: Condensed Matter* 25 (2013), p. 075903.

[18] Andreas Jeindl et al. *Advanced Solid State Physics.* TU Graz, 2009. Chap. 12: Landau Theory of Phase Transitions, pp. 151–155.

[19] Oliver Gutfleisch et al. «Mastering hysteresis in magnetocaloric materials». In: *Phil. Trans. R. Soc. A* 374 (2016), p. 20150308.

[20] Henrique Neves Bez et al. «Magnetocaloric materials and first order phase transitions». In: (2016).

[21] N. A. de Oliveira and P. J. von Ranke. «Theoretical aspects of the magnetocaloric effect». In: *Physics Reports* 489 (2010), pp. 89–159.

[22] KA Gschneidner Jr and VK Pecharsky. «Thirty years of near room temperature magnetic cooling: Where we are today and future prospects». In: *International journal of refrigeration* 31 (2008), pp. 945–961.

[23] Maximilian Fries et al. «Microstructural and magnetic properties of Mn-Fe-P-Si (Fe2 P-type) magnetocaloric compounds». In: *Acta Materialia* 132 (2017), pp. 222–229.

[24] Leticia Tocado, Elìas Palacios, and Ramòn Burriel. «Entropy determinations and magnetocaloric parameters in systems with first-order transitions: Study of MnAs ». In: *Journal of Applied Physics* 105 (2008), p. 093918.

[25] A Diestel et al. «Field-temperature phase diagrams of freestanding and substrate-constrained epitaxial Ni-Mn-Ga-Co films for magnetocaloric applications ». In: *Journal of Applied Physics* 118 (2015), p. 023908.

[26] Patrick J Shamberger and FS Ohuchi. «Hysteresis of the martensitic phase transition in magnetocaloric-effect Ni-Mn-Sn alloys». In: *Physical Review B* 79 (2009), p. 144407.

[27] Hironobu Fujii et al. «Magnetic properties of Fe2P single crystal ». In: *Journal of the Physical Society of Japan* 43 (1977), pp. 41–46.

[28] C Zimm et al. «Description and performance of a near-room temperature magnetic refrigerator». In: *Advances in cryogenic engineering.* Springer, 1998, pp. 1759–1766.

[29] V. K. Pecharsky et al. «Thermodynamics of the magnetocaloric effect». In: *Physical Review B* 64 (2001), p. 144406.

[30] JA Barclay and WA Steyert. «Active magnetic regenerator US Patent 4332135». In: (1982).

[31] Anders Smith et al. «Materials challenges for high performance magnetocaloric refrigeration devices». In: *Advanced Energy Materials* 2 (2012), pp. 1288–1318.

[32] Vitalij K Pecharsky and Karl A Gschneidner Jr. «Magnetocaloric materials». In: *Annual Review of Materials Science* 30 (2000), pp. 387–429.

[33] V Franco et al. «The magnetocaloric effect and magnetic refrigeration near room temperature: materials and models». In: *Annual Review of Materials Research* 42 (2012).

[34] Sindhunil Barman Roy. «First order magneto-structural phase transition and associated multi-functional properties in magnetic solids». In: *Journal of Physics: Condensed Matter* 25 (2013), p. 183201.

[35] TD Brown, I Karaman, and PJ Shamberger. «Impact of cycle-hysteresis interactions on the performance of giant magnetocaloric effect refrigerants». In: *Materials Research Express* 3 (2016), p. 074001.

[36] Vittorio Basso et al. «Theoretical approach to the magnetocaloric effect with hysteresis». In: *Annual Review of Materials Research* 290 (2005), pp. 654–657.

[37] Virgil Provenzano, Alexander J Shapiro, and Robert D Shull. «Reduction of hysteresis losses in the magnetic refrigerant Gd 5 Ge 2 Si 2 by the addition of iron». In: *Nature* 429 (2004), pp. 853–528.

[38] Ariana De Campos et al. «Ambient pressure colossal magnetocaloric effect tuned by composition in Mn 1- x Fe x As». In: *Nature Materials* 5 (2006), pp. 802–804.

[39] Jian Liu et al. «Giant magnetocaloric effect driven by structural transitions». In: *Nature materials* 11 (2012), pp. 620–626.

[40] Martino Trassinelli et al. «Magnetic properties of MnAs thin films irradiated with highly charged ions». In: *Nuclear instruments and methods in physic research* 317 (2013), pp. 154–158.

[41] Martino Trassinelli et al. «Suppression of the thermal hysteresis in magnetocaloric MnAs thin film by highly charged ion bombardment». In: *Applied Physics Letters* 104 (2014), p. 081906.

[42] S Cervera et al. «Hints on the origin of the thermal hysteresis suppression in giant magnetocaloric thin films irradiatied with highly charged ions». In: *Journal of Physics: Conference Series* 635 (2015), p. 012028.

[43] Martino Trassinelli et al. «Low energy Ne ion beam induced-modifications of magnetic properties in MnAs thin films». In: *Journal of Physics: Condensed Matter* 29 (2016), p. 055001.

[44] J-Y Duquesne et al. «Ultrasonic triggering of giant magnetocaloric effect in MnAs thin films». In: *Physical Review B* 86 (2012), p. 035207.

[45] Friedrich Aumayr and HP Winter. «Inelastic interactions of slow ions and atoms with surfaces». In: *Nuclear Instruments and Methods in Physics Research Section B: Beam Interactions with Materials and Atoms* 233 (2005), pp. 111–124.

[46] M. Nastasi, J. Mayer, and J.K. Hirvonen. *Ion-Solid Interactions: Fundamentals and Applications.* Cambridge Solid State Science Series. Cambridge University Press, 1996.

[47] Hannspeter Winter and Friedrich Aumayr. «Interaction of Slow HCI with Solid Surfaces: What Do We Know, What Should We Know?» In: *Physica Scripta* T92 (2001), pp. 15–21.

[48] IP Jain and Garima Agarwal. «Ion beam induced surface and interface engineering». In: *Surface Science Reports* 66 (2011), pp. 77–172.

[49] Peter Sigmund. «Elements of sputtering theory». In: *Nanofabrication by Ion-Beam Sputtering: Fundamentals and Applications* (2012), pp. 1–40.

[50] M. W. Thompson. «Defects and Radiation Damage in Metals». In: *Journal of Magnetism and Magnetic Materials* (1974).

[51] *Point Defect – Imperfections in Solids – Materials Science*. URL: http://www.minaprem.com/materials-science/defects/point-defect-imperfections-in-solids-materials-science/.

[52] Kai Nordlund et al. «Coherent displacement of atoms during ion irradiation». In: *Nature* (1999), pp. 49–51.

[53] C Chappert et al. «Planar patterned magnetic media obtained by ion irradiation». In: *Science* 280 (1998), pp. 1919–1922.

[54] D Ozkaya L et al. «Effect of Ga implantation on the magnetic properties of permalloy thin films». In: *Journal of applied physics* 91 (2002), pp. 9937–9942.

[55] D Weller et al. «Ion induced magnetization reorientation in Co/Pt multilayers for patterned media». In: *Journal of Applied Physics* 87 (2000), pp. 5768–5770.

[56] Kun Zhang et al. «Ion-induced phase transition in thin Co films». In: *Journal of magnetism and magnetic materials* 272 (2004), pp. 1162–1163.

[57] GA Müller et al. «Ion-beam induced changes in magnetic and microstructural properties of thin iron films». In: *The European Physical Journal B-Condensed Matter and Complex Systems* 48 (2005), pp. 449–462.

[58] J Fassbender et al. «Structural and magnetic modifications of Cr-implanted Permalloy». In: *Physical Review B* 73 (2006), p. 184410.

[59] D Oshima et al. «Control of Magnetic Properties of MnGa films by Kr+ Ion Irradiation for Application to Bit Patterned Media». In: *IEEE Transactions on Magnetics* 49 (2013), pp. 3608–3611.

[60] James F. Ziegler, Jochen P. Biersack, and Matthias D. Ziegler. *SRIM - The Stopping and Range of Ions in Matter*. 2008. Chap. 8.

[61] Roger E Stoller et al. «On the use of SRIM for computing radiation damage exposure». In: *Nuclear Instruments and Methods in Physics Research B* 310 (2013), pp. 75–80.

[62] GH Kinchin and RS Pease. «The displacement of atoms in solids by radiation». In: *Reports on progress in physics* 18 (1955), pp. 21–25.

[63] Laboratory of Nuclear Analytical Methods. *Van de Graaff electrostatic accelerator*. URL: http://neutron.ujf.cas.cz/vdg/graaff-principle.html.

[64] I. Vickridge E. Briand. *Rapid Ion Beam Analysis System (SAFIR)*. URL: http://www.insp.jussieu.fr/-Systeme-d-Analyse-par-Faisceaux-d,424-.html.

[65]   INSP:Institute of NanoSciences of Paris (Asur Team). *SIMPA source: technical presentation*. URL: http://www.insp.jussieu.fr/La-source-SIMPA-presentation.html.

[66]   Alexander Gumberidze et al. «Electronic temperatures, densities, and plasma x-ray emission of a 14.5 GHz electron-cyclotron resonance ion source». In: *Review of Scientific Instruments* 81 (2010), p. 033303.

[67]   Simon Foner. «Versatile and sensitive vibrating-sample magnetometer». In: *Review of Scientific Instruments* 30 (1959), pp. 548–557.

[68]   Simon Foner. «Review of magnetometry». In: *IEEE transitions on magnetics* 6 (1981), pp. 3358–3363.

[69]   *Chimie moléculaire de Paris Centre: Plateforme Mesures Physiques à Basses Températures*. URL: http://www.fr2769.upmc.fr/fr/plateformes_techniques/magnetisme.html.

[70]   Mohsin Rafique. «Study of the Magnetoelectric Properties of Multiferroic Thin Films and Composites for Device Applications». PhD thesis. COMSATS Institute of Information Technology, Islamabad-Pakistan, 2014. URL: https://www.researchgate.net/publication/322976482_Study_of_the_Magnetoelectric_Properties_of_Multiferroic_Thin_Films_and_Composites_for_Device_Applications.

[71]   RL Fagaly. «Superconducting quantum interference device instruments and applications». In: *Review of scientific instruments* 77 (2006), p. 101101.

[72]   Samuel Maguire-Boyle and Andrew R. Barron. «Practical Guide to Using a Superconducting Quantum Interference Device». In: (2009). URL: https://archive.cnx.org/contents/0eb9a88c-a813-41d9-befd-667beea5e6ff@2/practical-guide-to-using-a-superconducting-quantum-interference-device.

[73]   BTM Willis and HP Rooksby. «Magnetic Transitions and Structural Changes in Hexagonal Manganese Compounds». In: *Proceedings of the Physical Society. Section B* 67 (1954), p. 290.

[74]   L Däweritz. «Interplay of stress and magnetic properties in epitaxial MnAs films». In: *Reports on Progress in Physics* 69 (2006), p. 2581.

[75]   L. Pytlik and A. Zieba. «Magnetic phase diagram of MnAs». In: *Journal of Magnetism and Magnetic Materials* 51 (1985), pp. 199–202.

[76]   H. Wada and Y. Tanabe. «Giant magnetocaloric effect of $MnA_s1 - xSb_x$». In: *Applied Physics Letters* 20 (2001), pp. 3302–3304.

[77]   R Breitwieser et al. «Phase transition and surface morphology of MnAs/GaAs(001) studied with in situ variable-temperature scanning tunneling microscopy». In: *Phys. Rev. B* 80 (2009), p. 045403.

[78]   M Kästner et al. «Atomic scale morphology of self-organized periodic elastic domains in epitaxial ferromagnetic MnAs films». In: *Journal of Applied Physics* 92 (2002), pp. 5711–5713.

[79]   Lauri Panitzsch, Michael Stalder, and Robert F Wimmer-Schweingruber. «Direct high-resolution ion beam-profile imaging using a position-sensitive Faraday cup array». In: *Rev. Sci. Instum.* 808 (2009), p. 113302.

[80] WM Kaminsky et al. «Patterning ferromagnetism in Ni80Fe20 films via Ga+ ion irradiation». In: *Applied Physics Letters* 78 (2001), pp. 1589–1591.

[81] Kun Zhang et al. «Xenon-ion–induced phase transition in thin Co films». In: *EPL (Europhysics Letters)* 64 (2003), p. 668.

[82] DH Mosca, F Vidal, and Victor H Etgens. «Strain Engineering of the Magnetocaloric Effect in MnAs Epilayerss». In: *Phys. Rev. Lett* 101 (2008), p. 125503.

[83] S Cervera et al. «Modulating the phase transition temperature of giant magnetocaloric thin films by ion irradiation». In: *Physical Review Materials* 1 (2017), p. 065402.

[84] DT Cam Thanh et al. «Structure, magnetism, and magnetocaloric properties of Mn Fe P 1- x Si x compounds». In: *Journal of Applied Physics* 103 (2008), 07B318.

[85] A Bartok et al. «Study of the first paramagnetic to ferromagnetic transition in as prepared samples of Mn–Fe–P–Si magnetocaloric compounds prepared by different synthesis routes». In: *Journal of Magnetism and Magnetic Materials* 400 (2016), pp. 333–338.

[86] Nguyen H Dung et al. «From first-order magneto-elastic to magneto-structural transition in (Mn, Fe) 1.95 P0. 50Si0. 50 compounds». In: *Applied Physics Letters* 99 (2011), p. 092511.

[87] Alexandre Pasko et al. «X-ray diffraction analysis of the magnetoelastic phase transition in the Mn-Fe-P-Si magnetocaloric alloy». In: *AIP ADVANCES* 6 (2016), p. 056204.

[88] SR Shinde et al. «Influence of 85 MeV oxygen ion irradiation on magnetization behavior of micron-sized and nano-sized powders of strontium ferrite (SrFe12O19)». In: *Journal of Magnetism and Magnetic Materials* 186 (1998), pp. 342–348.

[89] L Zhang et al. «Neutron diffraction study of history dependence in MnFeP0. 6Si0. 4». In: *Journal of magnetism and magnetic materials* 290 (2005), pp. 679–681.